R-457
CU-253
NEVIS-147

Nevis Laboratories
Columbia University
Physics Department
Irvington-on- Hudson
New York

Positron Spectrum from Muon Decay

JOHN PEOPLES

Submitted in partial fulfillment of
the requirements for the degree
of Doctor of Philosophy in the Faculty
of Pure Science, Columbia University

May 1966

Office of Naval Research
Contract Nonr-266(72)

Positron Spectrum from Muon Decay †

JOHN PEOPLES *

Columbia University, New York, New York

† Research supported in part by the Office of Naval Research Nonr-266(72).

* Submitted in partial fulfillment of the requirements for the degree of Doctor of Philosophy in the Faculty of Pure Science, Columbia University.

John Tyndall Fellow: 1962-1964

George B. Peagram Honorary Fellow: 1964-1965.

ABSTRACT

The positron spectrum from the decay of positive muons was studied using a sonic spark chamber spectrometer. An analysis of 1.1 million events gave a value for the Michel parameter of 0.750 ± 0.003. This number includes internal radiative corrections and is to be compared directly with the 0.750 predicted by the V-A theory. An upper limit on the mass of the muon neutrino was set at 1.5 MeV.

TABLE OF CONTENTS

I. WEAK INTERACTIONS AND MUON DECAY

The decay of the muon is unique among the weak interaction processes that can be studied experimentally at the present time. The uniqueness stems from the fact that the decay is very nearly a bare weak interaction. The decays of other particles such as baryons or mesons are modified by the strong interactions of these particles. It is not possible to separate the weak interactions from the strong interactions because a quantitative theory of strong interactions does not exist. The comparison of the decay of the muon and the decay of a free neutron illustrates the theoretical difficulty of including strong interactions in any description of weak interactions. When a muon decays the strongest interaction between the initial state muon and the final state electron is through the emission and absorption of virtual photons. While this process, internal radiative corrections, modifies the decay by a few percent, the effect can be calculated by perturbation theory.[1] To order α the changes in decay amplitude are included in the following Feynman diagrams

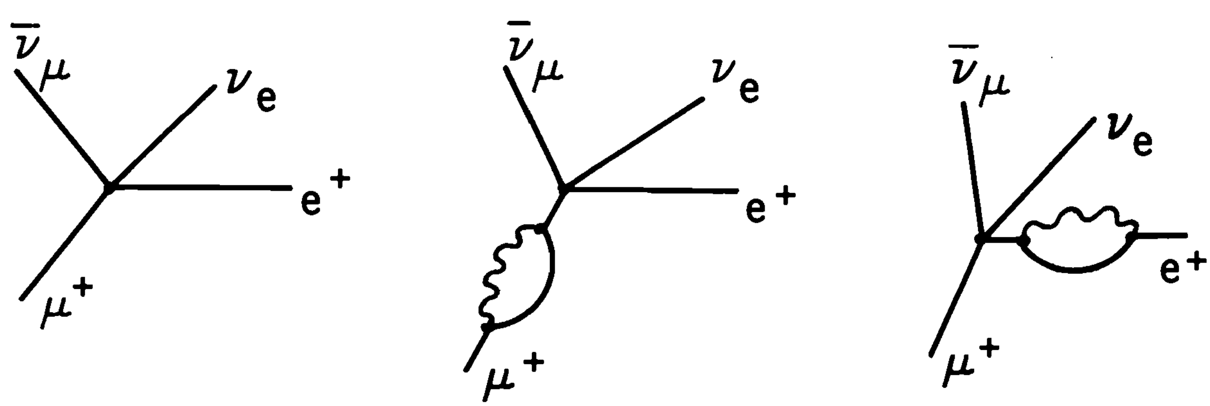

These graphs which are added coherently with the unmodified graph change the decay amplitude by an amount which is of the order $e^2 = 1/137$. [2] When higher ordered contributions are considered, their contributions are still smaller by an additional factor of e^2. The neutron will interact with the final state proton by emitting and absorbing virtual pions. Since the coupling constant of pions to nucleons $G^2/4\pi$ is 15, the corrections are at least as large as the unmodified term and hence perturbation theory is not applicable. Recently, calculations using dispersion relations have been made of the ratio of the axial vector coupling constant to the vector coupling constant which agree reasonably with experiment. Nevertheless, these calculations require the knowledge of cross section off the mass shell and therefore cannot be calculated exactly.[3]

The foregoing comparison proceeds from the assumption that muon decay and neutron decay are manifestations of the same interaction. The fact that the strength of the interaction responsible for muon decay is about the same strength as the interaction for β decay, led to this assumption. This notion was expanded to include the decay of the pi meson, strange particle decays, and mu capture.[4] In this form of the theory, known as the Universal Fermi Interaction, all weak processes were believed to be due to an interaction of two vector currents which were constructed from the interacting particles. The hamiltonian is

$$\mathcal{H} = \sqrt{8}\ G\ j_\alpha j^{\alpha\dagger} \tag{1}$$

j_α is a vector current formed out of the particles which participate in all possible weak interactions. j_α can be decomposed into two parts a lepton part ℓ_α which is written explicitly as

$$\ell_\alpha = \tilde{\mu}\gamma_\alpha \frac{(1+i\gamma_5)}{2} \nu_\mu + \tilde{e}\gamma_\alpha \frac{(1+i\gamma_5)}{2} \nu_e + \text{H.C.} \tag{2}$$

The second part h_α includes contributions which induce $\Delta S = 0$ and $\Delta S = 1$ transitions. The earliest form of universality which included strange particle decays, due to Feynman and Gell-Mann, treated the $\Delta S = 0$ and $\Delta S = 1$ terms on the same footing.[4] For example, the part of h_α due to the proton, neutron and Λ would be

$$h_\alpha = \tilde{n}\gamma_\alpha \frac{(1+i\gamma_5)}{2} p + \tilde{\Lambda}\gamma_\alpha \frac{(1+i\gamma_5)}{2} p + \text{H.C.} \tag{3}$$

With the exception of the predictions made by the $\Delta S = 1$ part of the h_α current, the universal of fermi interaction is in excellent agreement with the experimental results. The leptonic decay rates of the hyperons are a factor of ten slower than rates predicted using a current such as Eq. (3) for the baryons. After the usefulness of SU_3 in predicting relations between strong interaction processes became evident, Cabibbo proposed a weaker form of universality that was able to remove the one qualitative disagreement between theory and experiment.[5] The weaker form of universality modifies the hadronic current to the form

$$h_\alpha = \cos\theta\ h_\alpha^{o} + \sin\theta\ h_\alpha^{'} \tag{4}$$

h_α^o would induce $\Delta S = 0$ transitions, and h_α' would induce $\Delta S = 1$ transitions. The angle θ can be determined from the comparison of the rates of K_{e3} to π_{e3}. The modified Universal Fermi Theory, which will be called UFI hereafter, is in both qualitative and quantitative agreement with the experiments done to date. Because the angle θ has not been well determined by experiment, the validity of the $\Delta S = 1$ part is not established as well as the $\Delta S = 0$ part. An important puzzle remaining in the $\Delta S = 0$ part is the fact that G as determined from β-decay and μ-decay is not the same. The value of $\cos\theta$ needed to explain this discrepancy is just within the experimental limits on $\cos\theta$.

The contribution made by muon decay experiments to the development of this theory has been small. This stems from the fact that the totality of muon decay experiments which can be done cannot provide all of the details necessary to demonstrate that mu decay is in fact a weak interaction. One would have to do experiments with the neutrinos from muon decay to establish this.

Even if all experiments which could be done with the neutrinos from muon decay were done, the order of the lepton fields in the muon decay hamiltonian could not be fixed by muon decay experiments alone. As long as muon decay is regarded as an example of a weak interaction and not an isolated phenomenon, the ambiguity disappears since the composition of the lepton currents is established from the weak decays of mesons and baryons. The point is made at this time because historically muon decay has not been treated with the ordering of the lepton currents observed in the weak decay of mesons and baryons. When cast in this older form, conclusions about whether the weak interaction are $V + \epsilon A$ or V-A becomes meaningless since the V and A are not the V and A of the UFI theory, but are actually linear combinations of the coupling constants. This point will be treated at length in Sec. VIII when the results of this experiment are interpreted.

If muon decay is treated in very general form, excluding only derivative couplings, there are twenty real numbers which characterize the decay. If experiments with the neutrinos that accompany muon decay are excluded, only five relations between the twenty coupling constants can be determined from experiment. The UFI theory makes very definite predictions about these five experimental quantities and, as will be shown, these predictions are in agreement with experiment. To arrive at these predictions it is worthwhile to start from a more general interaction for muon decay.

The lifetime, the momentum spectrum of the decay electron, and the decay electron polarization are the measurable properties of the muon which depend in a fundamental way on the weak interactions. These properties can be calculated accurately from a simple theory in which the four leptons interact at one point. If derivative couplings are excluded, the most general local four-fermi interaction is described by the interaction hamiltonian of Eq. (5):

$$H_I(\chi) = \sqrt{2} \sum_i G_i \tilde{\nu}_e O_i^e e(x)\ \tilde{\mu}(x) O_i^{\mu}\ \nu_{\mu}(x) + \text{H.C.} \tag{5}$$

where

O_i^{ℓ} are formed from the γ matrices as follows:

$$O_1^{e,\mu} = a_1^{e,\mu}\ I + ib_1^{e,\mu}\ \gamma_5 \tag{6}$$

$$O_2^{e,\mu} = a_2^{e,\mu}\ \gamma_\alpha + ib_2^{e,\mu}\ \gamma_5\gamma_\alpha \tag{7}$$

$$O_3^{e,\mu} = a_3^{e,\mu}\ \sigma_{\alpha\beta} + ib_3^{e,\mu}\ \gamma_5\sigma_{\alpha\beta} \tag{8}$$

The modulus of the vectors (a,b) is 1. There are ten independent coupling constants. The hamiltonian is not necessarily invariant under C, P, or T, but it is CPT invariant as a consequence of its invariance under all proper lorentz transformations. The electron momentum spectrum computed from this hamiltonian can be characterized by a third-order polynomial, the coefficients of which are functions of the ten coupling constants.[6,7] The result is

$$\frac{dN}{dX} = \frac{d\Omega}{4\pi} \frac{A}{\left(1+\frac{4m_e}{m_\mu}\eta\right)} x^2 \left[3(1-x)+2\rho\left(\frac{4}{3}x-1\right)+6\eta\frac{m_e}{m_\mu}\left(\frac{1-x}{x}\right) - p\xi\cos\theta\left(1-x+2\delta\left(\frac{4}{3}x-1\right)\right)\right] \tag{9}$$

where

x = ratio of electron momentum to its maximum momentum

p = polarization of the decay muon

θ = the angle between μ-spin and the decay electron momentum vector

ρ, ξ, η, δ are dimensionless constants which are functions of the coupling constants.

After non-conservation of parity in β-decay[8] and in μ-decay[9] were discovered, it was shown that a neutrino which had only one state of helicity could explain both experiments.[10] This choice simplifies the weak interaction and there can be only two independent coupling constants: a vector and a scalar coupling. The values of ρ, ξ, δ, and η are in this case:

$$\rho = 3/4 \qquad \xi = \frac{|G_S|^2 - 4|G_V|^2}{|G_S|^2 + 4|G_V|^2} \qquad \delta = 3/4 \qquad \eta = \frac{2G_S G_V}{G_V^2 + (\frac{G_S}{4})^2}$$

The Universal Fermi Interaction of Feynman and Gell-Mann simplifies the interaction still further.[4] This theory, discussed earlier, has only one bare coupling constant G. Since $G = G_V = G_A$ and $G_S = 0$, the theory predicts the following results:

$$\rho = 3/4 \qquad \xi = -1 \qquad \delta = 3/4 \qquad \eta = 0 \; .$$

The theory makes predictions about the decays of other particles. For example, the branching ratio of the π_{e2} decay to $\pi_{\mu 2}$ decay is extremely sensitive to the presence of a scalar or pseudo-scalar coupling in the lepton currents. The agreement between the experimentally measured branching ratio and the value predicted by UFI is excellent.[11] If this experiment is interpreted as setting a lower limit on G_S, then $G_S < 10^{-3}\, G_V$. Other experimental tests of the theory are both numerous and successful. In particular, the best experimental values for ξ and δ are:[12,13]

$$|\xi| \geq 0.975 \pm 0.054 \quad \text{(Ref. 12)}$$

$$\delta = 0.78 \pm 0.05 \quad \text{(Ref. 13)} \; .$$

ξ and δ can only be measured from polarized muon decays. The sign of ξ is known to be negative from a separate experiment.[14]

η has not been measured reliably because the spectrum is sensitive to η primarily for momenta less than 5 MeV. It is in this momentum region that the experiment reported here and all past experiments have provided little or no information. ρ has been measured many times in the past and a description of the history of this measurement is given in Sec. II. The best bubble chamber measurements of ρ agree with the UFI theory to within the experimental error.

These measurements for ρ, ξ, and δ do not ambiguously establish the correct form of the hamiltonian, but they do provide a test of UFI. If UFI is to be checked as a hypothesis, then a large number of other experiments put restrictions on the form of the hamiltonian, for example, the previously cited π_{e2} decay rate. If other experiments have provided more sensitive and hence more crucial tests of the nature of the lepton currents in UFI, it is reasonable to ask; "What does an accurate measurement of the electron spectrum of unpolarized muons establish?" Considering that the radiative corrections are the least tested features of the weak decays, a careful measurement of the decay of a muon tests the validity of these corrections. These corrections, which amount to a few percent over most of the spectrum, were well within the range of sensitivity of the experiment described in the remainder of the report. By restricting the interaction, specific statements can be made about non-locality and lepton conservation. A discussion of these statements is made in Sec. VIII.

II. HISTORY OF THE MEASUREMENT OF THE MICHEL PARAMETER

The first experimental studies of the decay of the muon were directed at identifying the decay products. By measuring the brehmsstrahlung yield of the charged decay product in lead, it was established by Pontecorvo and Sard that this particle was an electron.[15] The neutral decay products were shown not to be photons.[16] These experiments did not establish anything further about the neutral particles. The general features of the electron spectrum provided some of the remaining pieces of information. These features are as follows: there is a continuous spectrum of momenta and as a consequence a two-body decay is not possible. The average momenta is $\frac{1}{3} m_{\mu}c$, which suggests a three-body decay. The maximum momenta observed is $\frac{1}{2} m_{\mu}c$, and hence the mass of the neutral particles is zero within experimental limits. No experiments which give observable results have been performed using the neutral particles from muon decay. As a result the neutrals are taken to be the muon neutrino and the electron neutrino only by inference. If these neutrals are different particles, their interaction strength is not vastly different from that of the aforementioned neutrinos. This statement follows from the cross section measurements made for high energy neutrinos on nucleons. These results are based on the assumption that only neutrinos from π and K decay interact in the detector. Neutrinos from muon decay are down a factor of 1000 in intensity. Since the cross sections are known to about 30% and since they agree with the preceding assumption, the interaction of the neutrals from muon decay with nucleons is no more than 30 G_V.[17] Another piece of indirect evidence stems from the fact that parity is violated in all interactions in which neutrinos are emitted, and parity is violated in mu-decay. Finally, the two neutrals are not the same particle since this would permit the muon to decay into an electron and a gamma ray.

An experiment by Steinberger[18] which used geiger counters and an experiment of Anderson, Leighton and Seriff,[19] which used a cloud chamber, were the first to show conclusively that muon decay was not a two-body process. Both experiments were done with muons from cosmic rays and are prototypes of the two kinds of experiments that have been done since. Muon decay events were identified in the counter experiment by using a delayed coincidence which would be sensitive to events with the lifetime of the muon. The energy was measured by the range in polyethylene. Later counter experiments have measured the momentum by the curvature in a magnetic field, while identifying a decaying muon by its lifetime. The cloud chamber experiment made identification by the topology of the track and measured momentum by curvature in a magnetic field.

After the meson-producing cyclotrons began to operate, large enough fluxes of muons became available to study the decay more accurately. Two types of apparatus were used: magnetic spectrometers with scintillation counters and diffusion cloud chambers. After the H_2 bubble chamber was developed, it was used in place of the cloud chamber. The results of all the experiments done at accelerators are presented in Table I.

TABLE I

Experimental Results of ρ Value Measurements
Done at Accelerators Before 1964 †

Experimenter	Year	Technique	Events	Value of ρ
Bramson et al [a]	1952	Photographic Emulsions	301	0.48 ± 0.13
Villain et al [b]	1954	Expansion Cloud Chamber	280	0.50 ± 0.13
Sargent et al [c]	1955	Diffusion Cloud Chamber	415	0.68 ± 0.11
Rosenson [d]	1956	Diffusion Cloud Chamber	1300	0.67 ± 0.05
Dudziak et al [e]	1959	Magnetic Spectrometer	——	0.741 ± 0.022
Plano [f]	1960	H_2 Bubble Chamber	9000	0.780 ± 0.025
Bloch et al [g]	1962	He Bubble Chamber	9000	0.751 ± 0.034
Barlow et al [h]	1964	Magnetic Spectrometer	——	0.661 ± 0.016

† For full details, see Ref. 20.

Table I illustrates that the measurement of ρ, which has been attempted frequently in the past, has shown a disturbingly large degree of inconsistency. However, with the exception of Ref. 20h, the results of the more recent experiments are in good agreement with one another and these experiments agree with $\rho = 3/4$. In order to make a comparison of the two types of techniques, it is reasonable to combine the results of Ref. 20f and 20g which were both made with bubble chambers. This combination assumes the validity of CPT, since Ref. 20f was a study of μ^+ decays and Ref. 20g was a study of μ^- decays. The combined result derived from Ref. 20f and 20g, $\rho = 0.768 \pm 0.021$, is not in agreement with Ref. 20h but is in agreement with Ref. 20e. Because the statistical errors of Ref. 20a through 20d are so much larger, their agreement or lack of agreement is not particularly significant, except to point out that in some of these experiments systematic errors were not correctly estimated. A careful critique of each experiment is not possible on the basis of the published papers. A reasonable conclusion to be drawn from this work is that the possibility for unevaluated systematic errors is much greater in the experiments which used the magnetic spectrometer than in the bubble chamber experiments. In Refs. 20e and 20h large systematic corrections of the order of 5% were made to account for the properties of the spectrometer. The bubble chamber as a tool for exploring the decays of particles is known to be free of serious systematic errors and has been used to do this for almost a decade.

The purpose of the review of past experiments was to decide what features of each technique were free of systematic errors and which features would lend themselves to a statistically more powerful experiment. If measurements are made over the whole spectrum in proportion to the rate at which the decay occurs, the uncertainty in ρ due to statistical fluctuations is $\sqrt{6/N}$. (N is the number of events.) The original goal of this experiment was to have an accuracy of 1×10^{-3} and hence

6×10^6 events would be needed. The magnitude of data that must be processed precluded the use of bubble chamber techniques without automatic scanning equipment. The magnetic spectrometer techniques do not have such a limitation, since data are acquired quickly and require very little processing. A set of guidelines to evaluate an experimental apparatus, which is designed to measure ρ to 0.001, are as follows:

1. The momentum measurement must be free of systematic errors to one part in 10^4 and the momentum resolution should be 1% or better.
2. The momentum acceptance of the magnet must be large enough so that either the experiment can be carried out at one magnetic field, or a statistically significant measurement of ρ can be made at each field.
3. The solid angle from which muon decay events are selected must be known to be momentum-independent.
4. The experiment must be capable of analyzing 6×10^6 events.

Items 2 and 3 are inherent to a bubble chamber experiment and are not present in a typical magnetic spectrometer experiment. By using a unique type of spark chamber, which did not rely on film for recording the data, it was possible to retain the features common to the bubble chamber experiment, improve the momentum resolution significantly over all past experiments and still process more than 6×10^6 events. The degree to which the experimental apparatus satisfied the guidelines outlined earlier is as follows:

1. The positron momentum was measured to 1/3% and was free of systematic errors to 4 parts in 10^4.
2. The momentum acceptance of the magnet, $\Delta P/\bar{P}$, was 40%. Statistically, significant measurements of ρ were possible at all fields.
3. The solid angle from which muon decay events were selected was 1/10 sr and was demonstrated to be momentum-independent.
4. In the final measurement of ρ, 15 x 10^6 events were analyzed of which 1.5 x 10^6 were used.

The experiment fell short of the $\Delta\rho$ = 0.001, although 0.0025 was achieved. In Sec. III a description is given of the apparatus that was used; in Sec. IV a detailed description of the spark chamber is given.

III. EXPERIMENTAL TECHNIQUES

A. General Description [21]

The experimental apparatus, shown in Fig. 1, was composed of four single-gap sonic spark chambers, a pion counter telescope (not shown in the figure) and a positron telescope. A positive pion beam from the Columbia Synchrocyclotron was incident along the direction of the magnetic field, which is perpendicular to the plane of Fig. 1. Approximately 1000 pions/sec were stopped in a 3 in. x 3 in. x 1/8 in. plastic scintillation counter.

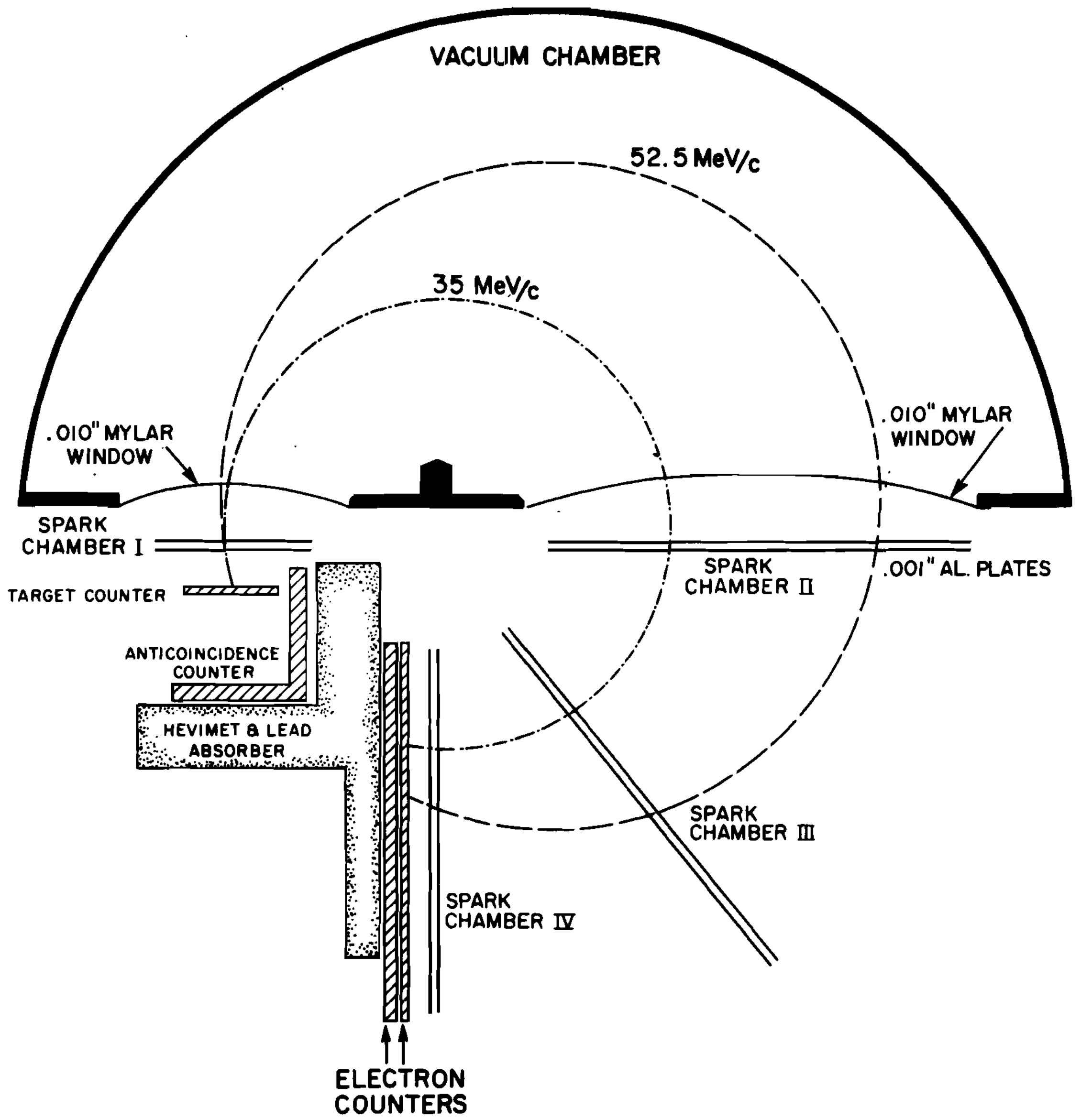

Fig. 1 Experimental Apparatus

The stopped pions decayed into muons in this target and 80% of these muons stopped in the target. These muons, which had no average polarization, subsequently decayed into positrons and about 3% of the positrons were detected by the electron counters. The orbits of the detected positrons were entirely within a uniform field to minimize vertical focusing. The positrons which were detected started in the target counter, traversed the vacuum tank and the four spark chambers, and after passing through the electron counters they were stopped in a hevimet and lead absorber.

The detection of a pion stopping in the target by the pion telescope generated a 2-μsec gate delayed by 0.5 μsec. A fast coincidence between the pulses from the target and the electron counters, which occurred during the gate, triggered the four spark chambers. A pulse in the anticoincidence counter, which occurred at the same time as the fast coincidence, vetoed the spark chamber trigger pulse. The pulse height from the target counter was measured to determine the ionization loss of the emerging positron.

The momentum and angle of emission of the positron were determined by fitting a helix to the position of the sparks in Chambers I, II and III. The position of the spark in Chamber IV and the coordinate of the spark in Chamber III which is parallel to the field were used to exclude particles that may have been scattered by surrounding materials. The major part of the trajectory, between Chambers I and II, is in vacuo. The 0.10-in. thick Mylar windows of the vacuum tanks and spark chamber I and II were near the 180-deg line of the spectrometer, where multiple scattering could cause relatively little uncertainty in the momentum measurement. The spark chambers were single-gap chambers which have 0.001-in. Aℓ foil electrodes. The spark positions were determined without photography by measuring the time between the spark trigger and the arrival of the soundwave associated with the spark at a microphone in the chamber. While two microphones are needed to locate a spark, each chamber contains four microphones and the extra microphones were used to detect the presence of more than one spark. For each event the transit time of soundwave to each microphone was measured and digitized. In addition, the pulse height was measured and digitized. The digitized information was transmitted to an IBM 1401 computer. The data were then written on magnetic tape by the 1401. The data could be accumulated at a maximum instantaneous rate of 40 events/sec; the limitation was due to the computations performed by the program stored in the 1401 after each event. In practice, data were accumulated at a slower rate, 15 events/sec, as a result of the pion beam intensity. The trajectory of each event was reconstructed from the data on magnetic tape using a 7094. The limited computational facilities of the on-line 1401 were used only for checks of the spark chamber and pulse-height analyzer operation.

The data were taken at eight different values of the magnet field in order to study the muon spectrum from 10 MeV to 53 MeV and to make several checks of the spectrometer. Figure 2 shows the momentum ranges for the three values of the field where most of the data were taken. The size of each momentum region is sufficiently large so that a separate determination of the Michel parameter could be made for each region. Moreover, because adjacent regions overlapped extensively with one another, a muon intensity monitor was not necessary.

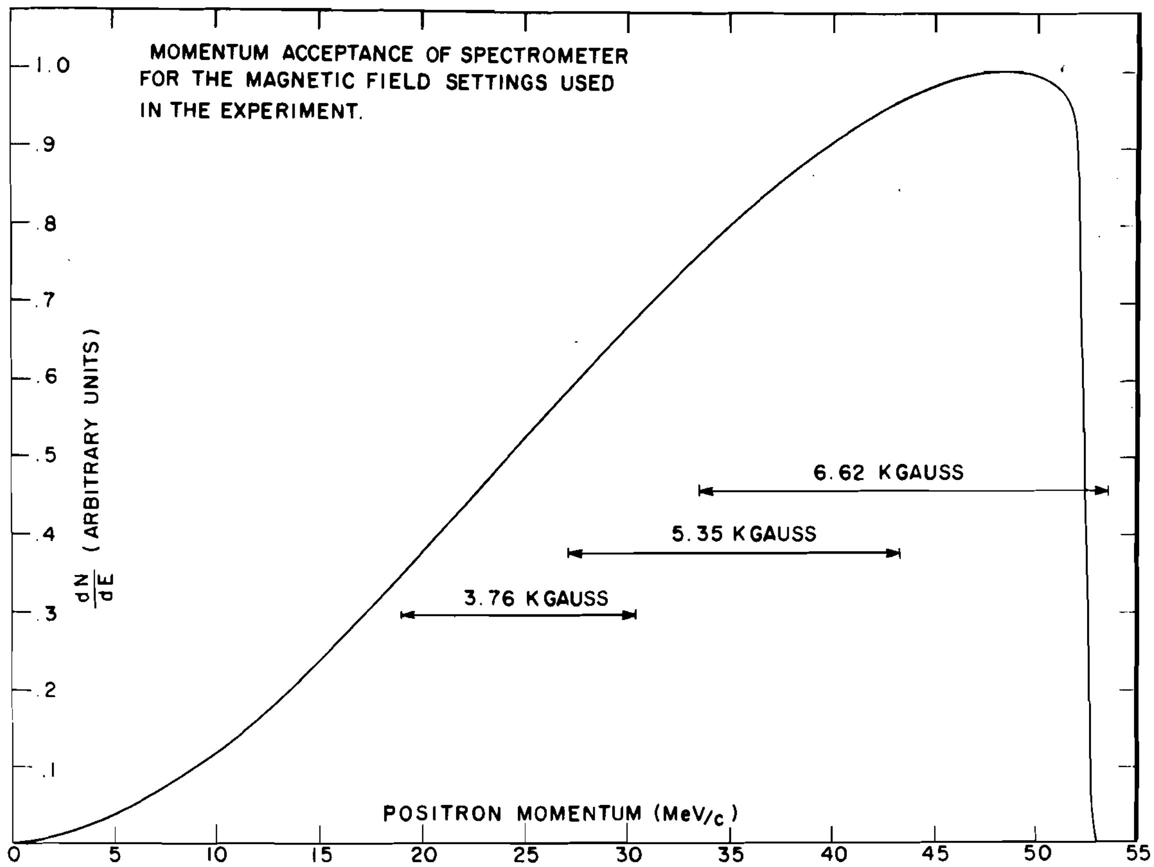

Fig. 2 Shape of the Momentum Spectrum for $\rho = 3/4$

The remainder of Sec. III describes in detail all of the experimental apparatus except the sonic spark chambers and the electronics associated with it. These are discussed in Sec. IV and the analysis of the data is discussed in Sec. VI.

B. Magnetic Field

The magnet used in the experiment was a 36-in. cloud chamber magnet. The magnet is made of a pair of coils which have an inside diameter of 36 in. and the coils are separated by 17 in. The magnet does not have pole tips and is open at both ends (see Fig. 3). At a distance of 38 cm from the axis the 6000 G field has decreased by 5% from the value at the center. Such a field shape was not adequate for the experiment and extra coils were added to improve it. The coils were designed by simulating the existing field on a computer and then adding the magnetic fields due to coils mounted coaxially with the cloud chamber coils. The assumption of superposition was reasonable since the iron structure supporting the cloud chamber coils provided very little return path for the flux from the auxiliary coils. The study showed that a field with a uniformity of 1 part in 1000 could be obtained in a cylindrical volume which had a 30-in. diameter and 12-in. height.

A pair of coils were added in the median plane. These coils had an inside diameter of 36 in. and each had 448 turns. A second pair of coils were placed coaxially with the magnet axis and 12 in. from the median plane of the magnet. The median plane is the plane parallel to the cloud chamber coils and passes midway between gaps between these coils. The second set of shim coils were 9 in. i.d. and each had 192 turns. The placement of the coils in the magnet is shown in Fig. 4.

The 36-in. shim coils build the field up at large radii in the median plane. The coils supply 10% of the field at the center of the magnet. The small coils compensate for the second order inhomogeneities introduced by the 36-in. shim coils. A comparison of the field shape before and after the coils is shown in Fig. 5. A field uniformity of 1 part in 1000 over the whole 30-in. by 12-in. cylinder was not obtained because of the difficulty in aligning the 36-in. shim coil, which weighed 2 tons, and the slight misalignment of the cloud chamber coils. These misalignments caused the deviations from axial symmetry.

The field shapes at various field strengths are shown in Figs. 6, 7, 8 and 9. These fields were uniform to 1 part in 1000 over most of the region needed by the spectrometer. The field deteriorated at the edges; nevertheless, the effect on each trajectory was small.

C. Spark Chamber Spectrometer

The spectrometer is made up of three elements: four single-gap sonic spark chambers, a vacuum tank, and a supporting frame. Each spark chamber is a machined brass frame on which are mounted two thin foil electrodes, 0.001-in. Aℓ, and four microphones (see Fig. 10). The spark chamber windows are 0.003-Mylar. The spark chambers are positioned on an Aℓ frame machined to tolerances of 0.001 in. The sides of the frame were held in position by stainless steel dowel pins rather than screws. The chambers were also held in position by dowel pins and shoulder screws. On the basis of machining tolerances the locations of the chambers were known relative to one another to 0.001 in. In addition to the chambers the frame contains a shelf which supports the lead and hevimet positron stopper.

Mounted on the spectrometer frame is a stainless steel vacuum tank. The windows of the vacuum tank are made of 0.010 in. Mylar. The spectrometer was placed in the magnet by sliding it on teflon bearings onto support rails mounted on the 36-in. shim coil. It was not bolted or pinned in place and hence was free to move if the magnet expanded or contracted. Whenever the magnet was turned on or off there were small motions of the coils. A photograph of the spectrometer is shown in Fig. 11. Chambers I, II and III were used to determine a helix from which the momentum and the angles of emission were calculated. The helix was projected into Chambers III and IV and the difference between the calculated and actual positions in these chambers is used to eliminate trajectories which have scattered in the spectrometer.

During the experiment the spark chambers were pulsed as often as 20 times/sec for periods as long as five days. The efficiency of the chambers was measured to be better than 98%. Most of these missing sparks were attributable to accidental triggers. Bench tests which were run on the chambers with a β source showed the efficiency to be greater than 99.5%. The high efficiency during the experiment was maintained by circulating the gas in the spark chambers, 90% Ne and 10% He, over a charcoal trap. The trap was kept at room temperature while data were taken.

D. Muon Decay Detection Electronics

A pion which stopped in the target was detected by the pion telescope which consisted of three counters, as follows:

The π counter, not shown in Fig. 1, the target counter T, and the anticounter A. The π counter was a 4 in. x 4 in. x 3/8 in. thick plastic scintillator viewed by a 6810-A phototube. The target counter was a 3 in. x 3 in. x 1/8 in. plastic scintillator viewed by a 6810-A. The anticoincidence counter A was composed of three pieces of plastic scintillator, two of which were 6 in. x 4 in. x 1/2 in. and the third was 4 in. x 4 in. x 3/8 in. The three pieces of scintillator were arranged to form three sides of a rectangular parallelepiped and were viewed with a single 6810-A. The 6-in. side of the parallelepiped was parallel to the direction of the beam.

The decay positron was detected by the positron telescope which was composed of the T counter, A counter, and the electron counters. The first electron counter to be traversed by the positron, E1, was a 13-in. x 12-in. x 1/4-in. plastic scintillator. The second counter, E2, was a 13-in. x 12-in. x 3/8 in. plastic scintillator. Each counter is viewed with its own 6810-A.

The phototubes were shielded from the large magnetic field outside the magnet by surrounding the tube with a mu-metal shield and three concentric sections of cast iron pipe. When one section of pipe and the mu-metal shield were used, the gain of the phototube decreased 10% after the magnetic field was turned on. No changes were noted in the gain when three sections of pipe were used. The light pipes varied in length from 5 to 10 ft and three possessed right-angle bends. The peculiar shapes were necessary to accommodate the counters to the magnet. In spite of the bends and long light pipes, light collection was sufficiently good that the target counter had a pulse height distribution corresponding to an average number of 25 photoelectrons for electrons passing through 1/8 in. of scintillator (see Fig. 12).

The last dynode outputs of the T and A counters were used to make the pion stopping coincidence, while the anodes of the same tubes were used to detect the positrons. The T and A anode signals were amplified in a fast amplifier by a factor of 7. These amplifiers could deliver a 6-volt pulse into a 50-ohm load with a 5-nsec risetime. The amplifiers also fanned out the signals, making it possible to do pulse height analysis on T and A simultaneously with fast logic. The electron counter outputs were amplified by a factor of 10 in a fast amplifier, which limited at 1 volt. The outputs of all counters or the amplified outputs were shaped and clipped by using Nevis fast discriminators. The pulse widths which were used to do logic are given in Table II.

TABLE II

Pulse Widths and Relative Timing

	Pulse Width (nsec)	Relative Timing
π^+	7	Reference
T^+	7	0 to π^+
A^+	70	50 nsec earlier than π^+
T^-	7	Reference
A^-	30	10 nsec earlier than T^-
E1	7	0 to T^-
E2	7	0 to T^-

Fast coincidences were made using the Nevis fourfold coincidences. The μ-gate was generated using Nevis slow logic. A block diagram of the detection electronics is shown in Fig. 13. The stopping pion was detected by a π^+T^+ coincidence in anticoincidence with A^+. The stopping π pulse generated a 2-μsec gate which was delayed by 0.5 μsec. The 2-μsec gate was used to gate on the positron telescope coincidence. A gated triple coincidence among T, E1, E2, which was in anticoincidence with A, was used to trigger a high voltage pulser which fired the spark chambers. The gate was delayed by 0.5 μsec to prevent scattered beam particles from triggering the chambers. Approximately 50% of the muons decayed during the gate. As a precaution to insure that the decay positrons did come from the pion which gated the $TE\bar{A}$, coincidence on, the $TE\bar{A}$ coincidence was gated off if another pion stop was detected in the pion telescope during the 2.5-μsec period after the first pion stopped. The $TE\bar{A}$ coincidence remains gated off for 5 μsec.

The output of the $TE\bar{A}$ coincidence is used to trigger a high voltage pulser which fires the spark chambers. The trigger circuit consists of a spark gap pulser and two spark gaps. The spark gaps can be run in excess of 40 pulses/sec for 20 x 10^6 pulses. The gap is made of copper electrodes and a tungsten firing pin. The final output pulse was a 6.4-kV pulse which was delivered at the chamber plates 175 nsec after the muon decayed. When the spark chambers were fired the $TE\bar{A}$ coincidence circuit was disabled for 25 msec. The $TE\bar{A}$ was also disabled if the 1401 was not ready to read data.

After the spark chambers had been pulsed, the transit times of the soundwave from the spark to the microphone in the chamber were measured. After 2 msec the data unit transmitted data to the 1401 memory. Data could be transmitted only when the 1401 was ready to read.

Throughout the experiment two pulse heights were continuously measured and transmitted to the 1401 with the sonic times. One of these was always the T^- counter. The pulse-height analysis was complicated by the presence of electrical noise from the spark chambers. The noise was eliminated by transmitting both the coincidence pulse and the T^- along low-loss cable from the cyclotron floor to a lab 1,000 ft away. The coincidence pulse, which is about 120 nsec earlier than the spark discharge, was used to gate a linear amplifier on for 50 nsec. During this time a peak detector sampled the T^- pulse which varied from 0.1 to 4 V. When the conducted noise from the spark discharge arrived 120 nsec later the linear amplifier was disabled. The spark noise was about 5 V and lasted for 1μsec. The remainder of the pulse-height analyzer was a standard height-to-time converter and pulse stretcher. A block diagram of the pulse-height-analyzer is shown in Fig. 14. A 1 V pulse was converted to a pulse of 100-μsec duration. The trailing edge of this pulse was differentiated, delayed by 60 μsec, and sent back to the cyclotron floor where it was handled in the same way as a microphone output. The pulse-height-analyzer was linear to several percent.

During the experiment the pulse-height-analyzers were checked for low-voltage cutoff, gain, and linearity. The results of tests of linearity of the pulse-height analyzer are given in Figs. 15 and 16. A pulse-height distribution for all gated positrons is shown in Fig. 12. The point at which the distribution falls to half the maximum value corresponds to the case of a positron traversing the full thickness of the scintillator. This connection was established experimentally by sampling pulse heights from positrons coming from the A counter, which must traverse the full thickness of T.

E. Outline of Experimental Runs

Data were taken at eight field settings. At 6.6 kG 6×10^6 events were taken; at this field setting the μ-decay endpoint could be seen. At 7.2 kG 2×10^5 events, and at 7.7 kG 2×10^5 events were taken. The purpose of this data was to measure the endpoint in different parts of the magnet, and thus check both the field and the spark chambers. At 5.3 kG 3×10^6 events were taken to provide a check of the 6.6 kG data and to provide data at the lower part of the spectrum. At 4.4 kG 1×10^6 events were taken, and at 2.6 kG and 2.0 kG a total of 0.2×10^6 events were taken for the purpose of providing data at the lower part of the spectrum. A study of the π-e decay was made at 9.2 kG solely as a check of the spectrometer accuracy.

In addition to 6×10^6 events which were taken at 6.6 kG another 1.2×10^6 events were taken with 3/8-in. plastic scintillator placed above the target counter. This permitted an experimental measurement of the combined brehmmstrahlung and the ionization loss. At the three main field settings, 6.6, 5.3, and 4.4, checks were made of the electronics to measure accidental rates. Approximately 2 x 10^5 events of this type were recorded.

IV. SONIC SPARK CHAMBERS AND SOUND RANGING

A. Theory of Operation

When a spark chamber is pulsed and breakdown occurs, not only is a spark visible but there is a sound wave which can be detected by a microphone. The time interval from the instant the spark is generated until the instant the sound of the spark is detected by a microphone is almost proportional to the distance between the spark and microphone. The speed of sound in neon, the gas usually used for spark chambers, is 0.5 mm/μsec. To measure a distance of 50 cm to 0.5 mm it is necessary to measure 1 msec to 1 μsec. In practice with standard electronics time resolutions of 0.050 μsec are achieved easily. The accuracy of this measurement is limited by the risetime of the microphone pulse and the acoustical wave, both of which are of the order of 1 μsec.

The first experimentalists to use the sound of the spark to measure position were Fulbright and Kohler of Rochester University.[22] Independent of this work Kirsten and Maglic devised a sonic spark chamber and demonstrated the feasibility of using it in a high rate experiment.[23] On the basis of the success of these devices, a sonic spark chamber was built at the Nevis Laboratories in September 1962. The Nevis chambers are single-gap spark chambers with four microphones mounted inside the chambers. An assembled chamber, shown in Fig. 10, consists of a rectangular brass frame to which thin foil electrodes are attached. The microphones are held in brass brackets which are in turn mounted on the inside walls of the frame.

The microphones form a rectangle of sides 2a and 2b, as shown in Fig. 17. The most natural set of coordinates to describe the location of a particle track are the perpendicular bisectors of the sides of the rectangle. The intersection of the bisectors is the origin. The x coordinate axis is parallel to the side formed by microphones 1 and 3, and the y coordinate axis is parallel to the side formed by microphones 1 and 2.

ARRANGEMENT OF MICROPHONES IN A SONIC CHAMBER

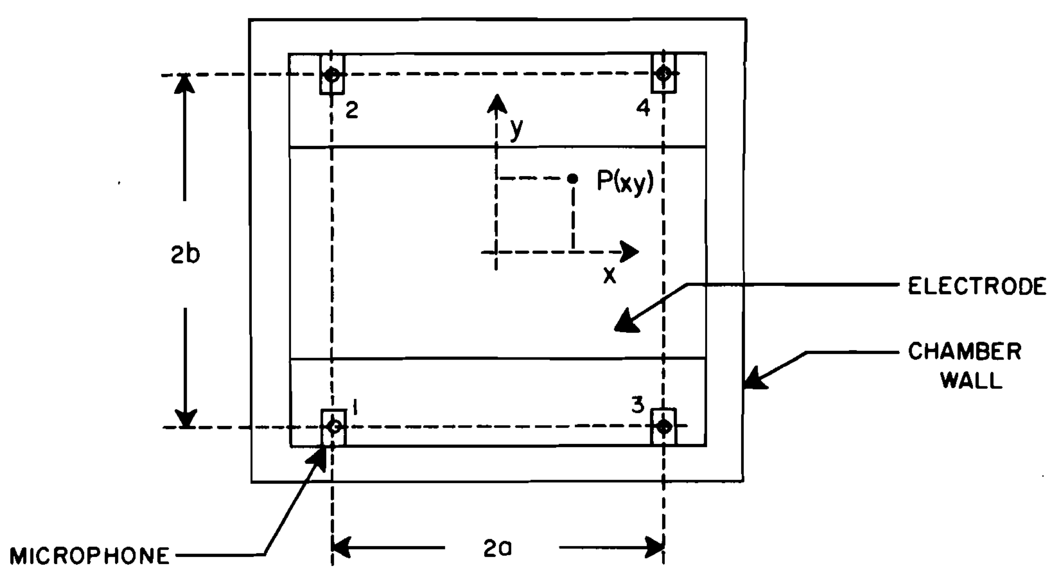

FIG.17

Fig. 17 Arrangement of Microphones in a Sonic Chamber

The relationship between the distance traveled by the sound wave and the time of propagation is given approximately by

$$d = Vt + K \tag{10}$$

d is the distance between the microphone and the spark; V is the velocity of sound in the gas; t is transit time of the soundwave between spark and the microphone; and K is a constant which accounts for the fact that during the first centimeter of travel the speed of the disturbance is greater than V.

When the spark is generated the average kinetic energy of the particles is much greater than the average kinetic energy of the particles in the remainder of the gas. Since the electrical discharge lasts for a time which is less than 250 nsec, the particles in the gas do not diffuse outward during the discharge and their density is the same as the bulk gas. If the average kinetic energy per particle in the spark is kT_S and the average kinetic energy per particle in the gas is kT_O, then the pressure difference at the time of the formation of the spark is

$$(P_S - P_O) = \rho Nk(T_S - T_O) \quad . \tag{11}$$

The disturbance will be approximately cylindrical. If the energy in the disturbance is considered to be constant, then as the disturbance spreads out the pressure decreases. If $P_S(r)$ is the pressure in the disturbance after it has spread out a distance r and if the energy density within the disturbance is uniform, then $P_S(r)$ is given by

$$P_S(r) - P_O = \rho Nk(T_S - T_O)\frac{c^2}{r^2} \quad . \tag{12}$$

c is the radius of the spark after the electrical discharge stopped. As long as the excess pressure is large the disturbance will be propagated with a velocity greater than the speed of sound. Once the excess becomes relatively small, that is $\left(\frac{T_S - T_O}{T_O}\right) \frac{c^2}{r^2} < 1$, the disturbance will be propagated with speed of sound. The distance K at which this is true is given by

$$K \approx \left(\sqrt{\frac{T_S - T_O}{T_O}}\right) c \approx \sqrt{\frac{f(C_D V_D{}^2)}{kT_O}} \tag{13}$$

If c is taken to be 1 mm, the typical width of a spark on a photograph and if T_S is about 1 eV, the value of K will be about 1 cm. It is of importance to note that the disturbance propagates with the speed of sound after 1 cm or so. From Eq. (13) it can be seen that K varies as the square root of the kinetic energy of the particles in the discharge. The kinetic energy of the discharge depends in turn on the energy stored in the discharge capacitor, $1/2(C_D V^2)$. While the energy dissipated in the spark is not a constant fraction of the energy stored in the discharge capacitor, it does depend only on the voltage to which the capacitor is charged, the capacitance, and the time response of the high-voltage triggering circuit. As long as these quantities are kept constant, K can be kept constant. In practice the charging voltage was kept constant to a few percent. An equivalent form of Eq. (10) is

$$d_i = V(t_i + t_p) \quad . \tag{14}$$

t_i is the time interval which was measured for the i^{th} microphone. The time interval, which begins 60 μsec after the spark chambers are pulsed, is measured by scaling a 5-Mc oscillator. The relationship between t_p and K is further modified by the finite size of the detector. The relation between K and t_p is given by

$$t_p = 300 + \frac{K + R_d}{V} \quad \text{(units of 1/5 } \mu\text{sec)} \tag{15}$$

R_d = radius of the lead zirconate cylinder .

The times measured by the acoustic pickups are related to the location of the spark by Eqs. (16) and (17).

$$x = \frac{V^2}{4a}\left[(t_1 + t_p)^2 - (t_3 + t_p)^2\right] = \frac{V^2}{4a}\left[(t_2 + t_p)^2 - (t_4 + t_p)^2\right] \tag{16}$$

$$y = \frac{V^2}{4b}\left[(t_1 + t_p)^2 - (t_2 + t_p)^2\right] = \frac{V^2}{4b}\left[(t_3 + t_p)^2 - (t_4 + t_p)^2\right] \tag{17}$$

Both x and y can be determined in two ways. The quantity DT, defined by Eq. (18), is zero for a single spark. It is therefore a test of the consistency of the measurement and an indication of whether more than two sparks are in the chamber.

$$DT = (t_1 + t_p)^2 - (t_2 + t_p)^2 - (t_3 + t_p)^2 + (t_4 + t_p)^2 \tag{18}$$

A second consistency check is given by the null quantity D:

$$D = (a + x)^2 + (b + y)^2 - V^2(t_1 + t_p)^2 \tag{19}$$

Using four microphones makes it possible to detect double sparks. DT is a good check on whether all transducers are working and it does not depend on V. D is then a check on V and, in addition, removes the few ambiguities which can occur in the DT check. For sparks near a microphone, DT is very sensitive to t_p; and thus t_p is determined from the experimental data by choosing a sample of these points, setting DT = 0, and then solving for t_p. Throughout the experiment t_p is checked for data samples. Since its variation is within the statistics of a single sample, one set of values is used for the data analysis. In a similar way, V is sensitive to points in the center of the chamber and it is checked in this manner.

The velocity of sound V is not a constant. V must be redetermined from time to time, for it cannot be controlled as is the case with t_p. The gas used in the chamber is a mixture of He and Ne which obeys the ideal gas law. The velocity of sound in an ideal gas is expressed by

$$V^2 = (\gamma R) \frac{T}{\bar{M}} \quad . \tag{20}$$

γ is the ratio of specific heats and R the ideal gas constant, T is the gas temperature and $\bar{M}$ the mean molecular weight. A 3° C change in T, which is not uncommon, will produce a 1% change in V^2. Such a change must be accounted for if the position of a spark is to be determined within 1/2 mm. The mean molecular weight can also change because the Mylar windows are more porous to He than Ne. The change in $\bar{M}$ is of more significance in practice than the change in T.

The velocity of sound is determined by a test spark, a pair of needles which are located at a fixed position, as shown in Fig. 16. If a large voltage is put across the needles a spark will be made and the velocity can be determined by

$$V = \left(\frac{d_3 - d_1}{t_3 - t_1}\right) \quad . \tag{21}$$

The advantage of using the test spark to determine V rather than the data from a real spark is that the test spark can be placed so that it is sensitive to V, while the real sparks occur throughout the chamber. In practice this relation was not used directly to get V, but it was related to an optical calibration.

B. Calibration of the Chambers and Bench Tests

The first check of accuracy of the spark chamber compares the position of the spark measured from photographs to the same position measured by the microphones. The relations used to compute the position are,

$$x = \frac{V^2}{4a} \left[\frac{(t_1+t_p)^2 - (t_3+t_p)^2 + (t_2+t_p) - (t_4+t_p)^2}{2}\right] \tag{22}$$

$$y = \frac{V^2}{4b} \left[\frac{(t_1+t_p)^2 - (t_2+t_p)^2 + (t_3+t_p)^2 - (t_4+t_p)^2}{2}\right] \tag{23}$$

X_{op}, the X coordinate of the spark as determined from the photograph, and X_a, the sonic measurement, are fitted by least squares to a relationship of the form:

$$X_a = \alpha X_{op} + \Delta X_{op} \quad . \tag{24}$$

X_{op} is measured from a fiducial mark on the spark chamber. ΔX_{op} is the distance from the optical fiducial mark to the center of the chamber. X_a is determined from the sonic times using Eq. (22) when $V^2/4a$ is set equal to 1. It is possible to fit the points (X_a, X_{op}) to a straight line by Eq. (24)

to an accuracy of 0.2 mm. The slope of this straight line, α, is $4a/V^2$ and hence determines V^2. V^2 can also be determined by an independent measurement which uses the test spark. According to Eq. (21), while the value of V^2 determined by the two methods differs by 1/2%, the ratio of the two measurements is almost independent of the value of V^2. A factor of two-change in V^2 changes the ratio by 3%. For normal conditions V^2 changes only by 10%. Over this range the ratio of the two methods for determining V^2 will be constant to 1 part in 1000. As a consequence, it is possible to determine the appropriate value of V^2 to use in Eqs. (22) and (23), by knowing the value of V^2 from the test spark and the ratio of the two values of V^2. In practice this is done by evaluating the quantity λ, defined by Eq. (25), which is proportional to the ratio of V^2 as determined from the two methods.

$$\lambda = \left(\frac{V^2}{4a}\right) \overline{(t_1 - t_3)^2}_{TS} \tag{25}$$

$\overline{(t_1 - t_3)}_{TS}$ is the average value of the difference in time for microphones 1 and 3 when the test spark is fired. By combining Eq. (24) with Eq. (21), it follows that λ should be equal to Eq. (26) and independent of V^2:

$$\lambda = \frac{(d_1 - d_3)^2}{4a} \tag{26}$$

Once the constant λ has been determined, the value of $V^2/4a$ can be obtained by continually monitoring the value of

$\overline{(t_1 - t_3)}_{TS}$. By repeating the optical calibration for a wide variation of the amount of He in the He-Ne gas mixture in the spark chamber, it is possible to change V^2 by a factor of 2. The values of $V^2/4a$ and λ are determined for each gas mixture by an optical calibration. t_p is measured by using Eq. (18) with DT set equal to zero. By choosing sparks only near the microphone, t_p can be measured quite well. The practice determines t_p for each optical calibration. The results of these calibrations are presented in Table III.

TABLE III

Bench Tests of 14 in. x 10 in. Sonic Spark Chambers
August 1963

Run No.	Chamber I		Chamber II		Chamber III	
	$V^2/4a$	λ	$V^2/4a$	λ	$V^2/4a$	λ
1	0.826	0.444	0.522	0.445	0.515	0.452
2	0.920	0.444	0.546	0.446	0.510	0.452
3	0.517	0.460	0.607	0.445	0.578	0.449
4	0.512	0.461	0.517	0.444	0.515	0.452

The data show that λ varies very slowly with V^2. In the course of the experiment the extreme variation of V^2 was about 10%. Over this range of V^2, λ can be considered to be a constant. These tests demonstrate that the chambers could locate a spark to 0.2 mm when calibrated with optical measurements. Moreover, by determining λ the V^2 of the spark chamber could be determined as a function of test spark times. The systematic error due to the slight variation of t_p with distance, and other such errors are eliminated to first order by the calibration procedure.

A second set of bench tests was performed by arranging the four chambers one on top of the other in an Aℓ frame machined by 0.001 in. A photograph of the setup which shows the sparks due to a β from Y_r^{90} decay is shown in Fig. 18. Approximately 100 pictures were taken and measured. The absolute location of the x coordinate was referenced to fiducial marks on the Aℓ frame.

TABLE IV

Bench Tests of the Sonic Chambers Used in the Experiment
April 1964

Chamber	t_p	$V^2 \times 10^5$ (cm^2/t^2)	ΔX_{op} by Machinists Measurements (in.)	ΔX by Calibration (in.)
I	370	8.774	0.037	0.036
II	375	8.936	0.069	0.071
III	380	8.915	0.069	0.066
IV	380	8.921	0.099	0.097

The location of the center of the spark chamber is not dependent on V or t_p, but depends only on the location of the microphones. These were mounted in brackets, an example of which is shown in Fig. 19. The microphone is held in place in the bracket by a rubber O-ring. The bracket itself is pinned accurately to the frame. The location of the center of the chamber, ΔX_{op}, was computed from the bracket locations. These locations were given on the basis of the machinists' measurements of the mounting holes. The data show that there was no slip of the microphones in the O-rings, as the relative positions of the centers from one chamber to another agree to within 0.005 in. The absolute location deviation reflects the accuracy of the optical system. These comparisons indicate how well sparks in separate chambers were measured relative to one another in the experiment.

To check how well the calibrated sonic chamber worked, a separate experiment was carried out using cosmic rays. The chambers were arranged as shown in Fig. 20. Cosmic rays passing through the chamber were detected by scintillation counters. In order to minimize multiple scattering in the spark chambers only cosmic rays which had penetrated 7-in. lead were used to trigger the chambers. This set a cutoff of 250 MeV/c in momentum. The quantity ΔX defined by Eq. (27)

$$\Delta x = \frac{(X_I - X_{III}) - 2(X_I - X_{II})}{2} \tag{27}$$

is the deviation of the spark in Chamber II from a straight line through the sparks in Chambers I and III. Because multiple scattering is neglible, the deviation can only depend on the sonic measurement error. The positions were computed using $V^2/4a$ and $V^2/4b$, which correspond to the times measured by the test spark. $(\overline{\Delta x^2})^{1/2}$ was found to be 0.3 mm. Figure 21 shows a histogram of Δx. The width of this distribution depends only on the accuracy of the spark chambers and hence is a measure of the accuracy of each chamber. It reflects the cumulative error of the single measurement, the test spark, and the calibration. It is not a fitted result.

The data of Table V obtained by photographing the chambers in the magnet during the experiment, provided the calibration for the data obtained in the experiment. It represents the most extensive calibration carried out as 300 pictures were taken and measured. The value of σ is poorer only because the camera was much further away than in the bench tests.

TABLE V
Experimental Calibration
July 1964

	Chamber I			Chamber II		
Run	$V^2 \times 10^3$ $(mm/unit\ t)^2$	λ $(mm)^2$	σ mm	$V^2 \times 10^3$ $(mm/unit\ t)^2$	λ $(mm)^2$	σ mm
9902	8.88	4367	0.23	8.88	45930	0.30
9904	8.87	4346	0.25	8.89	45910	0.27
9906	8.91	4360	0.27	8.89	45870	0.23
9913	9.21	4361	0.27	9.13	45710	0.27
9916	9.22	4372	0.27	9.14	45840	0.23
9921	9.75	4389	0.32	9.65	45849	0.23
	Chamber III			Chamber IV		
9902	8.85	45070	0.27	8.80	20130	0.25
9904	8.86	45050	0.30	8.81	20130	0.15
9906	8.87	45090	0.20	8.81	20130	0.25
9913	9.11	44970	0.32	9.09	20120	0.23
9916	9.12	45050	0.32	9.13	20290	0.23
9921	9.59	44976	0.27	9.57	20230	0.23

V is the velocity in mm/0.2 μsec, λ is a constant, σ is the standard deviation of the fit of a straight line to optical and sonic measurement.

C. Description of a Typical Chamber

The sonic chamber is a one-gap spark chamber with four microphones mounted on the walls inside the chamber. The microphones are cylindrical shells of lead zirconate which are silvered inside and out. The outside diameter is 1/8 in., the inside diameter 1/16 in., and the length 1/2 in. The cylinder, together with a brass cap and fitting, is soldered to a piece of thin coaxial cable. The coaxial mounting reduces the pickup of the spark discharge to tolerable levels. The brass cap and fitting are grooved so that a small rubber O-ring may be slipped on. A photograph of a microphone, its cable, and the mounting fitting is shown in Fig. 19. The microphone is held in position in a brass bracket mounted on the wall of the chamber. The brackets are held in place by nylon screws, which provide support and shock isolation. The spatial location of the bracket is determined by a milled slot into which the bracket slips.

The screws and rubber O-rings effectively isolate the microphone from wall vibrations. The microphone signals are brought out of the chamber by coaxial feed-throughs mounted on the front wall. Also mounted on the front wall are two valves which permit gas to be circulated through the chamber.

The electrodes of the spark chamber are 0.001-in Aℓ foil stretched on stainless steel frames. The windows of the chambers are 0.003-in. Mylar. All seals are made with O-rings. The chambers are leaktight to freon leak detectors, although He will diffuse through the windows. The test spark, a pair of tungsten electrodes mounted on a lucite bracket, is attached to the inside wall.

The brass frame of the chamber was machined to 0.001 in. tolerances. The microphone bracket holes were drilled after the brackets were in place, so that the centers of the holes would be positioned to ± 0.001 in. The use of rubber O-rings to position the microphone reduces the precision of the mounting somewhat, but the error introduced is less than 0.005 in. The important dimensions of the chambers used in the experiment are given in Table VI.

TABLE VI

Spark Chamber Dimensions

Chamber	Plate Area (in.)	2a (cm)	2b (cm)
I	$5\frac{1}{2}$ x $5\frac{1}{2}$	14.290	21.433
II	14 x 10	34.290	35.687
III	14 x $11\frac{1}{2}$	34.290	36.195
IV	12 x 12	29.210	41.275

D. Sonic Spark Chamber Electronics

The sonic data system measured the transit times of the soundwave to the microphones, converted the measurements to digital form, and wrote the digital data on tape. The hardware is composed of two parts, an IBM 1401 computer and a sonic data unit. The sonic data unit was designed and made at Nevis. A description of its operation is given in this section, with a number of details placed in Appendix III.

The time intervals between the generation of a spark and the arrival of the soundwave at the four microphones were measured and written on magnetic tape by the following sequence of operations:

1) After a delay of 60 μsec, a set of 5-Mc oscillators were gated on by the spark chamber trigger pulse and then gated off by the amplified microphone pulse.
2) During the time interval that each oscillator was gated on, it was scaled by a separate four-digit coded decimal scalar.
3) The digitized time intervals were transmitted to the 1401 memory one digit at a time. Transmission of digits to the 1401 was stopped after all time intervals were read.
4) The process was repeated until n such events have been read into the 1401 memory; then the data in the memory was written on magnetic tape as a single record. The number n was controlled by the 1401 program. (During the experiment n was 12.)

The block diagram of Fig. 21 shows schematically how each of the first three operations are carried out. The fourth operation is controlled by the 1401 and its program. The measurement of the time interval and its subsequent conversion from analog to digital form is done by the time interval channel. Data transmission to the 1401 memory is controlled by the main control chassis and the 1401 control chassis.

Aside from the microphone detector and its amplifier the electronics is typical of any 5-Mc saturated switching logic. The properties of the microphone and the amplifier were matched so that the system would be sensitive to only the soundwave and not extraneous vibrations.

The soundwave is detected by a lead zirconate cylindrical shell which generates a potential difference across the shell when it is struck by the soundwave. The output of a microphone, which is of the order of 1 mV, is amplified by a factor of 1000 and the amplified pulse is the digitron stop pulse. Figure 23 shows a transducer pulse after amplification. The 1-μsec rise of the pulse is due to the response of the high frequency vibration mode of 500 kc of the lead zirconate cylinder and the spatial definition of the soundwave. The ringing at 500 kc shows that this mode is excited directly by the sound wave. A second mode of vibration at 50 kc is set into vibration if the holding bracket is made to vibrate, and it is also set into vibration by the coupling between the two modes. The bracket will vibrate if a soundwave strikes the brass frame. This can be serious since a soundwave can strike the brass frame and then travel through the frame to the bracket. Because the speed of sound in brass is ten times greater than in neon, the soundwave can reach the microphone by this path before the soundwave in neon reaches the microphone. The amplifier is designed to pass the high frequency mode and reject the low frequency mode. The half-power points of the output are roughly 100 kc and 2000 kc. A block diagram of the amplifier and time interval flip-flop is given in Fig. 24.

After the pulse has been amplified it is fed into one side of a differential amplifier which is biased by an exponentially decaying pulse. The output of the differential amplifier is used to reset a flip-flop which stops the 5-Mc oscillator. The purpose of the exponentially decaying pulse is twofold. First, it gates the discriminator off when the spark chamber is fired; and second, it provides a time-varying discrimination level, thus making it possible to stop the 5-Mc oscillator at the same point on the rise of the microphone pulse, irrespective of where it comes from in the chamber. The pulse height of the microphone pulse is a function of distance and varies inversely as d(exp αd) $\cdot$ $\alpha \approx 1 \times 10^{-3}$/cm. A graph of the amplified microphone pulse height vs time is shown in Fig. 25.

Two milliseconds after the spark chambers are fired, data acquisition is complete and all 5-Mc clocks not stopped at this time are stopped by the disappearance of the amplifier gate pulse. In this experiment the largest possible transit time was less than 1 msec. The end of amplifier gate pulse starts the data-reading sequence which is shown in block diagram in Fig. 26. This pulse generates a service request which is sent to the 1401. If the 1401 is ready to read the data stored in the scalars of the sonic data unit, a read-call level is present and the sonic data unit puts the first digit on the five data lines to the 1401. These lines are an 8, 4, 2, 1, and a parity line. The 1401 reads these lines, sends a clock pulse to the sonic data unit, and stops to await the next digit. The 1401 clock pulse moves the step sequence to the next position, thereby bringing the next digit on to the data lines. The 1401 clock pulse also gates the service request off for its duration, thereby providing the time in which to move the next digit onto the data lines. After the 1401 clock pulse is over a new service request is generated and the 1401 reads the data, generates a second clock pulse, and then stops to await the next digit. This sequence is repeated until the last digit has been transmitted. At this time the step sequence generates an end of transmission pulse which the 1401 recognizes, and permits it to carry out the next step in its stored program. Total time to acquire and read the data is 3.5 msec. The 1401 program used in this experiment carries out a series of computations between events which last 20 msec. A discussions of the operations carried out by the 1401 is given in Sec. VI, while finer details of the operation of the sonic system are given in Appendix II.

The advantage of the sonic spark chambers over conventional spark chambers which use optics and photography to determine spark positions is striking. An excellent optical system and excellent measuring can locate sparks to 0.25 mm in space, while the sonic system can locate sparks to 0.30 mm in space. The accuracy of each system is roughly equivalent. In the sonic system data can be put into a computer within 4 msec after the event occurs and it is ready to be processed; moreover, as soon as the chambers can be pulsed again it can handle another event. Event rates of 60/sec were achieved using a β-source. The conventional system is limited by camera drive speeds to a few pictures a second.

V. CONSTRUCTION OF A THEORETICAL MUON DECAY SPECTRUM

A. The Choice of a Theoretical Model

The theoretical model to which the experimental results were compared is the four-fermion contact interaction given by Eq. (5). A consequence of Eq. (5) is that the decay spectrum can be described by a simple polynomial in the electron momentum as given by Eq. (9). For unpolarized muon decays this polynomial is characterized by only two parameters, ρ and η. The details of the interaction between the four fermions is contained in ρ and η. While the simple polynomial must be modified to include radiative corrections, it is still characterized by the parameters ρ and η. As long as the results of an experiment are presented in terms of ρ and η, the ordering of the lepton fields is immaterial. When an interpretation of a particular set of values of ρ and η is made in order to obtain limits on the fundamental coupling constants, the ordering of the lepton fields is crucial. For this reason the ordering can be ignored temporarily and will be until an interpretation of the experimentally determined values of ρ and η is made in Sec. VIII. The remainder of this section will be devoted to the modifications which must be made to Eq. (9).

Large non-local effects can be ignored because there is no evidence for their existence. Small non-local effects can be included into Eq. (9) as their dominant effect causes small changes in ρ and η. A plausible means of introducing a non-locality is to couple the weak interaction current, J_α, to a massive spin 1 particle, W. The weak interaction lagrangian becomes

$$\mathcal{L} = g\, J_\alpha W^\alpha \qquad g = M_W \sqrt{G_f} \tag{28}$$

W^α is the vector field describing the boson and M_W its mass. In this case the observed weak interaction processes are all second order. A further consequence of the spin 1 particle is that it will have the effect of increasing the observed Michel parameter by the amount

$$\Delta\rho = \frac{1}{3}\left(\frac{M_\mu}{M_W}\right)^2 \tag{29}$$

The original motivation for the experiment described here was to detect the existence of that correction. Since the start of this experiment a number of other experiments have placed a lower limit on the mass between 2.0 and 4.0 BeV.[24,25] For such a lower limit on the mass the correction to ρ is less than 0.001, and thus beyond the accuracy of the experiment.

B. Internal Radiative Corrections

The modifications to Eq. (9) to account for the internal radiative corrections have been computed by using the minimal electromagnetic interaction which is known to be applicable to both the muon and electron.[1] These corrections to order α^2 are described by the following Feynman diagrams:

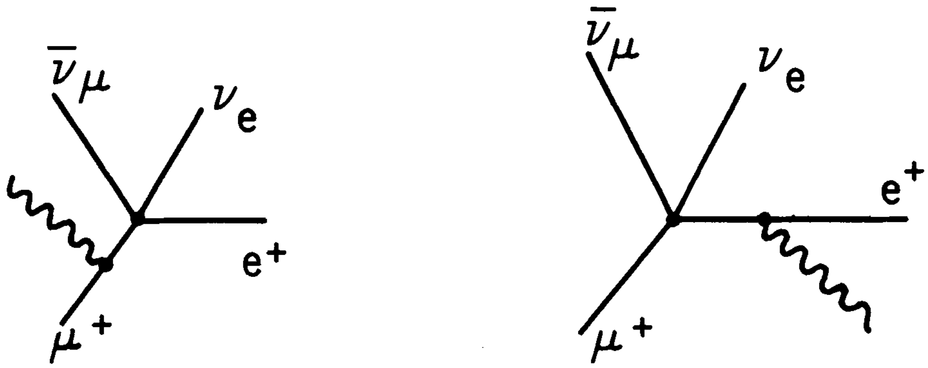

Diagrams A_1 and A_2 contribute because the apparatus does not distinguish the cases in which photons are emitted from the case in which they are not.

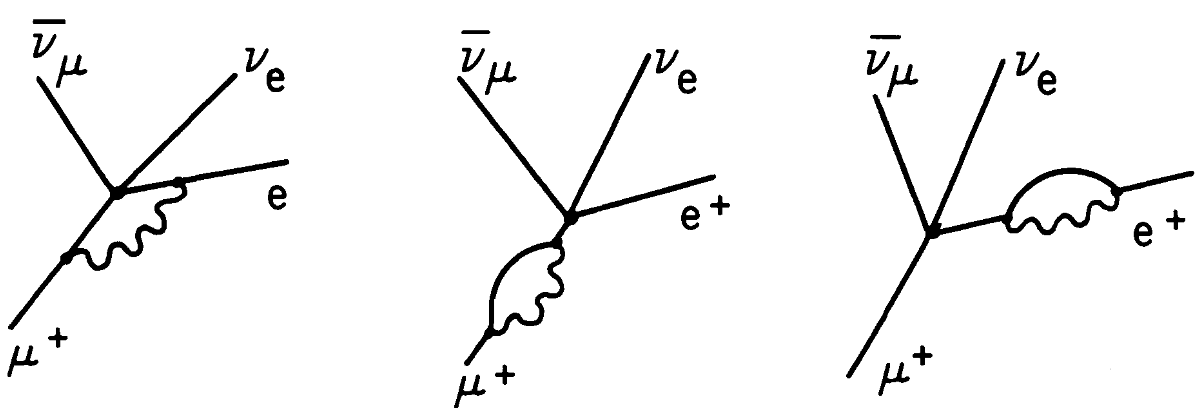

Diagram B_0 is the unmodified graph, while Diagram B_1 is the vertex modification, and B_2 and B_3 are the mass renormalization graphs.

The calculation can be carried out in a convergent manner in only one case, the case of V-A theory.[1] The calculation has also been done for the case of the intermediate boson. The difference between a local theory and a boson theory is small and varies as $(M_\mu/M_W)^2$.[26] For other types of coupling the results are divergent. For a cutoff of M_p the results are roughly independent of the exact nature of the weak vertex. As a V-A theory is at least correct to 1%, the radiative corrections for this theory were used. The results modify the spectrum in the following manner:

$$\frac{dN}{dx} = x^2\left\{\left(\frac{1}{1+\frac{4m_e}{m_\mu}\eta}\right)\left[3(x-1)+2\rho\left(\frac{4}{3}x-1\right)+6\frac{m_e}{m_\mu}\eta\left(\frac{1-x}{x}\right)+\frac{\alpha}{2\pi}f(x)\right]\right.$$
$$\left. - \xi p \cos\theta\left[1-x+2\delta\left(\frac{4}{3}x-1\right)+\frac{\alpha}{8\pi}g(x)\right]\right\} \tag{30}$$

$\frac{\alpha}{2\pi}f(x)$ and $\frac{\alpha}{2\pi}g(x)$ are integrals which give corrections of a few percent throughout the spectrum, except at $x = 1$ where they are divergent. The difficulty arises from the fact that the S-matrix for μ decay has been expanded in terms of one emitted photon, two emitted photons, etc.

The divergence can be overcome formally by including an experimental resolution which allows the integrals for $f(x)$ and $g(x)$ to converge. The inner bremsstrahlung process, the sum of diagrams A_1 and A_2, has been checked experimentally and is in agreement with the V-A theory to the accuracy of the experiment.[27]

The use of radiative corrections for a pure V-A theory, while retaining a spectrum which was derived from a more general hamiltonian, is a questionable procedure. The justification for this approach is due in part to the fact that the radiative corrections are not sensitive to the exact form of the interaction, and in part to the historical precedence that this means of reporting the data has had. The radiative corrections are the largest corrections which must be made. The error which would be introduced in ρ by neglecting these corrections would be to lower it by 0.04, when a fit is made for the region $0.3 \leq x \leq 0.95$. Above $x = 0.95$ the corrections become increasingly large and therefore this region of the spectrum provides a sensitive test of these corrections.

C. Modifications of the Theoretical Spectrum Introduced by the Measurement

Several additional corrections were made to the spectrum of Eq. (30) to account for some of the features of the experimental apparatus. Each of these corrections has the property that it cannot be accounted for on an event-by-event basis. To remove their effects from the experimental data would have required a difficult and tedious numerical solution of a set of integral equations, whereas the effects can be included in the theoretical spectrum by a direct numerical integration. These corrections were as follows:

1. Bremsstrahlung in the target counter, the first window of the vacuum chamber and spark chamber I.
2. Ionization loss in the first window of the vacuum tank, the wrapping of the target counter and the first spark chamber.

3. The effect of the finite resolution of the momentum measurement.

Most of the bremsstrahlung was generated in the target counter and it was the largest of the three corrections. Bremsstrahlung was treated in the limit of complete screening where γ, the screening parameter, is less than 1. If P is the energy of the photon, E_o the initial electron energy, and E the final energy, γ is given as

$$\gamma = \frac{100(M_e)}{(E+k)} \left(\frac{k}{E}\right) Z^{-1/3} \tag{31}$$

The cross section per unit energy of a photon of energy k in this approximation is

$$d\sigma = 4Z^2e^2r_o^2 \left(1 + \left(\frac{E}{E_o}\right)^2 - \frac{2}{3}\left(\frac{E}{E_o}\right)\right) \log\left(183\ Z^{-1/3}\right) \frac{dk}{k} \tag{32}$$

The probability that a positron will lose energy in the interval k to k+dk after passing through a thin piece of material is dW(k).

$$dW(k) = \left(\frac{N_o}{A}\right) \rho \ell d\sigma \ . \tag{33}$$

The effect of the finite thickness of the target counter was included by using the Bethe-Heitler formula[28] given in Eq. (34).

$W(b\ell, Y)$ is the probability that the positron would have an energy $E_o e^{-y}$ or more after traversing a sample of thickness ℓ.

$$W(b\ell, y) = \frac{(b\ell-1, y)!}{\Gamma(b\ell)} \tag{34}$$

$$y = \ell n(E_o/(E_o-k)) \ .$$

If bremsstrahlung losses were ignored the observed value of ρ would have been lower by 0.007 than the actual value of ρ. The bremsstrahlung correction diverges at the endpoint. This like those in the inner bremsstrahlung, is an infrared divergence. Of some importance is the fact that the correction is very important for $x > 0.95$ and small below this region.

For positrons (or electrons) the average energy loss due to ionization is not the most probable energy loss and it is possible for a positron to lose all its energy in a single collision with an electron. Because there is a significant chance that a positron will lose several times the most probable energy loss, the detailed shape of the distribution of the energy losses must be taken into account.

The losses due to ionization in the target counter wrapping, Chamber I, and the first vacuum tank window were taken into account by using the Landau distribution.[29] If only the average energy loss in these materials had been considered and the shape of the probability distribution of energy losses had been ignored, the measured value of ρ would have been low by 0.002. Ionization losses in the active part of the target counter were corrected on an event-by-event basis.

The finite resolution of the spectrometer is accounted for by folding in a gaussian with a width consistent with the experimental resolution at the endpoint. It is not necessary to consider the momentum dependence of the resolution since the effect of finite resolution is important only within a few standard deviations of the maximum energy.

The theoretical spectrum which was compared with the experimental data is the sum of two parts. The first part is the spectrum for the case $\rho = 3/4$ and $\eta = 0$. This part is obtained by folding into Eq. (30) all the corrections discussed in Sec. V-C. The second part represents the difference between the spectrum for which $\eta \neq 0$ and $\rho = 3/4 + \Delta\rho$ and the spectrum for which $\rho = 3/4$ and $\eta = 0$. The difference of two spectra contains no interval radiative corrections but does include all other corrections discussed in this section. An important feature to be noted about the corrections made to the simple theory of Eq. (9) is that these made very large changes to the spectrum above $x = 0.95$. While it would be possible to get a good fit to experimental data for the momenta below this momentum, even if the corrections were ignored or made improperly, it would not be possible to get a good fit to the momenta above 0.95 unless the corrections were included and made properly. Thus, a good fit to experimental data over the whole momentum spectra is evidence for the validity of the corrections.

D. Bhabba Scattering in the Target and Positron Annihilation

No corrections were made to the theoretical spectrum to account for energy loss in the counter due to ionization, since the pulse height was used to correct each event in the experimental spectrum. The pulse height measured the positron energy loss correctly only when no secondary electrons had escaped. Secondary electrons were produced when a positron transferred more than 0.2 MeV kinetic energy to an electron in the target. The following analysis shows that when a secondary electron was produced, the event was rejected either because the pulse height exceeded the maximum acceptable value (0.54 MeV) or a double spark occurred in Chamber I. The secondary electrons must have had at least 0.2 MeV kinetic energy to have escaped the target. If it had less energy it would always have been deflected back into the counter by the magnetic field. If it had an energy of more than 9 MeV, it would have made a double spark in Chamber I. There was a probability of 5% that a secondary electron would acquire a kinetic energy between these limits by positron-electron scattering. However, the probability it acquired this energy and emerged from the counter with at least 0.2 MeV is 0.5%. Of the electrons which escaped, 80% were either deflected back into the counter or caused a double spark in Chamber I. Electrons which made more than one traversal of the target counter had a pulse height which exceeded the maximum limit and the event associated with this electron was rejected. These two effects caused the rejection of more than 98% of the events which contained a secondary electron with a kinetic energy of more than 0.3 MeV; as a result no correction must be made for the events which were retained. There was a small momentum dependence of the fraction of the events rejected, and thus a small bias was made in the selection of events. This bias is considered along with other systematic errors in Sec. VII.

Positron annihilation in flight was not taken into consideration when the theoretical spectrum was made. When annihilation took place in the target counter, the spectrometer, or the E1 counter, there was no event trigger. The fraction of positrons which annihilated was about 1/2%. The number of annihilation events depends on the positron energy and hence a small correction must be made. The correction is made in Sec. VII.

VI. CONSTRUCTION OF THE EXPERIMENTAL SPECTRUM

A. Data Processing and Editing

The fact that 10^7 events had to be processed by a computer made it necessary to use data-processing techniques that are out of the ordinary routine encountered by physicists. FORTRAN because of its slowness in handling I/O and executing BCD-to-binary conversion was entirely unsuitable for the data processing. Four different machine language programs were written and the average time to run an event through all the programs was 15 msec. The programs can be separated into three categories according to their function, as follows:

1. Editing;
2. Geometric reconstruction of the trajectories;
3. Histogramming .

The programs are described briefly in the following paragraphs and in somewhat more detail in Appendix III.

a. Approximately 8% of the events had more than one missing spark and are therefore without any value.

b. Blocks of events could not be processed because of occasional failures in the computing machinery of sonic spark chamber electronics.

c. The 7094 computer on which geometric reconstruction was done is a fixed word length binary computer, while the 1401 is a variable length word BCD computer.

For these three reasons, primarily the last, the raw data tapes, which were written by the 1401, were edited on the 7094 and rewritten in binary form. During the editing each input data record was checked for its form and its identity with the previous event. Events which had either the wrong form or which were identical with the previous event were rejected. Of the remainder of the events those which had no sparks missing were written on one binary output tape and those which had a single missing spark were written on a separate binary output tape. Approximately 6% of events had only one missing spark and these events were used solely to study spark chamber efficiency.

B. Geometric Reconstruction

After editing each event is reconstructed and the result is written on tape. The coordinate position of the spark within each chamber, x_i and y_i, are computed using Eqs. (22) and (23). The chamber coordinates are transformed to space coordinates of the coordinate system shown in Fig. 27.

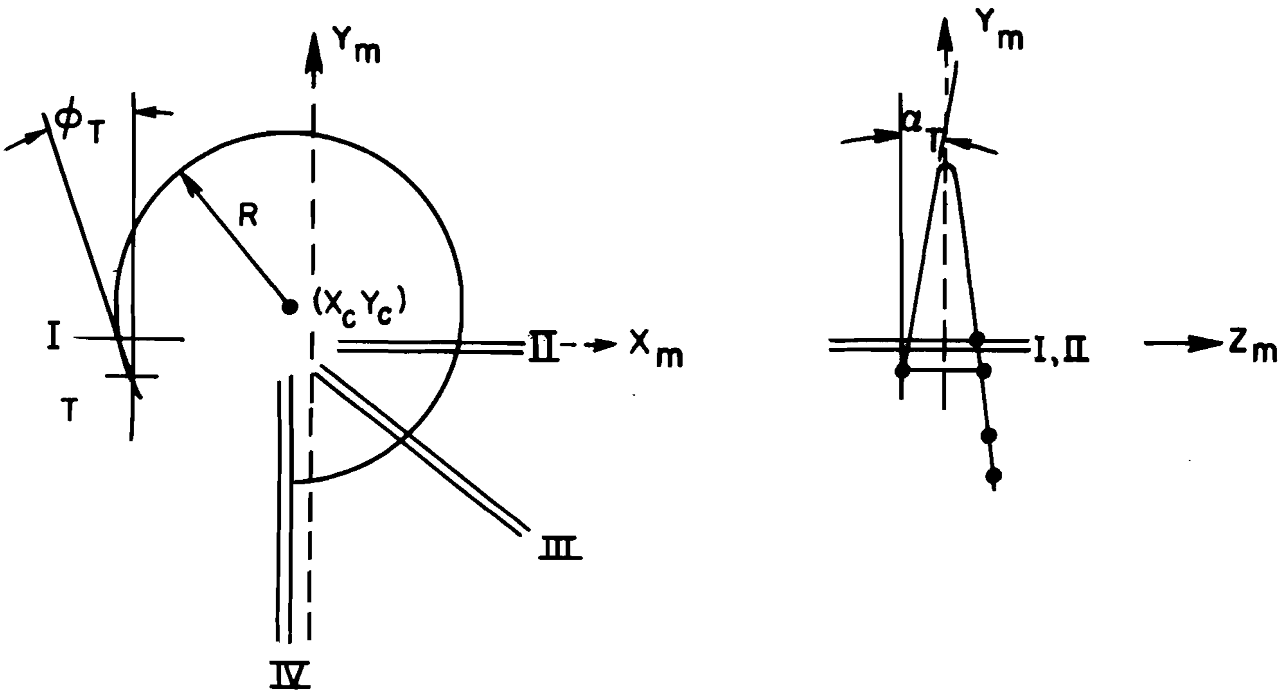

Fig. 27 Space Coordinates Used for Trajectory Reconstruction

z_m The coordinate axis which is parallel to the magnetic field

x_m The coordinate axis which lies in the plane of the high voltage plate of Chamber II and is perpendicular to z_m. $x_m = 0$ is located at a point in Chamber II.

y_m The coordinate axis perpendicular to x_m and y_m, which lies in the plane midway between the pair of microphones 1 and 3 and the pair 2 and 4 in Chamber II.

x_c, y_c The center of the circle in the space coordinate system made by projecting the helical trajectory of the positron onto the x_m, y_m plane.

φ_T The angle made by Y_m with the tangent to the projected circle at its intersection with the target.

α_T The angle made by the tangent to the helix with the x_m, y_m plane at the target.

R The radius of the projected circle.

This figure also serves to define the angular coordinates, φ_T and α_T. A helix is fitted to the coordinates of the sparks in Chamber I and II and the x coordinate of Chamber III. This helix is projected into Chamber IV and the projected point is compared with the actual spark location. The difference between the projected trajectory and the actual spark location is used to eliminate the events in which the positron is scattered by the vacuum tank walls. There are three such differences; DZ3ACT, DZ4ACT, and DY4ACT; and they are the difference respectively between the projected and actual z coordinates in Chamber III and IV and the difference between the projected and real y coordinates in Chamber IV. The helix is corrected for the energy losses due to ionization in the material between the exit window of the vacuum tank and Chamber III. The principal effect of these losses is to cause an error in φ_T. The error in momentum due to these losses is proportional to $\sin\phi_I$; where ϕ_I is the azimuthal angle at Chamber I.

The momentum of the positron, when it emerges from the target counter, is computed from the radius of curvature and the mean magnetic field. No attempt was made to correct for field variations over a trajectory. The energy loss in the target due to ionization is corrected for by using the pulse height from the target counter. The relation between pulse height and the ionization loss was determined experimentally in the following manner. For each interval of pulse height the location of the endpoint of the spectrum was determined. The relationship between pulse-height interval and the shift in the endpoint was found to be linear for all statistically significant intervals of pulse height. The range of statistically significant intervals of pulse height spanned a shift of the endpoint of 0.7 MeV. This is approximately one and a half times the most probable energy loss for a positron traversing the full thickness of the counter. The results of this analysis are shown in Fig. 16. The endpoint in each case was defined as the momentum at which the population of the histogram was half the value of the population at 51.5 MeV/c.

DZ3ACT, DZ4ACT, and DR4ACT have gaussian distributions, the widths of which are functions of P and ϕ_T. DZ3ACT is due principally to multiple scattering, in the vacuum tank windows and spark chamber II. The scattering by a thin foil can be written as

$$\left\langle (\Delta X)^2 \right\rangle^{1/2} = \frac{\ell_p}{p\beta} f(t, t_o) \qquad (35)$$

ΔX is the displacement of a track due to a scattering by a material of thickness, t, and radiation length, t_o, ℓ_p is the path length of the track after the scattering. This can be applied to DZ3ACT by taking ℓ_p to be

$$\ell_p = P \left(\frac{dR}{dP}\right) \phi_{23} \qquad (36)$$

where ϕ_{23} is the arc subtended by the trajectory in going from Chamber II to Chamber III. Equation (35) can be written for positrons with small dip angles as

$$\left\langle (DZ3ACT)^2 \right\rangle^{1/2} = \frac{dR}{dP} \phi_{23} \ f(t) \ . \tag{37}$$

ϕ_{23} depends rather strongly on momentum. Since DZ3ACT is used as a criterion to distinguish between multiple scattering in the foils and scattering of the vacuum tank walls, the momentum dependence of ϕ_{23} must be factored out. If it is not done, the selection on DZ3 will introduce a bias favoring low momentum. The momentum dependence is eliminated by dividing by ϕ_{23}. To define

$$DZ3 = \left(\frac{dP}{dR}\right) \frac{DZ3ACT}{\phi_{23}} \tag{38}$$

dP/dR is retained to make it possible to use one criterion for all fields. When scattering in the gas is considered, t also depends on ℓ_p and a more complicated correction is made to include this effect and to correct for the fact that ℓ_p for the vacuum tank is not $R\varphi_{23}$. In a similar way DZ4ACT and DY4ACT are modified to give momentum independent descriptions of the multiple scattering. Histograms of these variables are shown in Figs. 28 and 29.

In addition to computing the dip angle, α, a new variable α' is introduced for the purpose of making histograms. At each point on the target counter the maximum useful range of α is 12°. This is the range of α within which all events in a selected range of ϕ and p are accepted by the spectrometer. The center of this range depends on the location in the target. In order to select the largest possible sample of events the variable α' which is defined by Eq. (39) is used in the selection criteria.

$$\alpha' = \alpha - \frac{Z_T}{125\ \text{cm}} \qquad (39)$$

By selecting events from a fixed region of α', each part of the target has a different solid angle, but this solid angle does not depend on momentum. A factor of two increase in useful data is obtained by this means.

After calculation, each event is truncated and written on tape at 250 events per record. Table VII gives a list of those events which are written on the "P tape" and the number bits assigned to each variable.

TABLE VII

Information Retained After Reconstruction

Variable	Range	Bits	Variable	Range	Bits
p	15 to 55 MeV	12	$(D1234)_{II}$	0 to 8×10^5 t^2	6
φ_T	-30^o to $+50^o$	9	$(D1234)_{III}$	0 to 8×10^5 t^2	6
α_T	-20^o to $+20^o$	9	$(D1234)_{IV}$	0 to 8×10^5 t^2	6
α'_T	-20^o to $+20^o$	9	XI		6
X_T	-4 to +4 cm	6	YI		6
Z_T	-4 to +4 cm	6	XII		6
DZ3	-2 to +2 MeV/c	6	YII		6
DZ4	-2 to +2 MeV/c	6	XIII		6
DR4	-2 to +2 MeV/c	6	YIII		6
PHI	0 to 1600	7	XIV		6
PH2	0 to 9999	5	YIV		6
$(D1234)_I$	0 to 4×10^5 t^2	6	Identification		12

If an event does not fall into the range given in Table VII, it is tested to see whether it falls in a range which is twice as large, and if the event is within the new range it is written onto a separate tape, the "rejected P tape". Events which do not fall within the enlarged range are discarded and a record is kept of the number of such events. Approximately 90% of the edited events are accepted for the "P tape".

At this stage the number of tapes is still too large to construct histograms without a prohibitive amount of time being used on the 7094. Therefore, the "P tapes" were edited by reducing the number of significant figures carried in each variable and by reducing the number of variables to 11. The P' tape, the result of this editing, is the tape from which the histograms are constructed. A description of the P' tape is given in Appendix III.

C. Selection of Events for the Experimental Spectrum

A partial selection of events is made at each stage of the computations. Events with missing sparks are rejected during the data-tape editing. During the geometric reconstruction, events which had double sparks in any chamber or which had sparks within 1/4-in. of the steel frame of the spark chamber plates were rejected. The double spark criteria were that D1234 could not exceed 4×10^5 in Chamber I, and 8×10^5 in Chamber II, III, IV. The units are $(0.2\ \mu\text{sec})^2$. These values correspond to an ambiguity of position of 1 cm.

The next criteria which were imposed on the acceptable events were the limits of pulse height in the target counter.

The pulse height had to be at least 0.05 MeV of energy loss, which was somewhat larger than single photoelectron noise. The pulse height had to be less than 0.54 MeV. This upper limit helped to eliminate events due to spurious beam particles passing through the target counter and a large fraction of the events in which an energetic secondary δ ray was produced. The upper cutoff was well within the limit of linearity in the pulse height analysis. The upper cutoff introduces a momentum dependent bias which is accounted for in Sec. VII.

After making a preliminary estimate of the useful regions of ϕ_T and α', the histograms of DZ3, DZ4, and DR4 were constructed for each 5 MeV/c band of momenta. In addition, the events in these histograms were within the same maximum limits on all other variables which were imposed when the final selection was made. Some of these histograms are shown in Figs. 28 and 29. The distributions are gaussian and their widths are not dependent on momentum, as can be seen from Fig. 30. The events in the tails of these distributions contain the positrons which scattered off obstructions or muons which after scattering in the target counter, were detected in the E counter.

The spatial extent of the scattering permitted by the limits depends on momentum, as has been discussed in Sec. VI-B. At 50 MeV/c the limits of acceptable DZ3 and DR4 correspond to a scattering of ± 2.5mm, and the limits for DZ4 correspond to a scattering of ± 5.0mm. Since the histograms for these variables are gaussian, the fraction of good events which were rejected can be estimated. Less than 0.1% of the good events were rejected by the DZ4 limits and hence no bias was introduced by these limits. Of the good events 1% were outside the limits of DR4. The momentum dependence of the fraction of these events was less than 10% and as a result a negligible bias was introduced by this selection. The momentum dependence of the widths of the DR4 distributions is shown in Fig. 30. The limits on DZ3 gave a 4% rejection of good events. The fraction of good events rejected by this criterion was not dependent on momentum, as the shape of the DZ3 distribution did not depend on momentum. The purpose of the limits on DZ3, DZ4, and DR4 was to eliminate events in which the positron scattered off an obstruction and lost some of its energy. A small contamination of events which did this remains and is discussed in Sec. VII-F. The pulse height criteria rejected 5% of the events, as did the scattering criteria.

The next selection chose events from a region of α' and ϕ_T, such that the momentum dependence of the spectrum did not depend on the choice of the region of α' and ϕ_T. The size of this region was determined from the data and is in agreement with the expected region. Histograms of α' were made for each 5.0 MeV/c interval of momentum, and each 11° interval of ϕ_T, and each cm of the target along the Z_T direction. The α' histograms are constant for a symmetric range of α' and fall to zero within a fraction of a degree. Plots of two such histograms which have been summed over Z_T are shown in Fig. 31. As can be seen from the histogram the minimum interval of α' over which the population is constant occurs at the maximum momentum. As the width of the interval varies inversely with the momentum, an unbiased selection of events is made when all the events which lie within the interval defined by the maximum momentum are chosen. The width of this interval is 11.5° and is symmetric at about zero.

After determining the maximum useful region of α', histograms of φ_T were constructed for events satisfying $|\alpha'| < 5.75^{\circ}$ and for each 5 MeV/c band of momenta. As with α' the maximum useful region of φ_T is that region of φ_T for which the histogram population is constant for all values of P. The region depends on the choice of the ratio of the minimum to maximum momentum of the final momentum selection. For a ratio of 0.65, the useful range of φ_T is $-19^{\circ} \leq \varphi_r \leq 18.5^{\circ}$. Figure 32 shows the φ_T histograms for each 5 MeV/c band of momenta for the 6.6 kG field case and the cutoff criteria. Unlike the α' histograms the distributions do not have a sharp cutoff, but have a gradual decrease for large φ_T. The histogram for the region 50.0 MeV/c to cutoff is not flat anywhere and changes by 6% over the useful region. The latter effect is caused by the variation of the magnetic field at large radii, together with the fact that this momentum band contains the endpoint. At $\varphi_T = 18.5^{\circ}$ and P = 50 MeV/c the momenta will be measured by 1/4% due to the field. As a result the element of population between 50 MeV/c and 50.08 MeV/c will be found in the band between 45 MeV/c and 50 MeV/c.

The band between 50.0 and 52.8 MeV/c will be depleted by that amount, which is 5%. The band between 45 and 50 MeV/c loses an amount almost equal to what it gains, so that to first order there is no net change in its population. This effect is taken care of later in Sec. VII by estimating its effect on ρ. It is of course surprising that such a large effect is present in the φ_T histograms when the momentum error is so small.

The small slope, less than 1%, at other momenta is due to vertical focussing. The effect also causes a systematic error and is corrected for later in Sec. VII.

The final momentum spectra which were selected by the foregoing are tabulated in Appendix IV for each field. Approximately 80% of the data are rejected because they fall outside of the limits on α' and ϕ_T.

VII. EXPERIMENTAL RESULTS AND DISCUSSION OF THE EXPERIMENTAL ERROR

A. The Internal Consistency of the Data and the Evaluation of ρ

Since each momenta spectrum obtained at a given value of magnetic field permits an independent measurement of ρ, each spectrum was compared separately to the theoretical spectrum. The theoretical spectrum is composed of two parts; the first part is the spectrum for the case $\rho = 3/4$ and $\eta = 0$, and the second part represents the difference between the spectrum for $\rho = 3/4 + \Delta\rho$ and $\eta \neq 0$. The inclusion of corrections is described in Sec. V. Data for the experimental spectra were selected according to Sec. VI-C. The comparison between experimental and theoretical spectra is made by computing χ_j^2, defined by Eq. (40).

$$\chi_j^2(\Delta\rho,\eta) = \sum_{P_i=P_{min}}^{P_{max}} \frac{[\alpha^j N_{th}(P_i) - N_{ex}^j(P_i)]^2}{N_{ex}^j(P_i)} \qquad (40)$$

j denotes the magnetic field the data were taken at. j = 6.6 kG, 5.3 kG, and so forth. $N_{ex}^j(P_i)$ are the number of events in the i^{th} momentum interval observed experimentally at the j^{th} field setting. $N_{th}(P_i)$ is the relative density of events in the i^{th} momentum interval for the theoretical spectrum and is chosen to satisfy Eq. (41).

$$\alpha_j \sum_{P_i} N_{th}(P_i) = \sum_{P_i} N_{ex}^j(P_i) \qquad (41)$$

For the particular hypothesis $\rho = 3/4$ and $\eta = 0$. χ^2 has been computed for each magnetic field and the results are shown in Table VIII. They show that with the exception of the data taken at 5.3 kG the agreement with the hypothesis is good and hence the data show consistency from one field to another.

TABLE VIII

Values of χ^2 for the Hypothesis ρ=0.750 and η=0.0

Momentum Region (MeV/c)	Magnetic Field (kG)	Degrees of Freedom	Chi Square
52.6-38.6	7.2	35	30
52.6-34.0	6.6	62	60
44.9-27.9	5.3	55	85
44.9-33.6	5.3	39	44
31.6-19.4	4.4	40	43
21.8-13.6	2.6	25	21

The data taken at 5.3 kG do not agree with the hypothesis and the disagreement can further be isolated to a part of 5.3 kG data. The disagreement will be discussed at length later in this section. In addition to computing χ^2 for the hypothesis $\rho = 3/4$ and $\eta = 0$, the most probable value of ρ was found by minimizing χ^2 with respect to $\Delta\rho$. The results of these calculations are presented in Table IX. The data from 2.0 kG were not statistically significant, as they were consistent with all values of ρ from +1 to 0.

TABLE IX

Most Likely Value of ρ When η=0 at Each Magnetic Field

Momentum Region (MeV/c)	Magnetic Field (kG)	Number of Events	Degrees of Freedom (deg)	Chi Square	$\rho \pm$ Statistical Error
52.6-38.6	7.2	11,799	35	30	0.7500±0.022
52.6-34.0	6.6	744,085	62	59	0.7510±0.0024
44.9-27.8	5.3	400,000	53	84	0.7384±0.0053
44.9-33.6	5.3	301,668	38	36	0.748 ±0.0082
31.60-19.4	4.4	85,304	40	43	0.746 ±0.022
21.80-13.65	2.6	13,777	25	21	0.750 ±0.167

The agreement of one field with another is good except for the 5.3 kG data.

Another means of testing agreement of the results obtained at different fields is to make a direct comparison of the spectra shapes where the spectra span a common interval of momenta. The fields were chosen in such a manner that the useful region of momenta at any given field would overlap the useful momenta region of momenta at the next larger and the next smaller field.

For example, at 6.6 kG and 5.3 kG the useful region of momenta for both fields contains the interval between 34.0 and 44.9 MeV/c. The extent of the useful region of momenta at any given field setting is based on criteria described in Sec. VI-D. Since no attempt was made to monitor the muon stopping rate in the target counter, the spectra first must be normalized so that each has an equal number of events in the overlap region. The normalization is done by Eq. (42):

$$\sum_{P_i} [C_j N_j(P_i) - C_{j-1} N_{j-1}(P_i)] = 0 \qquad (42)$$

C_j is the normalization constant for the j^{th} field. Equation(40) is defined to be 1. A χ^2 is computed for each pair of overlapping spectra by Eq. (43)

$$\chi^2_{j,j-1} = \sum_{P_i} \frac{[N^j_{ex}(P_i) - (C_{j-1}/D_j) N^{j-1}_{ex}(P_i)]^2}{N^j_{ex}(P_i) + (C_{j-1}/C_j)^2 N^{j-1}_{ex}(P_i)} \qquad (43)$$

The sum is carried out over the momenta interval common to each pair of spectra. A point-by-point comparison of one overlap region is shown in Fig. 33. The results of the overlap computations are presented in Table X.

TABLE X

Comparison of Overlap Regions

Overlap Region (MeV/c)	No. of Degrees of Freedom	No. of Events in Each Region		χ^2_j, j-1
44.9-34.0 (6.6 and 5.3 kG)	35	438,032	294,782	39.4 ± 8.5
31.6-27.8 (5.3 and 4.4 kG)	14	91,439	40,154	24.7 ± 5.6
21.8-19.4 (4.4 and 2.6 kG)	7	42,244	5,299	7.1 ± 3.7
15.4-13.6 (2.6 and 2.0 kG)	5	2,382	1,096	5.6 ± 3.2

The results show that agreement between the 5.3 kG and 4.4 kG field spectra is poor, and that all other overlaps show good agreement. The overlap between 4.4 and 2.6 kG and 2.6 and 2.0 kG are statistically weak and the results of Table VIII are more useful in establishing agreement since more events are being compared. The three tables can be combined to show that the data between 33.6 MeV/c and 27.8 MeV/c obtained when the field was 5.3 kG is in strong disagreement with all other data and any reasonable theoretical spectrum. The data of Table X show that either the 5.3 kG or the 4.4 kG data are in error. Table VIII shows that only the 5.3 kG data, and only the part between 33.6 and 27.8 MeV/c, reject the theoretical hypothesis $\rho = 3/4$ and $\eta = 0$. Table VIII also shows that all other data can fit the hypothesis $\rho = 3/4$ and $\eta = 0$. Table IX shows that all data except the questioned data fits a spectrum for some value of ρ very well.

The data for the 5.3 kG field fits no value of ρ well. The probability for all these results to be consistent is well beyond reasonable statistical limits. An examination of the difference between the best-fit theoretical spectrum and the experimental spectrum of 5.3 kG shows that there is no obvious systematic departure. There is only a wide scatter of points. In particular, the contribution to χ^2 in the interval 27.8 to 33.6 MeV/c for the hypothesis $\rho = 3/4$ was 48 for 19 degrees of freedom. The contribution to χ^2 for the remainder of the data at this field setting, data from 33.6 to 44.9 MeV/c, was 38 for 36 degrees of freedom. Because the data taken at

4.4 kG include part of the same momenta band as the data in question, there is an independent check that the anomaly is due to a malfunction of the apparatus and not due to some undiscovered property of muon decay. For the foregoing reasons the data between 27.8 and 33.6 MeV/c taken at the 5.3 kG field was not used in any of the subsequent analyses. If the data were included the value of ρ obtained would only decrease by 0.002, but the fit would be very poor.

Because the ϕ_T distributions were not flat a check of whether the spectra were the same was made by comparing the 6.6 kG data taken for $-19^o < \phi_T < 0$ with the 6.6 kG data taken for $0 < \phi_T < 18.5^o$. Except for the momentum intervals which include the endpoint, the agreement was within statistics. Each piece of the data measures ρ to $\pm$ 0.004. An effect is expected at the endpoint and was observed as expected. The small difference between the two spectra caused by vertical focussing was not observed because of statistics. At the other fields the quantity of data was smaller and did not permit meaningful comparisons. The conclusion which can be drawn from these checks is that the data is self-consistent except as noted earlier.

Using only the data which are self-consistent the most probable value of ρ was computed by minimizing the sum of the χ_j^2, (defined by Eq. (40)). The sum is carried out over all the field settings with the value of ρ:

$$\rho = 0.7498 \pm 0.0022 \quad \text{when } \eta = 0 .$$

The error is the statistical error and corresponds to the values of ρ where χ^2 has increased by 1 from its minimum value. The value of χ^2 was 188 for 213 degrees of freedom. A plot of χ^2 as a function of ρ is shown in Fig. 34.

In addition to the case $\eta = 0$ and ρ variable, the case $\rho = 3/4$ and η variable was investigated. When $\rho = 3/4$ the most probable value of η is

$$\eta = 0.05 \pm 0.050 \qquad \text{when } \rho = 3/4 \quad .$$

The preceding values for ρ and η have not been corrected for several small systematic errors which were present in the experiment.

B. Experimental Check of Ionization Loss and Bremsstrahlung

Since the largest corrections made to the data were those due to bremsstrahlung and ionization loss, part of the experiment was devoted to checking these corrections. Most of the bremsstrahlung is generated in the 1/8-in. plastic scintillator which is used as the target. By placing a 3/8-in. thick piece of the same type of plastic scintillator between the first chamber and the target counter, the positrons which emerged from the target counter were degraded in energy by additional bremsstrahlung and ionization loss. The 3/8-in. plastic scintillator served no purpose other than to degrade the positron energy, and all detected positron trajectories began in the 1/8-in. target counter. The bremsstrahlung was increased by a factor of 7 and the ionization loss outside of the target by a factor of 20 beyond the normal experimental conditions. Of the 600,000 events of this kind recorded, 120,000 of these were in the useful regions of momentum and solid angle. Two relevant numbers were obtained from the data: the shift in the endpoint, which measured the most probable ionization loss; and a value of ρ, which gives a measure of how well the corrections were made in the momentum interval between 34 MeV/c and 52.8 MeV/c.

The shift in the endpoint was 1.65 MeV/c and is to be compared with the 1.68 MeV/c predicted by the following formula[30]

$$\Delta_p = (0.1537)\left(\frac{\Sigma_Z}{\Sigma_A}\right) D[19.43 + \ln(D/P)] \tag{44}$$

Δ_p is the most probable energy loss in Landau's probability distribution for ionization loss. The shift in the endpoint should correspond closely to the most probable energy loss. The endpoint was defined to be the momentum at which the population of the experimental spectrum had fallen to half the population at 50.0 MeV/c. Experimental results agree with both Δ_p and the shape of the Landau distribution for energies below 15 MeV. Above that energy there are no experiments. In particular the results of Goldwasser, Hanson, and Mills at 15 MeV/c agree with the Landau theory to within a few percent.[30] The value of ρ obtained from this data provides a more direct check of the corrections. If bremsstrahlung had been ignored for the data taken under normal experimental conditions the value of ρ obtained would be 0.005 lower than the correct value. When the 3/8-in. plastic scintillator is added, the value of ρ would be decreased by an additional 0.032 if bremsstrahlung were ignored. The effect of straggling in the ionization loss is to lower ρ by 0.03 if it is ignored when the 3/8-in. plastic is added.

On the basis of including all the corrections for the extra plastic in addition to those normally made, the value of ρ obtained from this data was $\rho = 0.748 \pm 0.008$, which is in excellent agreement with the other data. Since the effects which are corrected for are eight times the statistical error, one can conclude that the corrections for the case without the extra scintillator were correct to at least 0.001 in ρ.

C. An Upper Limit to the Muon Neutrino Mass

Another experimental result which can be obtained from this experiment is an upper limit to the muon neutrino mass. Ignoring radiative corrections a displacement of the endpoint from a value less than [31]

$$P_e = \frac{M_\mu C}{2}\left(1- \left(\frac{M_e}{M_\mu}\right)^2\right) = 52.826 \text{ MeV/c} \tag{45}$$

is a sign that the muon neutrino mass is not zero. If ΔP is the discripancy in the endpoint, then

$$M_\nu^{\,2} \approx 4c^2(\Delta p)(k_\nu) \tag{46}$$

where k_ν is the momentum of the muon neutrino. After averaging over all values of k_ν, the upper limit on M_ν can be put as:

$$M_\nu^{\,2} < \Delta c^2(\Delta p)(\bar{k}_\nu) \approx c^2(\Delta p)M_\mu \tag{47}$$

$\bar{k}_\nu$ is the average muon neutrino momentum when emitted collinear with the electron neutrino and the electron. The shape of the endpoint can in principle give more information, but it is uncertain by the uncertainty in the experimental momentum resolution. The preceding discussion is based on the assumption

in the falloff and the statistical fluctuations in the that the electron neutrino mass is zero. This mass is known to be less than 200 eV and thus the assumption is reasonable.[32]

Aside from the pulse height correction which has been discussed previously, only two corrections must be made to the spectrum at the endpoint to obtain the endpoint. The experimental endpoint must be corrected for energy loss by ionization in the wrapping of the target counter, spark chamber I, and the vacuum tank. The loss, 0.12 MeV/c, was computed from Eq. (44) and the contribution of each piece of material to the loss is given in Table XI.

TABLE XI

Sources of Ionization Loss
Which Were Not Accounted for in Reconstruction

Material		D ($grx10^3/cm^2$)	t (cm)	Δp (MeV/c)
Mylar				0.077
Vacuum Windows	0.010-in.	34.9	0.0252	
Two Spark Chamber Windows	0.003-in.	21.2	0.0154	
Inside Counter Wrapping (Aluminized Mylar)	0.001-in.	3.6	0.0026	
Two Aluminum Foil Electrodes	0.001-in.	13.7	0.0051	0.014
1 Layer of Black Polyethylene		8.0	0.008	0.010
4 cm Air		5.3	4.0	0.008
4 cm Neon		3.5	4.0	0.006
Total Energy Loss				0.115

The true endpoint is not an observable property of the spectrum, due to the presence of the corrections outlined in Sec. V-B and Sec. V-C. The endpoint is defined operationally as that momentum at which the spectrum has half the population that the spectrum has at 51.5 MeV/c. This definition clearly depends on 51.5 MeV/c as a reference and the use of a halfway point. The shift of the operational endpoint relative to the true endpoint is obtained by applying the operational definition to the theoretical spectrum. The shift was found to be 0.06 MeV/c. The total correction due to the preceding two effects is 0.18 MeV/c.

The momentum resolution of the spectrometer was determined to be ± 0.16 MeV/c at 52.8 MeV/c, from the width of the falloff. The endpoint was determined at three different fields, the results of which are presented in Table XII.

TABLE XII

Experimental Determination of Muon Spectrum Endpoint

Magnetic Field (kG)	Experimental Endpoint (MeV/c)	Corrected Endpoint (MeV/c)
6.6	52.66 ± 0.02	52.84 ± 0.02
7.2	52.68 ± 0.04	52.86 ± 0.04
7.7	52.66 ± 0.04	52.84 ± 0.04
Average of All Fields ± Variance	52.66 ± 0.02	52.84 ± 0.02

The uncertainty in the endpoint at the 6.6 kG field is due entirely to the uncertainty in the magnetic field. At 7.2 and 7.7 kG there are an order of magnitude fewer events in the falloff and the statistical fluctuations in the populations account for the increased uncertainty in the endpoint. These results differ by several hundredths of 1 MeV/c from previously published values.[33] The difference arises from the fact that the trajectory was not corrected during reconstruction for energy loss near Chamber II and the effect of the magnetic field variations was neglected in the earlier publication. On this basis the mass of the neutrino is $m_\nu < 1.5$ MeV with 90% confidence. The experimental variance is consistent with the estimated error in chamber location and the average magnetic field.

D. Errors in ρ Due to Systematic MisMeasurement of Momentum

The systematic errors of the experiment can be grouped into three main categories:

1. A systematic mismeasurement of momentum,
2. The selection of events in the spectrum with a momentum-dependent bias,
3. Inclusion in the spectrum of electrons which have scattered off obstructions, or particles which did not come from the decay of a muon.

These errors are inherent to all counter experiments as was mentioned in Sec. II. However, because of the use of spark chambers it is possible to reduce the systematic errors by two orders of magnitude in most instances.

A momentum mismeasurement can arise from one of the following: Incorrect measurement of the relative position of the spark chambers, systematic error in sound ranging, and inaccurate knowledge of the magnetic field. In all instances the accuracy of these measurements exceeds the damands of the experiment. The relative position of the chambers is known to 0.005 in., and hence the error on momentum is 1 part in 5000. The systematic errors of the sound ranging do not exceed 0.005 in., on the basis of the measurements discussed in Sec. IV. The effect on ρ due to positron measurements does not exceed 0.0001.

The magnetic field was measured with an NMR, and the accuracy of this device exceeds 1 part in 10^4. The fact that the field was not completely uniform, together with the approximation of a constant field, can introduce two types of error. The first is an error in the endpoint, and the second is a non-linear momentum scale. The field between Chamber I and II for 34 MeV/c was on the average 1 part in 2000 lower than the field for the 52 MeV/c trajectories. The variation of the average field is more sensitive to the angle ϕ_T and it is this dependence which causes the appearance of the ϕ_T histograms in Fig. 30. The stretching of the momentum scale causes the measured value of ρ to be low by 0.0007±0.0003. The error in the estimate is due to the uncertainty in the magnetic field. The value of ρ is sensitive to the exact location of the end-point even when the falloff is not included. If the spectrum is constrained to have its endpoint at the value predicted by Eq. (45), then the value of ρ given in Sec. VII-A must be corrected by subtracting 0.0009± 0.0005, since the end-point is 1 part in 3000 beyond the value predicted by Eq. (45).

As evidence that the endpoint measurement was made correctly and independent of the location of the trajectory, the consistency of the endpoint measurements is presented in Table XIII.

TABLE XIII

Positron Spectrum Endpoint in Different Parts of the Spectrometer

Azimuthal Angle at the Target	Endpoint Before Field Correction	Endpoint After Field Correction
(deg)	(MeV/c)	(MeV/c)
-10 ± 5	52.69 ± 0.02	52.68 ± 0.02
0 ± 5	52.66 ± 0.02	52.67 ± 0.02
+10 ± 5	52.62 ± 0.02	52.66 ± 0.02
+20 ± 5	52.56 ± 0.02	52.64 ± 0.02

E. Systematic Errors in ρ Due to Momentum Dependent Selection Criteria

Several of the selection criteria introduced momentum biases in the spectrum. In addition the electronic logic which fired the spark chambers caused a small momentum bias. The sources of the biases are listed as follows:

1. Multiple scattering selection criteria,
2. Momentum-dependent choice of solid angle,
3. Event trigger,
4. Pulse-height selection criterion.

The existence of momentum-dependent selection criteria has been mentioned before in connection with the limits set for multiple scattering. The selection was made as momentum-independent as possible by factoring out the momentum dependence of the multiple scattering. As the multiple scattering is not exactly gaussian and since the results are somewhat sensitive to the exact limits which are set, a systematic error is introduced. The error is estimated to be less than $\pm$ 0.001 in ρ.

A more important cause of a momentum-dependent selection criterion is due to the non-uniform magnetic field. The non-uniform field implies the presence of a radial field which causes vertical focussing. The angle α is no longer correctly computed from the relation:

$$\alpha = \frac{Z_{II} - Z_{I}}{R\ \varphi_{12}} \tag{48}$$

φ_{12} is the arc subtended by the trajectory between Chamber I and II. The effect of the radial field is to displace Z_{II} from the value a simple helical trajectory would have given. If this displacement depends on momentum, the actual interval of α which was chosen also depends on momentum. The following analysis shows how this dependence comes about.

Near the median plane the radial field is $\left(\frac{\partial B_z}{\partial R}\right) Z$ and it follows that the displacement of Z_{II} from the value obtained from a simple helical trajectory is given by

$$\Delta Z = (\varphi_{12})^2 R \left\langle \frac{1}{B_o} \frac{\partial B_z}{\partial R} Z \right\rangle \tag{49}$$

After averaging ΔZ over all azimuthal angles and target positions the relation between the true value of α, α_T, and the measured value α_m, can be written as:

$$\alpha_M = \alpha_T \left(1+ \frac{\pi^2 R}{6B_o} \left\langle \frac{\partial B_z}{\partial R} \right\rangle \right) \quad (50)$$

The average value of $\frac{1}{B_o}(\partial B_z/\partial R)$ over these angles and target positions is 5×10^{-5}/cm. As it causes the measured value of $|\alpha|$ to be greater than the true value and since the difference is larger for larger momenta the choice of α intervals is momentum-dependent. Substituting the relevant number into Eq. (50) the relation between α_M and α_T is

$$\alpha_M = \alpha_T(1+0.002x) \quad (51)$$

Using the selection criterion outlined in Sec. VI-C the range of α' was 0.2% smaller at 52.8 MeV/c than it was thought to be, and the range of α' was 0.1% smaller at 34 MeV/c than it was thought to be. The effect is to introduce a bias which favors the low momentum by 0.1%. By using the selection criteria of Sec. VI-C the value of ρ given in Sec. VII-A is low by 0.0012 ± 0.0005 due to the effect of vertical focussing. As mentioned in Sec. VI-C the φ_T histograms are distorted by vertical focussing. One may average Eq. (49) over all momenta and target positions and demonstrate the presence of this effect. The non-uniform field also causes the angle φ to be mismeasured. However, the effects on ρ are negligible in comparison to the preceding case for α.

The principal cause of the momentum bias in the event trigger was positron annihilation in flight. All events for which annihilation took place in the target counter, the spectrometer, or the E1 counter were excluded from the experimental spectrum. Since the fraction of positrons which annihilate varies inversely with the energy, the momentum dependence of the experimental spectrum differs from the positron spectrum at the instant of decay. The fraction of annihilations which were excluded can be estimated from the annihilation cross section $\phi(E)$ into two photons. If E is the positron energy then the probability that the positron will annihilate in flight with an electron into two photons is[34]

$$\phi(E) = \pi r_o^2 \left(\frac{M_e}{E}\right)\left(\log \left(\frac{ZE}{m_e}\right) - 1\right) \qquad E \gg M_e \tag{52}$$

Single photon annihilation is a factor of $(\alpha^2 Z)^4$ smaller and since Z = 6 for carbon, the contribution is negligible.[35] Annihilations in the target counter, E1 counter, the first 1/6 of the E2 counter, and the spectrometer introduced a bias. The total amount of material is 1.23 gm/cm^2 and the fraction of excluded events is

$$f(x) = \frac{0.0044}{x}\,[1 + 0.023\ \ln x] \tag{53}$$

This bias caused the measured value of ρ to be high by 0.0026±0.0005. The uncertainty is due to the uncertainty in the fraction of E2 which must be traversed before a count is registered in E2.

Another possible source of bias was positron dependence of the spark chamber efficiency. By examining the class of events which missed a single chamber it was possible to determine where the spark would have been from the trajectory determined by the other three chambers. By demanding that the missing spark correspond to a point within the chamber fiducial volume the chamber efficiencies were found to be within 0.1% to 0.4%. The missing spark did have an unusual distribution as the misses tended to cluster at the edges of the chamber. This can be accounted for in part by the fact that a positron can scatter off the steel frame in the inactive region and into the remaining chambers. The reconstructed event will tend to have distribution which extends into the active region. The misses which were not associated with the edges, approximately one-half of the misses, are associated with low momentum trajectories which scatter very badly. The interpretation of these events is that they are muons. There is no evidence that there is a systematic inefficiency in the spark chambers and this systematic error is put at less than 0.001 in ρ.

The double spark criterion in Chamber I together with the pulse height criterion of 0.54 MeV placed a limit on the maximum kinetic energy of the secondary electrons produced by Bhabba scattering.[36] The limit was estimated to be 0.27 MeV. The rejection of all events with secondary electrons of kinetic energy greater than 0.27 MeV introduced a momentum bias since high momentum positrons were more likely to produce energetic secondaries than were low momentum positrons. If ΔE is the cutoff kinetic energy, the probability that a positron of energy E produced a secondary with energy greater than $\Delta E + M_e$.

$$\phi(E) = 2\pi r_o^2 \left[\frac{M_e}{\Delta E+M_e} - \frac{M_e}{E} \left(2\ln\left(\frac{E}{\Delta E+M_e}\right) - \frac{4}{3} + \frac{3(\Delta E+M_e)}{E} \right) \right] \quad (54)$$

The expression was derived from the Bhabba scattering cross section and terms of order $(\Delta E+M_e)^2/E$ have been dropped. In addition to Bhabba scattering in the target, events which scattered in the spectrometer between Chamber I and IV would be rejected for ΔE in excess of a few MeV, as a result of the multiple scattering criteria and double sparks. Taking these contributions together, their effect was to reduce the measured value of ρ by 0.0021 ± 0.0005.

F. Systematic Errors Due to Contamination of the Spectrum by Unwanted Events

There are three types of unwanted events which could have introduced a bias if they had been sufficiently numerous:

1) Positrons from muon decays in the anti-counter,
2) Beam muons which scattered into the apparatus,
3) Positrons which scattered off the vacuum tank walls or other obstructions in the apparatus.

All other types of events, whether caused by a real or accidental trigger, either did not give a reconstructable event or gave an event which did not bias the spectrum. The first category gave a bias because of the undetermined energy loss in the anti-counter. The anti was estimated to be 100% efficient for energy losses in excess of 0.2 MeV. There were two sources of positrons which came from the anti. The beam pion could scatter in the target and into the anti; a subsequent event trigger would have been generated if the positron decay were undetected by the anti, and simultaneously was in accidental coincidence with the muon gate (1%). During the experiment the rate of positrons which came from pions stopped in the anti was found to be one-fifteenth of the normal rate. The anti-efficiency for the positron decays was found to be 95%; as a consequence the probability of a positron coming from the anti in this manner is less than one on ten thousand. The second source of muons stopping in the anti were from pions which stopped in the side of the target counter which faced the anti. Of all the stopped pions 10% produced muons which escaped from this face of the target counter, and of these approximately 10% stopped in a region of the anti-counter resulting in trajectories which would satisfy the selection criteria of Sec. VI. The timing of the anti-counter was arranged so that these events would not give triggers, and it is estimated that 90% of these muons had enough range in the anti to be rejected. The relative rate is less than 1 in 1000 of the good event rate. Since the energy loss of the positron could not have exceeded 0.2 MeV without being detected by the anti, the bias introduced by these events is negligible.

The second type of unwanted events arose from muons in the pion beam which scattered in the target, and subsequently went through all spark chambers and stopped in either E1 or E2 counters. Most of these events did not have enough range to reach E2. The delay of the muon gate, 0.5 μsec, prevented these prompt events from triggering the spark chambers. A muon which stopped in E1 generated a muon gate and the efficiency of E1 and E2 for counting the subsequent decay positron was almost 50%. The accidental coincidence rate between T^- and the coincidence of E1 and E2 was measured to be 5%. The spark chambers were fired by this accidental coincidence and because the chambers were sensitive for 5 μsec, there was a reasonable chance that the muon track would give sparks in all chambers. The event would have reconstructed with a momentum between 35 and 60 MeV/c. These muons must lose a significant fraction of their energy as they traverse the spectrometer. The average value of DR4ACT for a 40 MeV/c muon is +10 mm. Since the scattering limits of the DR4 criterion are ± 3 mm at 40 MeV, 95% of the muons were rejected by this criterion. Since the multiple scattering of 40 MeV/c muons is three times that of 40 MeV/c positrons, the DZ4 and DZ3 scattering criteria rejected an additional factor of three of these events. If all of the accidentals were assumed to be due to beam muons (5%), then the fraction of contamination cannot exceed 1 part in 1,200. The effect is therefore negligible.

The third type of unwanted events were the positrons which scattered off the vacuum tank walls and reconstructed as a lower energy positron. These events triggered the apparatus although their presence in the spectrum is unlikely since the DR4, DZ3, and DZ4 selection criteria eliminated them. An estimate of the fraction of the events that were scatterings can be made by noting that events which scattered off obstructions must have very broad distributions of DZ3 and DR4, and appear as a flat background in the DZ3 and DR4 histograms. It is estimated, when applying only the DZ3 criterion (or the DR4 criterion) and permitting the other scattering limits to be the maximum (± 2 cm at 50 MeV/c), that 0.3% are the events due to scattered positrons. Since DZ3 and DR4 are independent criteria the total number of positron events which had these scatterings is less than 0.1%. This is an overestimate since there should be a tail due to coulomb-scattering and the tails of the DZ3 and DR4 histograms could be attributed to this. The effect is considered to be negligible.

G. Experimental Value of ρ

The results of the preceding analysis, together with the best estimate of the value of ρ, lead to a corrected estimate of $\rho = 0.7503 \pm 0.0026$. The systematic corrections are summarized in Table XIV.

TABLE XIV

Summary of Experimental Systematic Corrections to ρ

Source of Systematic Correction	Best Estimate Of Correction	Uncertainty In Correction
Stretching of Momentum Scale	+0.0007	±0.0003
Uncertainty of the Endpoint	-0.0009	±0.0005
Vertical Focussing	+0.0012	+0.0005
Positron Annihilation	-0.0026	±0.0005
Bhabba Scattering	+0.0021	±0.0005
Spark Chamber Efficiency	---	±0.0010
Contamination by Unwanted Events	---	0.000
Sum of Corrections	+0.0005	±0.0014
Best Estimate of ρ Before Correction	+0.7498	±0.0022
Experiment Value of ρ Including Corrections	0.7503	±0.0026

The data are sufficiently insensitive to η that the systematic corrections are not necessary to the best fit value of η where $\rho = 3/4$. This result is

$$\eta = 0.05 \pm 0.50 \qquad \text{when } \rho = 3/4 .$$

VIII. INTERPRETATION OF THE EXPERIMENTAL RESULTS

The results of this experiment can only be interpreted after a definite order for the lepton fields in the interaction hamiltonian have been chosen. The order of the lepton fields cannot be established from the interaction of the leptons alone, since the order can be changed by a Fierz transformation on the hamiltonian without changing the measurable quantities. A discussion of this ambiguity is given in Appendix I. Since muon decay is an example of a weak interaction, the natural ordering to choose is the ordering that follows from charged lepton currents. The fact that neutral lepton currents have never been observed, makes it plausible that the charge retention order, an interaction of neutral currents, is incorrect. Unfortunately, almost all theoretical work that has been done on muon decay has used the charge retention order.

Even after the choice of an order has been made the range of possible interpretations is still too large to handle. One more reasonable restriction that can be placed on the hamiltonian is to set the scalar coupling constant, G_S, to zero. The experiments which permit this choice are discussed in Appendix I. After imposing the preceding two assumptions the experimentally measurable parameters, ρ, δ, ξ, and η, are functions of only four quantities. The most convenient way to express these quantities is to express them in terms of the fundamental couplings G_V and G_T and the extent to which the neutrinos violate lepton conservation in the hamiltonian. The hamiltonian contains Majorana neutrinos and only the dynamics restrict the possible helicities of the neutrinos. The hamiltonian density on which the interpretation of the experiment is based is given in Eq. (55).

$$H_I(x) = \sqrt{8}\, G_V \tilde{\mu}\gamma_\alpha \left(\frac{(1+i\gamma_5)}{2} + \alpha_\mu^V \frac{(1-i\gamma_5)}{2}\right) \nu_\mu \tilde{\nu}_e \left(\frac{(1-i\gamma_5)}{2} + \alpha_e^V \frac{(1+i\gamma_5)}{2}\right)\gamma_\alpha e$$

$$+ \sqrt{8}\, G_T \tilde{\mu}\sigma_{\alpha\beta} \left(\frac{(1+i\gamma_5)}{2} + \alpha_\mu^T \frac{(1-i\gamma_5)}{2}\right) \nu_\mu \tilde{\nu}_e \left(\frac{(1-i\gamma_5)}{2} + \alpha_e^T \frac{(1+i\gamma_5)}{2}\right)\sigma_{\alpha\beta} e \qquad (55)$$

$\frac{(1+i\gamma_5)}{2}$ and $\frac{(1-i\gamma_5)}{2}$ are the helicity projection operators. Since it is known already that the fraction of the righthanded neutrino which participates in weak interactions is small, the α's which describe this amount are less than one. The connection between this hamiltonian (Eq.(55)), and one described by Eq.(5) is given in Appendix I. Because the α's and G_T/G_V are known to be small, approximate expressions for ρ, δ, ξ, and η can be derived which permit easy interpretation of the measurements. Equations (56) to (59) are derived in Appendix I.

$$\rho = \frac{3}{4}\left(1-(\alpha_\mu^V)^2 - (\alpha_e^V)^2 - \frac{17}{4}\left(\frac{G_T}{G_V}\alpha_e^T\right)^2 - \frac{17}{4}\left(\frac{G_T}{G_V}\alpha_\mu^T\right)^2\right) \qquad (56)$$

$$\delta = \frac{3}{4}\left(1-3(\alpha_\mu^V)^2 - 3(\alpha_e^V)^2 - \frac{43}{4}\left(\frac{G_T}{G_V}\alpha_e^T\right)^2 + \frac{51}{4}\left(\frac{G_T}{G_V}\alpha_\mu^T\right)^2\right) \qquad (57)$$

$$\xi = -1\left(1+2(\alpha_\mu^V)^2 - 4(\alpha_e^V)^2 - \frac{68}{4}\left(\frac{G_T}{G_V}\alpha_e^T\right)^2 + \frac{26}{4}\left(\frac{G_T}{G_V}\alpha_\mu^T\right)^2\right) \qquad (58)$$

$$\eta = \frac{6}{\sqrt{2}}\left\{\left(\frac{G_T}{G_V}\alpha_\mu^T\right)(\alpha_\mu^V) + \left(\frac{G_T}{G_V}\alpha_e^T\right)(\alpha_e^V)\right\} \qquad (59)$$

As the formulas have been written it is clear that η is not independent of ρ, δ, ξ. Moreover, $(\alpha_e^V)^2$ is known to be zero to < 1% from the helicity measurements in β decay. $(\frac{G_T \alpha_e^T}{G_V})^2$ is similarly restricted to less than 1%. Using these values and the best experimental values for δ and ξ, the following limits may be imposed

$|\alpha_\mu^V| < 0.2$ for simultaneous one standard deviation limit of both δ and ξ

$|\frac{G_T}{G_V} \alpha_\mu^T| < 0.02$ for simultaneous one standard deviation limit of both δ and ξ .

These limits in turn restrict η to

$|\eta| < 0.04$.

As can be seen from this discussion the least established feature of muon decay is the helicity of the muon neutrino. The possibility that the muon neutrino can permit a small amount of lepton non-conserving processes was pointed out by Friedberg.[38] The results of this experiment considerably diminish this possibility as will be shown.

The results of the measurement of the spectrum can be presented in either of two ways

$\rho = 0.750 \pm 0.003$ for $|\eta| < 0.04$

$\eta = 0.05 \pm 0.50$ for $\rho = 0.750$.

A simultaneous fit for ρ and η is uninformative, as the errors on ρ become quite large. Fitting for η alone is likewise uninformative since it only poorly confirms the limits imposed on η by existing measurements of ξ, δ, and ρ. This arises from the fact that the spectrum is very insensitive to η. The only new information that is gained from this experiment is the value of ρ for $|\eta|$ restricted to the values consistent with the measured values of ξ and δ. It follows from Eq. (56) alone that α_{μ}^{V} must be less than

$$|\alpha_{\mu}^{V}| < 0.06 .$$

A majorana neutrino which satisfies lepton conservation must be $\alpha_{\mu}^{V} = 0$. If this majorana neutrino is to give results identical to those of a two-component neutrino theory, the neutrino mass must be zero. The results of this experiment can be expressed in terms of the upper limits to α_{μ}^{V} and $M_{\nu_{\mu}}$:

$|\alpha_{\mu}^{V}| < 0.06$ (lepton non-conserving amplitude of the muon neutrino)

$M_{\nu_{\mu}} < 1.5$ MeV (upper limit to the muon neutrino mass).

These results provide improved evidence that the muon neutrino is a two-component neutrino.

Another interpretation of the measured value of ρ can be used to establish a lower limit on the intermediate boson mass. Although this experiment does not establish a better lower limit, it does deserve to be mentioned. The high energy neutrino experiments established a lower limit on the mass between 1.2 BeV and 2.2 BeV, depending on the branching ratio of W decays into pions and W decays into leptons.[24] The Columbia p-p collision experiment established an upper limit on the product of the W production cross section and the branching ratio of W into muons. This limit could be interpreted to establish an upper limit on the boson mass between 2.5 BeV and 6.0 BeV.[25]

This interpretation is sensitive to both production mechanism and the branching ratio. The 1.2 BeV limit established by the measurement of ρ does not depend on the branching ratio and is thus free from the aforementioned problems. The result may be sensitive to a detailed theory of higher orders of weak interactions.

A third conclusion that may be drawn from these results is that radiative corrections are properly calculated in the region $\chi = 0.50$ to 1.00. Between $\chi = 0.95$ and 1.00 the radiative corrections are large as they vary from 5 to 10%, while the population in the spectrum is 10^5 events/MeV/c. Since the agreement is within statistics, the check is good to about 5%. The check over the whole spectrum is somewhat better since the corrections amount to 5% in ρ between $0.3 < x < 0.95$ and the results are in agreement with the theory to 1/3%.

The experimental results are clearly in agreement with the V-A theory as outlined in the Introduction and Appendix I. The experiment is in good agreement with the bubble chamber experiments of Ref. 20f and 20g. The results are in good agreement with a recent experiment done by Sherwood and Telegdi which used wire chambers.[39] Their result was

$$\rho = 0.762 \pm 0.012 \qquad \text{for } \eta = 0.$$

IX. ACKNOWLEDGEMENTS

I would like to thank Professor Allan M. Sachs for his guidance and interest throughout the course of this work. I am very grateful to him for his active participation at every stage of the experiment. I am deeply indebted to my colleagues on the experiment, Dr. Marcel Bardon, Dr. Juliet Lee-Franzini, and Mr. Peter Norton, for their many contributions. I would particularly like to thank Peter Norton for his singular computer programs which made it possible to analyze the enormous amount of data in a fast and systematic way.

I thank Mr. Fredrich Sippach, who developed the electronics to handle the sonic spark chamber and 1401 computer, and Mr. Graydon Doremus for the careful and precise machining of the spark chambers.

I thank Mr. J. Cleary and Mrs. A. McDowell for the careful preparation of the many drawings and photographs. I am especially grateful to Miss Ann Therrien and Mrs. Edna Thornton for the typing of the manuscript and for shepherding it over its many hurdles.

APPENDIX I

Summary of the Experimental Limitations On The Muon Decay Hamiltonian

The fact that the measurable properties of muon decay cannot by themselves specify the muon decay hamiltonian has been stated in the introduction. The ambiguities which exist make it impossible to make a precise interpretation of this experiment unless a few additional restrictions are imposed on the hamiltonian. There are two assumptions that can be made, seemingly self-evident, to help restrict the possible interpretations of the experiment. A reasonable first assumption is to treat muon decay as a weak interaction, since one of the reasons for studying muon decay is to measure the bare weak interaction coupling constants. The second assumption made is that the weak interaction hamiltonian in the limit of low momentum transfer is properly represented by a current-current interaction. A consequence of these two assumptions is that the properties of the lepton currents can be established by decay processes other than muon decay.

The purpose of the following analysis is to make plausible restrictions on the muon decay hamiltonian and then finally to set a limit on η. The starting point for the computation of η is a phenomenological hamiltonian of the form:

$$\begin{aligned} H_I(x) = {} & G_S\tilde{\mu}(1+a_\mu^S i\gamma_5)\nu_\mu\tilde{\nu}_e(1-a_e^S i\gamma_5)e \; + \\ & G_V\tilde{\mu}\gamma_\alpha(1+a_\mu^V i\gamma_5)\nu_\mu\tilde{\nu}_e(1-a_e^V i\gamma_5)\gamma_\alpha e \qquad \text{(AI-1)} \\ & G_T\tilde{\mu}\sigma_{\alpha\beta}(1+a_\mu^T i\gamma_5)\nu_\mu\tilde{\nu}_e(1-a_e^T i\gamma_5)\sigma_{\alpha\beta} e \end{aligned}$$

In order to use the formulae for ρ, η, ξ, and δ which appear in the literature it is necessary to reorder the fermion fields in (AI-1) to the order in Eq.(AI-2).

$$H_I(x) = \sum_{\ell=1}^{5} g_i \tilde{\mu}\Gamma_i e \tilde{\nu}_e \Gamma_i \nu_\mu - g_i^1 \tilde{\mu}\Gamma_i e \tilde{\nu}_e \Gamma_i i\gamma_5 \nu_\mu$$

$$\Gamma_1 = 1 \qquad \Gamma_2 = \gamma_\alpha \qquad \Gamma_3 = \frac{i}{2\sqrt{2}} [\gamma_\alpha, \gamma_\beta] \qquad \Gamma_4 = i\gamma_\alpha\gamma_5 \qquad \Gamma_5 = -i\gamma_5$$

Equations (AI-1) and (AI-2) are connected by a Fierz transformation which relates the G_S, G_V, G_T, a_μ^S, etc. to the g_i and g_i^1.

These hamiltonians, which are equivalent, are the most general which are consistent with a point interaction without derivative coupling. The relationship between Eqs. (AI-1) and (AI-2) is given by the following ten equations.

$$g_1 = G_V(1-a_e^V a_\mu^V) + \frac{3G_T}{\sqrt{2}}(1-a_T^e a_T^\mu) + \frac{G_S}{4}(1-a_e^S a_\mu^S) \qquad \text{(AI-3)}$$

$$g_2 = -\frac{G_V}{2}(1+a_\mu^V a_e^V) + \frac{G_S}{4}(1+a_e^S a_\mu^S) \qquad \text{(AI-4)}$$

$$g_3 = \frac{G_T}{2}(1-a_e^T a_\mu^T) + \frac{\sqrt{2}}{8} G_S(1-a_e^S a_\mu^S) \qquad \text{(AI-5)}$$

$$g_4 = -\frac{G_V}{2}(1+a_\mu^V a_e^V) - \frac{G_s}{4}(1+a_e^S a_\mu^S) \qquad \text{(AI-6)}$$

$$g_5 = -G_V(1-a_\mu^V a_e^V) + \frac{3G_T}{\sqrt{2}}(1-a_e^T a_e^T) + \frac{G_S}{4}(1-a_e^S a_\mu^S) \qquad \text{(AI-7)}$$

$$g_1' = \left\{ G_V(a_\mu^V - a_e^V) + \frac{3G_T}{\sqrt{2}} (a_\mu^T - a_e^T) + \frac{G_S}{4} (a_\mu^S - a_e^S) \right\} \tag{AI-8}$$

$$g_2' = \left\{ - \frac{G_V}{2}(a_\mu^V - a_e^V) + \frac{G_S}{4} (a_\mu^S + a_e^S) \right\} \tag{AI-9}$$

$$g_3' = \left\{ - \frac{G_T}{2}(a_\mu^T - a_e^T) + \frac{G_S\sqrt{2}}{8}(a_\mu^S - a_e^S) \right\} \tag{AI-10}$$

$$g_4' = \left\{ - \frac{G_V}{2}(a_\mu^V + a_e^V) - \frac{G_S}{4}(a_\mu^S + a_e^S) \right\} \tag{AI-11}$$

$$g_5' = \left\{ - G_V(a_\mu^V - a_e^V) + \frac{3G_T}{\sqrt{2}} (a_\mu^T - a_e^T) + \frac{G_S}{4}(a_\mu^S - a_e^S) \right\} \tag{AI-12}$$

The order of the lepton fields in the mu-decay hamiltonian is a consequence of the absence of neutral currents. The order most commonly found in the literature, the charge retention order (Eq.(AI-2) is not found in nature. In the case of a pure V-A interaction one order transforms into the other. Experimentally, only charged lepton currents have ever been observed, (Eq. AI-1), as will be shown in the following review of experiments. The leptonic current is believed to be

$$\ell_\alpha(x) = \tilde{\mu}\gamma^\alpha(1+i\gamma_5)\nu_\mu + \tilde{e}\gamma^\alpha(1+i\gamma_5)\nu_e + \text{H.C.} \tag{AI-13}$$

All experiments done to date require that the currents have $\Delta Q = \pm 1$. The presence of neutral lepton currents in the weak interaction hamiltonian would give to rise to terms such as

$$\frac{g_{\mu e} g_{NN}}{\sqrt{2}} \left[\tilde{p}\gamma_\alpha(1+i\gamma_5)p + \tilde{n}\gamma_\alpha(1+i\gamma_5)n \right] \tilde{\mu}\gamma^\alpha(1+i\gamma_5)e \tag{AI-14}$$

$$\frac{g_{\mu e} g_{ee}}{\sqrt{2}} \left[\tilde{\mu}\gamma_\alpha(1+i\gamma_5)e \; \tilde{e}\gamma^\alpha(1+i\gamma_5)e \right] \tag{AI-15}$$

$$g_{\mu\mu} G_T \frac{\partial K_{o2}}{\partial x^\alpha} \tilde{\mu}\gamma^\alpha(1+i\gamma_5)\mu + g_{ee} G_T \frac{\partial K_{o2}}{\partial x^\alpha} \tilde{e}\gamma^\alpha(1+i\gamma_5)e \tag{AI-16}$$

The first of these terms, Eq.(AI-14), would give rise to the process

$$\mu^- + N(A,Z) \rightarrow e^- + N^*(A,Z) \quad . \qquad \text{(AI-17)}$$

N(A,Z) is a nucleus of atomic number A and charge Z. $N^*(A,Z)$ is a collection of A nucleons of which Z are charged. The experimental upper limit of the process is 2.5×10^{-7} times smaller than the allowed process[40] given by Eq.(AI-17).

$$\mu^- + N(A,Z) \rightarrow \nu_\mu + N^*(A,Z-1) \quad . \qquad \text{(AI-18)}$$

Hence a lower limit on $g_{\mu d} g_{nn}$ may be established as $g_{\mu e} g_{nn} < 5 \times 10^{-4}\ G_f$.

Similarly, the term of Eq. (AI-15) would give rise to the decay mode of the μ-meson.

$$\mu^+ \rightarrow e^+ + e^- + e^- \quad . \qquad \text{(AI-19)}$$

The branching ratio of this mode to the decay mode $\mu^+ \rightarrow e^+ + \bar{\nu}_r + \nu_e$ is less than 1.5×10^{-7}, [41] consequently, $g_{\mu e} g_{ee} < 4 \times 10^{-4}\ G_f$. Both of these processes could also occur if ν_μ and ν_e were the same through electromagnetic interactions. The most direct experimental evidence for the lack of neutral currents is their absence in K_{o2} decay. If a neutral current existed then using the term Eq.(AI-16) in the decay hamiltonian the rate

$K_{o2} \rightarrow \mu^+ + \mu^-$ to $K^+ \rightarrow \mu^+ + \nu_\mu$ would be [42]

$$\frac{R(K_{o2} \rightarrow \mu^+ + \mu^-)}{R(K^+ \rightarrow \mu^+ + \nu)} = \frac{|g_{\mu\mu}|^2}{G_f} \frac{m_K^3 (m_K^2 - 4m_\mu^2)^{1/2}}{(m_K^2 - m_\mu^2)^2} = \frac{|g_{\mu\mu}|^2}{G_f} \qquad \text{(AI-20)}$$

the branching ratio $K_{o2} \rightarrow \mu^+ + \mu^-$ to all modes of K_{o2} decay is experimentally known[43] to be less than 10^{-4}.

$$(g_{\mu\mu})^2 < 5 \times 10^{-5} G_f$$

Moreover, neutral currents if present would be detected by the K^+ decay into $\pi^+e^+e^-$, $\pi^+\mu^+\mu^-$ or $\pi^+\bar{\nu}\nu$. The experimental limit[44] on the branching ratio of the $\pi^+e^+e^-$ to all K^+ decay modes is 2.5×10^{-6}. These modes have not been observed, and this fact reinforces the above conclusion.

The current written in Eq.(AI-13) satisfies conservation of leptons and muons. Muon conservation was first established directly in the high energy neutrino experiments. In the experiments done by the Columbia group and the CERN group, it was found that the process[45,46]

$$\nu_\mu + N(A,Z) \rightarrow N^*(A,Z+1) + e^- \qquad \text{(AI-21)}$$

occurred at a rate which was less than 1% of the rate of the allowed process.

$$\nu_\mu + N(A,Z) \rightarrow N^*(A,Z+1) + \mu^- . \qquad \text{(AI-22)}$$

ν_μ is the neutrino from the decay of the positive pion. The result of this experiment is interpreted as the fact that the neutrino from π-decay is different from the neutrino from nuclear β-decay. Indirect evidence for the conservation of muon number comes from the absence of the decay $\mu \rightarrow e + \gamma$. The branching ratio of this decay mode has been measured to be less than 2×10^{-8}.[47] An estimate of the rate for this process in the intermediate boson theory by Feinberg gave branching ratio of [48]

$$\frac{R(\mu \rightarrow e + \gamma)}{R(\mu \rightarrow e\nu\bar{\nu})} \approx \left(\frac{\alpha}{24\pi}\right) N^2 \qquad \text{(AI-23)}$$

where N is a logarithmically diverging constant of order 1.

T.D. Lee pointed out that the non-locality does not need to be provided by a vector boson, since higher order weak interactions will provide such a non-locality. Furthermore, one obtains a result which is comparable to Feinberg's if one uses for a cutoff in the calculation of these divergent processes the unitary limit of weak interactions. In the spirit of the proceeding estimates of coupling constants, the experimental upper limit of $|g_{\mu\nu_e}|^2$ or $|g_{e\nu_\mu}|^2$ would be 10% to 1% of G_f, depending on the interpretation of the $\mu \rightarrow e + \gamma$ result.

Surprisingly enough the conservation of leptons as an independent conservation law is not so well established. The CERN neutrino experiment placed an upper limit of 6% on the lepton non-conserving processes.[45] The lepton violating amplitude can be as large as 25%.

In addition to the lack of neutral currents the next most strongly established absence of a property of the lepton current is the absence of a fundamental scalar and pseudoscalar current. All experiments are consistent with ℓ_α transforming as a vector under proper lorentz transformations. While many experiments are also consistent with a 10% admixture of pseudoscalar coupling there are two important exceptions. The ratio of the decay rate of the π into an electron and a neutrino to the rate for decay into a muon and a neutrino is very sensitive to the presence of a slight admixture of either scalar or pseudoscalar coupling. A similar result is true for the ratio of the same decay modes for the K meson. This ratio has been measured for π-decay and is[11]

$$\frac{R(\pi^+ \to e^+ + \nu)}{R(\pi^+ \to \mu \ + \nu)} = 1.23 \times 10^{-4} \pm 0.02 \ .$$

The agreement with a V-A theory is within the experimental error. If this result is used to put an upper limit on the presence of a term like Eq.(AI-24) in the π-decay hamiltonian

$$G_\pi G_s \pi \left[\frac{\tilde{\mu}(1+i\gamma_5)\nu_\mu}{2} + \frac{\tilde{e}(1+i\gamma_5)\nu_e}{2} \right] \qquad \text{(AI-24)}$$

Then the magnitude of G_S must satisfy the following inequality

$$G_s^{\ 2} < \left(\frac{2\times 10^{-6}}{5} \right) G_f^{\ 2} = 4 \times 10^{-7} \ G_f^{\ 2} \ .$$

The observation of K_{e2} decay has only been done recently and the branching ratio based on three events is consistent with the result predicted by the V-A theory. The value of G_S derived from β-decay is less than 0.01 G_V. This result follows from the absence of pseudoscalar coupling in β-decay.[37]

The limit on the tensor coupling is not as well-established as the case for the scalar coupling; nevertheless, some evidence exists in β-decay and K^+-decay. From form factors of K^+_{e3} and $K^+_{\mu 3}$ decay the value of $G_T < 0.3\ G_V$.[49] From β-decay G_T must be less than 0.1 G_V.[50]

Much better restrictions may be placed on G_T by using the best results for the measurements of ρ, δ, and ξ, as will be shown. Using the relations between the coupling constants obtained in Eq. (AI-3) and (AI-12) and the formulae for ρ, δ, ξ and η given in Refs. 6 and 7, ρ, δ, ξ, and η can be written as

$$\rho = \frac{3}{2\Delta}\left\{G_V{}^2[(1+a_\mu^V a_e^V)^2 + (a_\mu^V+a_e^V)^2] + G_T^2[(1-a_\mu^T a_e^T)^2 + (a_\mu^T-a_e^T)^2]\right\} \quad \text{(AI-25)}$$

$$\delta = \frac{3[G_V{}^2(1+a_\mu^V a_e^V)(a_\mu^V+a_e^V)+G_T{}^2(1-a_\mu^T a_e^T)(a_\mu^T-a_e^T)]}{G_V{}^2[-12(1-a_\mu^V a_e^V)(a_\mu^V-a_e^V)+4(a_\mu^V+a_e^V)(1+a_\mu^V a_e^V)]-47G_T{}^2(1-a_\mu^T a_e^T)(a_\mu^T-a_e^T)} \quad \text{(AI-26)}$$

$$\xi = \frac{-G_V{}^2}{\Delta}[-12(1-a_\mu^V a_e^V)(a_\mu^V-a_e^V)+4(a_\mu^V+a_e^V)(1+a_\mu^V a_e^V)]+47G_T{}^2(1-a_\mu^T a_e^T)(a_\mu^T-a_e^T) \quad \text{(AI-27)}$$

$$\eta = \frac{\frac{12}{\sqrt{2}}G_V G_T}{\Delta}[(1-a_e^T a_\mu^T)(1-a_e^V a_\mu^V)+(a_\mu^V-a_e^V)(a_\mu^T-a_e^T)] \quad \text{(AI-28)}$$

$$\Delta = 2G_V{}^2[(1-a_\mu^V a_e^V)^2+(a_\mu^V-a_e^V)^2+(1+a_\mu^V a_e^V)^2+(a_\mu^V+a_e^V)^2] + \frac{21}{2}G_T{}^2[(1-a_\mu^T a_e^T)^2+(a_\mu^T-a_e^T)^2] \quad \text{(AI-29)}$$

This form is not entirely useful. A more useful form would use the hamiltonian

$$\mathcal{H} = \sqrt{8}G_V'\tilde{\mu}\gamma_\alpha\left[\frac{(1+i\gamma_5)}{2}+\alpha_\mu^V\frac{(1-i\gamma_5)}{2}\right]\nu_\mu\tilde{\nu}_e\left[\frac{(1-i\gamma_5)}{2}+\alpha_e^V\frac{(1+i\gamma_5)}{2}\right]\gamma_\alpha e + \sqrt{8}G_T'\tilde{\mu}\sigma_{\alpha\beta}\left[\frac{(1+i\gamma_5)}{2}+\alpha_\mu^T\frac{(1-i\gamma_5)}{2}\right]\nu_\mu\tilde{\nu}_e\left[\frac{(1-i\gamma_5)}{2}+\alpha_e^T\frac{(1+i\gamma_5)}{2}\right]\sigma_{\alpha\beta}e \quad \text{(AI-30)}$$

The relations between the G's of Eq.(AI-1) and Eq.(AI-30) are given by

$$(G_V') = \frac{(G_V)}{(1+\alpha_\mu^V)(1+\alpha_e^V)} \qquad \alpha_\mu^V = \frac{1-a_\mu^V}{1+a_\mu^V} \qquad \alpha_e^V = \frac{(1-a_e^V)}{(1+a_e^V)} \quad \text{(AI-31)}$$

$$(G_T') = \frac{G_T}{(1+\alpha_\mu^T)(1+\alpha_e^T)} \qquad \alpha_\mu^T = \frac{(1-a_\mu^T)}{(1+a_\mu^T)} \qquad \alpha_e^T = \frac{(1-a_e^T)}{(1+a_e^T)} \quad \text{(AI-32)}$$

Writing the hamiltonian in this way the components of the majorana neutrino which would violate lepton conservation are proportional to one of the α's. The formulae for ρ, δ, ξ, and η then

$$\eta = \frac{\frac{6}{\sqrt{2}}\left(\frac{G_T'}{G_V'}\alpha_\mu^T\alpha_\mu^V + \frac{G_T'}{G_V'}\alpha_e^T\alpha_e^V\right)}{\left(1+(\alpha_\mu^V)^2+(\alpha_e^V)^2+(\alpha_\mu^V\alpha_e^V)^2+\frac{21}{4}\left[\left(\frac{G_T'}{G_V'}\alpha_\mu^T\right)^2+\left(\frac{G_T'}{G_V'}\alpha_e^T\right)^2\right]\right)} \tag{AI-33}$$

$$\xi = -\frac{\left(1-3\left[(\alpha_e^V)^2-(\alpha_\mu^V)^2\right]-(\alpha_\mu^V\alpha_e^V)^2-\frac{47}{4}\left[\left(\frac{G_T'}{G_V'}\alpha_e^T\right)^2-\left(\frac{G_T'}{G_V'}\alpha_\mu^T\right)^2\right]\right)}{\left(1+(\alpha_\mu^V)^2+(\alpha_e^V)^2+(\alpha_\mu^V\alpha_e^V)^2+\frac{21}{4}\left[\left(\frac{G_T'}{G_V'}\alpha_e^T\right)^2+\left(\frac{G_T'}{G_V'}\alpha_\mu^T\right)^2\right]\right)} \tag{AI-34}$$

$$\delta = \frac{3}{4}\,\frac{\left(1-(\alpha_\mu^V\alpha_e^V)^2+\left(\frac{G_T'}{G_V'}\alpha_e^T\right)^2-\left(\frac{G_T'}{G_V'}\alpha_\mu^T\right)^2\right)}{\left(1-3\left[(\alpha_e^V)^2-(\alpha_\mu^V)^2\right]-(\alpha_\mu^V\alpha_e^V)^2-\frac{47}{4}\left[\left(\frac{G_T'}{G_V'}\alpha_e^T\right)^2-\left(\frac{G_T'}{G_V'}\alpha_\mu^T\right)^2\right]\right)} \tag{AI-35}$$

$$\rho = \frac{3}{4}\,\frac{\left(1+(\alpha_\mu^V\alpha_e^V)^2+\left(\frac{G_T'}{G_V'}\alpha_e^T\right)^2+\left(\frac{G_T'}{G_V'}\alpha_\mu^T\right)^2\right)}{\left(1+(\alpha_\mu^V)^2+(\alpha_e^V)^2+(\alpha_\mu^V a_e^V)^2+\frac{21}{4}\left[\left(\frac{G_T'}{G_V'}\alpha_e^T\right)^2+\left(\frac{G_T'}{G_V'}\alpha_\mu^T\right)^2\right]\right)} \tag{AI-36}$$

In this form there are only four independent parameters, α_μ^V, α_e^V, $\frac{G_T'\alpha_\mu^T}{G_V'}$, and $\frac{G_T'}{G_V'}\alpha_e^T$. The analysis of β-decay experiments can be used to set limits of $(\alpha_e^V)^2 < 0.01$, $(\frac{G_T}{G_V}\alpha_e^T)^2 < 0.01$.

By using the best experimental values for ξ and δ,[12,13] the limits on $\frac{G'_T}{G'_V}\alpha_\mu^T$ and α_μ^V can be set as follows:

$$|\alpha_\mu^V| < 0.2 \qquad\qquad |\frac{G'_T}{G'_V}\alpha_\mu^T| < 0.02$$

As a result η can be restricted to $\eta < 0.04$.

APPENDIX II

Sonic System Electronics

The sonic data unit can be used to measure a variety of experimental data. These include measurement of sonic transit times to ± 0.2 μsec, decay times of muons to ± 10 nsec, and pulse heights of fast counter pulses. In all cases three features are retained: the experimental information which is inthe form of a set of pulses is converted to a time interval; the time interval is scaled by a crystal-controlled oscillator and stored on a set of four-decade BCD scalers; at the conclusion of each event all the data in the scalars are transmitted to the memory of a 1401 computer and then recorded on magnetic tape.

The sonic data system is composed of a 1401 computing system and a sonic data unit. The sonic data unit is made up of the following electronic units:

a) Eight or more digitron chasses

b) A main pulse generator chassis

c) A 1401 control chassis

d) A main control chassis.

These units are described in detail in the following paragraphs. A brief description of the 1401 system is also included.

A. Digitron Chassis Description

The digitron chassis accepts pulses from the experiment electronics and converts this information to digital data under the control of the main pulse generator. Several types of these units have been built, a list of which is given below:

1. Sonic transit time digitron (5 Mc)
2. 100 Mc digitron
3. Scintillation counter pulse height analyzer
4. Counter hodoscope register.

In each case the data are converted to digital form and stored on the four-decade BCD scales. The means by which the data are formed depend to some extent on the particular application. The sonic transit time digitron chassis which was the original unit constructed is described here. A block diagram of this is shown in Fig. 24.

The microphone pulse is amplified by a factor of 1000 in an amplifier, the band pass of which is matched to the microphone. The amplified signal varies from 0.25 volts to 5 volts depending on how far the spark was from the microphone. The amplified pulse triggers a discriminator which in turn resets the time interval flip-flop.

Since the rise time of the amplified microphone pulse is 1 μsec, it is necessary to compensate for the variation in the pulse height. This can be done simply by using an exponentially decaying discriminator bias since the smallest pulses arrive last. The pulse height actually varies inversely with time, as shown in Fig. 25. The amplifier is a narrow band pass amplifier passing frequencies from 100 kc to 2 Mc. Outside these limits the rejection is 6 dB per octave. The band width is matched to the resonant frequency of the lead-zirconate microphone.

The time interval flip flop is set by the start gate pulse, a 2-msec pulse delayed by 60 μsec from the instant the spark chambers are fired. The time interval flip-flop if reset by the output of the time interval discriminator and the time interval flip-flop cannot be set again until a new start gate is generated. During the time interval between set and reset a 5.0 Mc oscillator is gated into each four-decade scaler. A block diagram of the scaler is shown in Fig. 37. After the start gate has ended, the main control chassis, the 1401 control chassis, and the 1401 computer control the flow of the data from the scalers by activating chassis and channel select lines located in the digitron chassis. The four digits of a channel are mixed with corresponding digits of the other three channels. The mixed sixteen lines of output are sent to the main control chassis. The code of the scalers is given in Table XV below.

TABLE XV

BCD Code of Decade

Digit	One Line	Two Line	Four Line	Two Prime Line
0	0	0	0	0
1	X	0	0	0
2	0	X	0	0
3	X	X	0	0
4	0	0	X	0
5	X	0	X	0
6	0	X	X	0
7	X	X	X	0
8	0	X	X	X
9	X	X	X	X

This is not the scheme used by the 1401 or the Hewlett-Packard printer. Decoding for these units is done in the main control chassis.

B. Main Pulse Generator Description

With the exception of the trigger amplifier the circuits of the main pulse generator are made from the Nevis slo-logic univibrators, Dwg. No. B30504 and gates, Dwg. No. B2656. The main pulse generator chassis generates pulses which are used to reset all flip-flops, counters, and gate discriminators off during the time which the electrical noise generated by the sparks comes into the sonic data unit. The noise presented a serious problem since complete shielding was not possible. For this reason the noise was considered omnipresent and the logic of the processing was arranged to be independent of its presence.

The main pulse generator block diagram is shown in Fig. 38. The main pulse generator generates three pulses after receiving an input trigger pulse. These pulses are:

1. Reset Pulse - the duration is 50-μsec and is generated promptly from the amplified trigger pulse. The reset pulse is fanned out and sent to each digitron chassis, the 1401 control chassis, and main control chassis. The reset pulse, generated by a univibrator, resets all BCD scalers and flip-flops.
2. Amplifier Gate - the pulse has a duration of 2.0 msec and is generated promptly by a univibrator. The

negative amplifier gate is used to gate the last stage of the digitron amplifier on. The pulse is fanned out eight times in the main pulse generator chassis and sent to each digitron chassis.

3. Start Gate - this pulse has a length of 2 msec and is delayed by 60 μsec. It is generated by making an anticoincidence with the positive amplifier gate and a pulse of 60-μsec duration. Since the leading edge of the start gate is the time with respect to which the sonic transit time intervals are measured, the 60-μsec delay must be generated accurately. The pulse is delayed so that the transit times are measured after the electrical noise due to the spark has decayed to a negligible value. This noise is conducted into the system on the cables which are attached to the microphones from the transducers. It is more than ten times the signal from the sound wave. If scaling were done immediately this noise would cause the clocks to be stopped during the first 10 μsec. The 60 μ-sec pulse is generated by triggering a univibrator with a 100-μsec output pulse. The univibrator pulse is then used to gate a 5-Mc oscillator which drives a four decade scaler of the type described in Fig. 37. When it has counted to 300 the counter output is used to inhibit the 100-μsec univibrator pulse. The scaled 60-μsec pulse is put in anticoincidence with the amplifier gate, thereby generating

the start gate. Because this four-decade scaler can be isolated from the electrical noise, the scaling is not affected. Finally, it is to be noted that the delay is measured with a 5-Mc oscillator which has the same phase as the oscillators for the time intervals, so that this delay does not introduce an additional least count error.

In addition to the aforementioned pulses, the main pulse generator generates the 5-Mc clock signal. This is done first by clipping and then amplifying the output of a 10-Mc crystal oscillator. This output is then scaled down to 5-Mc by driving a flip-flop. The output of the flip-flop is then fanned out eight times and sent to each digitron chassis, where it is reshaped and fanned out four more times to each channel. A block diagram of the main pulse generator is shown in Fig. 38.

C. The Main Control Chassis

The sixteen digit lines coming from each chassis are brought into the main control chassis and then connected together through diodes, a given digit line of all chasses is connected to a common point. The summed digit line pulses are amplified and the sixteen lines are reduced to four lines by combining the corresponding digit of each decade. The block diagram of these circuits is shown in Fig. 39 for the one line. The way in which the digits are sequenced is controlled in the following way. A step sequencer output is generated. The exact way in which the pulse is generated depends on which mode of operation the data unit is in. The only mode which is pertinent to the discussion is the computer mode. Digit sequencing is obtained by driving two flip-flops in series, as shown in Fig. 40. The digit sequencing then drives a set of two flip-flops for the channel select sequencing. The output of the channel select is used to drive three flip-flops which generate the chassis select pulses. The channel select pulses are fanned out eight times and sent to each chassis. The output of the third or last flip flop is used to generate the end of transmission pulse, which is sent to the 1401 control chassis. The select pulse logic is shown in Fig. 41.

D. The 1401 Control Chassis

This chassis controls the flow of data from the BCD scalers to the 1401 memory. A block diagram of it is shown in Fig. 37.

1. The logic for generating the step sequences pulse;
2. A decoder of the 1242 BCD code to a 1248 BCD code; the generation of a parity bit and the drivers for the lines to the 1401.
3. An end of transmission pulse circuit.

The 1401 must provide a I/O Read Call level during data transmission. The I/O Read Call is generated by the 1401 program when the 1401 is ready to read data. When the read call is on,an end-of-time pulse is generated by differentiating the trailing edge of the amplifier gate pulse. The scalers at this time are no longer counting, hence data can be transmitted to the 1401. The end-of-time pulse sets the 1401 control flip-flop, which in turn activates both the 1401 service request line and the step sequencer line. When a service request is generated, the 1401 senses it and reads the data on the data lines into the memory of the 1401. After this is done the following occurs:

a) Advances the location at which the next event will be stored,

b) Sends one clock pulse of 000-090 time,

c) Stops the program until it senses a service request, it is ready to read.

The 090-000 pulses inhibit the service request for 2.8 μsec and at the same time generate step-sequencer pulses, as shown in Fig. 26. This causes the next digit to be placed on the data lines. When the 000-090 pulse is gone the service request comes back on and the 1401 then reads the data lines again. The procedure is repeated until an end-of-transmission pulse is sensed. There are two end-of-transmission pulses, the first one is sent promptly after the trigger. The 1401 is programmed to recognize this as an end-of-transmission. The program simply transfers the data on the lines to a core storage location, stops after one digit, and awaits the arrival of a true service request at which time it reads the data into the core, writing over the noise digits. This added complication is necessary because from time to time a service request would be generated by noise and the data lines would be read promptly. The program would not differentiate this from a real service request and the subsequent digits would be stored in the wrong storage locations.

APPENDIX III

The Experimental Spectrum

A. Data Processing

The fact that 1.5×10^7 events had to be reconstructed made it necessary to use data processing techniques that are out of the ordinary routine encountered by physicists. An outline of the program used in the reconstruction sequence is given here.

The major problem in handling the data was to get data in the computer and in a form the computer could use in a reasonable amount of time. Fortran was entirely unsuitable for the operations which were performed. A data tape written by the 1401 contained tape records of 1536 BCD characters, which represented twelve events of 128 BCD characters. The 7094 is a binary machine which uses 36 Bit words and hence the data must be converted from BCD to binary. Of the 128 BCD characters only 80 contained useful information. The first program in the sequence edited the data tapes and wrote a binary output tape. Each event was read into the 7094 and converted to binary. Each four-digit BCD number was converted to 36 Bit words. The 48 BCD characters which contained no information were deleted. The event was then checked for identity with the previous event, identity with the same event of the previous record and more than one missing spark. If any of these conditions were satisfied the event was rejected and written on the rubbish tape at one event per record. The other events were assembled in core into records of 200 events in two separate categories. Events with one spark were written on one tape - the Missing Spark Tape, and events with no misses were written on another tape - Edited Data Tape. When the events were assembled for writing they were compacted into six 36 bit words. The number of tapes which had to be handled was reduced by a factor of five. The table below shows how many bits were given to each piece of information.

Channels 1 to 4	Chassis 1	12 Bits Per Channel
Channels 1 to 4	Chassis 2	13 Bits Per Channel
Channels 1 to 4	Chassis 3	13 Bits Per Channel
Channels 1 to 4	Chassis 4	13 Bits Per Channel
Channels 1 and 2	Chassis 5	14 Bits Per Channel
Channels 3 and 4	Chassis 7	9 Bits Per Channel

During the editing separate histograms were made of the events which missed each combination of chambers, and of the events which had the wrong record length or form.

After editing the Edited Data Tapes and the Missing Spark Tapes can be reconstructed. The Edited Data Tapes are reconstructed using a 7094 program. After each event is reconstructed the results of the calculation are truncated and stored. Table XVI gives a list of the quantities which are computed and the number of bits which are retained.

TABLE XVI

Information Stored on P' Tape

Variable	No. of Bits	Variable	No. of Bits
1	9	7	3
2	9	8	3
3	9	9	4
4	3	10	4
5	3	11	4
6	3		

Any of the 25 variables on the P tape could be assembled in the list of eleven variables appearing on the P' tape.

The final program in the data processing sequences was the histogram program. This program made a set of three-dimensional histograms; the number of histogram channels could not exceed 2^{15}. A unique feature of the program was the way in which the histogram was constructed. Each event was first tested to see whether it was in the outer limits of each variable; if accepted the first three variables were truncated and reassembled into a single 15 Bit number. This 15 Bit number corresponded to a particular address in the 7094 memory and hence a channel in the histogram. After computing the address, one was added to the contents of the address. The program had the virtue of being exceptionally fast and permitted the use of almost the entire memory for histograms. After all data had been read into the 7094 the contents of the memory were written on tape. The histogram tape was interpreted by a special 1401 program, which provided a set of one-dimensional histograms.

APPENDIX IV

Raw Data

The following histograms present the raw experimental data after angle selection criteria have been imposed. The limits of each variable are given in the first two lines of the table. The top line denotes the lower limit and the second line gives the upper limit. The limits are given in terms of binary numbers. The connection between the binary numbers and the decimal equivalents is as follows:

P		φ_T		α	
0	15 MeV	0	-55^o	0	-7.5^o
511	55 MeV	511	$+35^o$	511	$+7.5^o$

X_T		Z_T		Z_{IV}	
0	+4 cm	0	+4 cm	0	-15 cm
7	-4 cm	7	-4 cm	7	+15 cm

DZ4		PH2		DZ3	
0	-2 MeV/c	0	0	0	-2 MeV/c
7	+2 MeV/c	7	9999	7	+2 MeV/c

PHI		DR4	
1	0.045 MeV	0	-2 MeV/c
12	0.54 MeV	7	+2 MeV/c

The variables are listed from left to right as follows: P, φ_T, α, X_T, Z_T, Z_{IV}, DZ4, PH2, DZ3, PHI and DR4. The histograms list the experimental population for momentum intervals of 40/512 MeV/c.

MOMENTUM HISTOGRAM No. 1

Lower and Upper Limits

0	0	90	192	0	0	0	2	0	6	1	6
9999	511	300	319	7	7	7	5	7	9	12	9

78,472 Total Events 18,333 Total in Histogram 0 Also Total in Histogram

120	0	0	0	0	0	0	1	0	0	0
130	2	2	2	1	2	1	4	0	4	4
140	0	9	5	2	3	6	5	6	2	4
150	8	6	7	7	7	8	13	7	7	12
160	5	10	9	9	11	13	15	11	11	12
170	18	13	13	15	13	18	17	15	24	13
180	19	21	12	19	18	26	17	19	23	21
190	28	35	23	19	28	28	28	27	38	28
200	42	34	28	34	34	36	25	38	40	24
210	36	37	38	31	36	34	37	53	37	34
220	46	51	46	44	38	41	36	31	42	40
230	50	56	44	43	59	49	43	44	47	54
240	53	46	53	40	52	53	46	55	42	51
250	63	40	48	48	51	58	69	63	73	58
260	49	49	46	54	64	62	56	61	61	64
270	54	53	65	65	45	61	48	50	53	64
280	64	68	56	56	71	53	82	44	76	57
290	65	72	53	68	54	53	55	56	64	45
300	69	53	59	67	60	67	65	59	50	72
310	80	67	63	67	81	60	66	78	65	62
320	72	58	66	61	65	59	68	56	79	62
330	64	67	67	56	79	58	68	75	55	61
340	76	71	59	66	59	71	72	65	70	61
350	61	69	60	62	67	80	72	73	91	63
360	63	65	62	64	71	64	62	67	72	73
370	65	66	71	60	66	76	61	69	66	63
380	78	68	65	54	69	65	70	85	65	77
390	70	76	64	59	60	64	66	68	78	61
400	70	69	66	78	92	74	42	72	61	72
410	83	86	77	68	77	74	58	70	65	77
420	79	56	76	74	73	69	79	74	68	78
430	75	62	67	67	71	62	67	80	78	61
440	69	90	70	88	78	88	64	59	82	77
450	66	77	73	59	58	67	71	74	64	69
460	61	66	62	79	67	71	69	64	64	71
470	60	85	61	72	69	74	62	50	53	56
480	64	49	31	13	10	4	3	0	1	0
490	1	0	0	0	0	0	0	0	0	0

For P Between 0 and 119 All Sums are Zero
Between 500 and 511 All Sums are Zero

1 P 512

18,333 Events in Above Histogram 512 Boxes in Above Histogram

7.2 kG

MOMENTUM HISTOGRAM No.2 - Lower and Upper Limits

0	0	90	192	0	0	0	2	0	6	1	6
999	511	300	319	7	7	7	5	7	9	12	9

3,867,972 Total Events 986,150 Total in Histogram 0 also Total in Histo.

1 P 512 For P Between 0 and 79 all sums are Zero

80	0	2	3	3	7	13	18	18	20	30
90	35	47	44	47	58	59	75	77	81	97
100	105	115	119	127	151	167	185	185	213	224
110	233	227	267	254	294	293	340	315	369	325
120	372	396	419	426	432	474	453	534	561	517
130	616	594	586	615	638	677	710	710	719	844
140	808	779	800	906	955	879	993	1057	1016	1115
150	1123	1069	1095	1181	1222	1332	1292	1316	1373	1341
160	1335	1435	1481	1485	1508	1511	1602	1618	1624	1728
170	1728	1654	1709	1752	1886	1914	1934	1955	1948	1936
180	1973	1956	1976	1992	2078	2025	2029	2069	2136	2148
190	2159	2102	2173	2165	2245	2307	2207	2245	2273	2196
200	2214	2329	2279	2369	2287	2332	2325	2228	2329	2376
210	2384	2346	2408	2470	2438	2431	2418	2440	2463	2440
220	2568	2371	2517	2423	2536	2550	2487	2505	2549	2592
230	2550	2563	2613	2587	2449	2598	2568	2621	2634	2585
240	2683	2668	2605	2610	2690	2604	2690	2719	2708	2684
250	2738	2688	2784	2756	2848	2717	2619	2669	2832	2768
260	2750	2751	2864	2777	2737	2828	2879	2824	2716	2768
270	2859	2825	2893	2785	2935	2917	2857	2881	2942	2822
280	2854	2951	2839	2911	2916	2190	3001	2989	3047	2935
290	2931	2974	2928	3056	2891	2994	3026	3065	2983	3000
300	2954	3076	3043	3070	3116	3102	3078	3131	3129	3017
310	3089	3092	3049	3119	3148	3129	3128	3134	3040	3182
320	3317	3160	3129	2958	3115	3283	3263	3115	3210	3217
330	3242	3160	3156	3129	3235	3184	3246	3285	3265	3279
340	3248	3252	3194	3277	3148	3234	3194	3338	3229	3303
350	3154	3241	3227	3189	3323	3357	3384	3282	3355	3361
360	3293	3374	3259	3297	3320	3342	3321	3267	3383	3267
370	3381	3374	3251	3374	3402	3370	3332	3380	3338	3344
380	3395	3426	3339	3416	3479	3362	3405	3450	3509	3357
390	3337	3316	3368	3475	3383	3346	3453	3357	3499	3357
400	3363	3373	3470	3347	3355	3353	3454	3494	3504	3393
410	3464	3413	3426	3467	3465	3460	3331	3385	3402	3568
420	3392	3375	3427	3419	3452	3499	3446	3398	3439	3364
430	3382	3471	3391	3443	3416	3370	3542	3434	3381	3432
440	3394	3507	3425	3428	3326	3595	3468	3352	3468	3452
450	3402	3422	3454	3443	3510	3409	3409	3355	3386	3424
460	3405	3390	3413	3342	3235	3345	3419	3419	3360	3378
470	3372	3321	3250	3296	3257	3207	3148	3088	2946	2750
480	2458	1900	1255	670	373	180	94	31	21	12
490	8	1	0	3	2	1	0	0	1	0
500	1	0	0	0	0	0	0	0	0	0

For P Between 510 and 511 all sums are Zero

986,150 Events in Above Histogram 512 Boxes in Above Histogram

6.6 kG

MOMENTUM HISTOGRAM No. 3 - Lower and Upper Limits

0	0	90	192	0	0	0	2	0	6	1	6
9999	511	300	319	7	7	7	5	7	9	12	9

2,111,626 Total Events 614,524 Total in Histogram 0 also Total in Hist.

1 P 512 For P between 0 and 19 all sums are Zero

20	0	0	0	0	0	0	0	0	0	1
30	2	1	0	4	3	11	12	13	14	17
40	20	26	24	41	33	35	31	74	70	78
50	70	90	70	74	100	101	131	112	114	130
60	150	135	145	171	184	189	204	218	204	249
70	230	338	271	297	285	331	310	373	369	356
80	373	416	431	426	459	513	516	483	561	577
90	601	631	582	657	644	657	675	778	754	779
100	785	808	900	887	911	935	892	920	930	976
110	973	947	999	994	1103	1042	1070	1037	1032	1061
120	1139	1066	1205	1134	1294	1233	1189	1168	1159	1235
130	1183	1224	1206	1134	1187	1170	1322	1228	1296	1255
140	1238	1355	1284	1220	1324	1228	1265	1312	1335	1427
150	1343	1374	1357	1335	1369	1314	1342	1311	1340	1374
160	1366	1432	1343	1369	1359	1500	1452	1449	1379	1511
170	1418	1382	1407	1413	1425	1412	1481	1456	1542	1489
180	1509	1487	1476	1508	1508	1552	1534	1506	1582	1587
190	1577	1586	1632	1666	1542	1618	1509	1601	1644	1592
200	1635	1588	1576	1629	1603	1620	1569	1540	1640	1663
210	1653	1675	1727	1690	1721	1742	1665	1664	1752	1643
220	1675	1732	1677	1635	1774	1743	1689	1728	1881	1719
230	1816	1686	1689	1685	1785	1727	1721	1774	1693	1761
240	1788	1883	1826	1767	1838	1862	1842	1792	1853	1774
250	1861	1779	1817	1802	1871	1888	1872	1843	1873	1949
260	1839	1860	1857	1859	1801	1906	1912	1983	1886	1947
270	1809	1946	1920	1918	1983	1967	1908	1988	1958	1901
280	1910	1974	1960	2048	2072	2015	1950	1954	2040	2022
290	2075	1984	1988	1947	2014	1992	2079	2058	1952	1973
300	2015	2014	2047	2075	2022	2031	1978	2019	1981	2075
310	2016	2088	2117	2074	2092	2114	2120	2127	2132	2058
320	2066	2101	2076	2119	2160	2055	2236	2123	2206	2168
330	2135	2170	2157	2147	2198	2194	2144	2103	2098	2153
340	2165	2211	2213	2169	2081	2149	2305	2301	2165	2192
350	2236	2257	2202	2240	2194	2139	2113	2214	2200	2184
360	2273	2188	2206	2204	2216	2237	2222	2171	2340	2248
370	2291	2163	2192	2363	2292	2284	2266	2270	2277	2261
380	2402	2236	2306	2277	2237	2276	2320	2195	2249	2247
390	2236	2278	2191	2110	2111	2127	2160	2051	2070	2105
400	2018	1968	1959	1865	1920	1869	1868	1836	1788	1762
410	1800	1764	1699	1686	1662	1702	1589	1459	1482	1466
420	1445	1390	1390	1286	1308	1335	1232	1166	1073	1138
430	998	1073	957	947	991	878	873	893	802	819
440	765	753	756	697	622	653	578	534	491	463
450	458	392	369	332	324	286	265	225	199	183
460	149	140	115	93	81	57	67	46	33	28
470	26	27	19	14	9	6	4	5	0	1

For P Between 480 and 511 all sums are Zero

5.3 kG

REFERENCES

[1] T. Kinoshita and A. Sirlin, Phys. Rev. 113, 1652 (1959). This paper contains reference to earlier work.

[2] The diagrams for the emission of photons must be included with the other electromagnetic corrections if an infrared divergence is to be avoided. The problem is discussed in Sec. V. No such divergence exists in the case of pion-nucleon coupling.

[3] S.L. Adler, Phys. Rev. Letters 14, 1051 (1965); W.I. Weissberger, Phys. Rev. Letters 14, 1047 (1965). The values of G_A/G_V computed in the preceding papers were 1.24 and 1.16, respectively.

[4] R.P. Feynman and M. Gell-Mann, Phys. Rev. 109, 193 (1958).

[5] N. Cabibbo, Phys. Rev. Letters 10, 513 (1963).

[6] The calculation was first carried out by L. Michel for a Hamiltonian that was separately C, P, and T invariant in Proc. Phys. Soc. (London) A63, 514 (1950). After non-conservation of parity was discovered the interaction was treated more generally in C. Bouchiat and L. Michel, Phys. Rev. 106, 170 (1957).

[7] T. Kinoshita and A. Sirlin, Phys. Rev. 107, 593 (1957).

[8] C.S. Wu, E. Ambler, R.W. Hayward, D.D. Hopper and K.P. Hudson, Phys. Rev. 105, 1413 (1957).

[9] R.L. Garwin, L.M. Lederman, and M. Weinrich, Phys. Rev. 105, 1415 (1957); J.I. Friedman and V.L. Telegdi, Phys. Rev. 106, 1290 (1957).

[10] T.D. Lee and C.N. Yang, Phys. Rev. 105, 1671 (1957); A. Salam, Nuovo Cimento 5, 299 (1957); L. Landau, Nucl. Phys. 3, 127 (1957).

[11] E. Dicapua, R. Garland, L. Pondrom and A. Strelzoff, Phys. Rev. 133, B1332 (1964).

[12] M. Bardon, D. Berley, and L.M. Lederman, Phys. Rev. Letters 2, 56 (1959).

[13] R. Plano, Phys. Rev. 119, 1400 (1960).

[14] M. Bardon, P. Franzini, and J. Lee, Phys. Rev. Letters 7, 23, (1961).

[15] R. Sard and B. Pontecorvo, Phys. Rev. 77, 102 (1950).

[16] L.W. Nordheim, Phys. Rev. 59, 544 (1941), first proposed that the muon decayed as $\mu \rightarrow e + \nu + \bar{\nu}$, when $e + \nu$ or $e + \gamma$ were found too inconsistent with his experimental evidence. The amount of data was too small to be conclusive, and two later experiments by E.P. Hincks and B. Pontecorvo, Phys. Rev. 73, 257 (1948), and R.D. Sard and E.J. Althaus, Phys. Rev. 74, 1364 (1948), with sufficient data demonstrated that $e + \gamma$ and $e + \nu + \gamma$ were either rare decay modes or absent.

[17] E. Hyman, Ph.D. Thesis (1966), Columbia University, unpublished.

[18] J. Steinberger, Phys. Rev. 75, 1136 (1949).

[19] R.B. Anderson, C.D. Anderson and A.J. Seriff, Phys. Rev. 75, 1446 (1949) G1 and G2.

[20] a H.J. Bramson and W.W. Havens, Phys. Rev. 83, 862 (1951); Bramson, Havens, and Seifert, ibid. 88, 304 (1952).

b Villain and Williams, Phys. Rev. 94, 1011 (1954).

c Sargent, Rinehart, Lederman and Rodgers, Phys. Rev. 99, 885 (1955).

[20] d L. Rosenson, Phys. Rev. 109, 958 (1958).

e Dudziak, Sagane, and Vedder, Phys. Rev. 114, 336 (1959).

f R. Plano, Phys. Rev. 119, 1400 (1960).

g M. Block, E. Fiorinni, E. Kikuchi, G. Giacomelli, and S. Ratti, Nuovo Cimento 23, 1114 (1962).

h J. Barlow, P. Booth, L. Carrol, G. Court, J. Davis, D. Edwards, R. Johnson, and J. Wormold, Proc. Phys. Soc. (London) 84, 239 (1964).

[21] Previous reports of the detailed operations of this system have been given in M. Bardon, J. Lee, J. Peoples, A.M. Sachs, Proceedings of CERN Conference on Film-less Spark Chamber Techniques, (Geneva, Switzerland) CERN 64-30 P. 41, March 1964.

[22] H. Fullbright and D. Kohler, University of Rochester Report, NYO-9540, 1961 (preprint).

[23] B. Maglic and F. Kirsten, Nucl. Instr. Methods 17, 49 (1962).

[24] R. Burns, K. Goulianos, E. Hyman, L. Lederman, W. Lee, N. Mistry, J. Rettberg, M. Schwartz and J. Sunderland, Phys. Rev. Letters 15, 42 (1965);
G. Bernardini, H. Bienlein, A. Böhm, G. von Dardel, H. Faissner, F. Ferrero, J-M. Gaillard, H.J. Gerber, B. Hahn, M. Holder, V. Kaftanov, F. Krienen, C. Manfredotti, M. Reinharz, R.A. Salmeron, A. Staude, H.J. Steiner, J. Bartley, M.M. Block, H. Burmeister, D.C. Cundy, B. Eiben, C. Franzinetti, J. Keren, R. Møllerud, G. Myatt, M. Kikolic, A. Orkin-Lecourtois, M. Paty, D.H. Perkins, C.A. Ramm, K. Schultzer, H. Sletten, K. Soop, R. Stump, W. Venus and H. Yoshiki, Nuovo Cimento 38, 608 (1965).

[25] R. Burns, G. Danby, E. Hyman, L.M. Lederman, W. Lee, J. Rettberg, J. Sunderland, Phys. Rev. Letters 15, 831 (1965).

[26] T.D. Lee, Phys. Rev. 128, 899 (1962).

[27] C. Rey, Phys. Rev. 135, B1215 (1964).

[28] H.A. Bethe and W. Heitler, Proc. Roy. Soc. (London) A146, 83 (1934).

[29] L. Landau, Journal of Physics (U.S.S.R.) 8, 201 (1944).

[30] E.L. Goldwasser, F.E. Mills, and A.O. Hanson, Phys. Rev. 88, 1137 (1952).

[31] Charpak, G., Farley, F., Garwin, R., Muller, T., Sens, J., Zichichi, A., Physics Letters 1, 16 (1962).

[32] Langer, L.M. and Moffat, R.J.D., Phys. Rev. 88, 689 (1952); Hamilton, D.R., Alford, W.P., and Gross, L., Phys. Rev. 92, 1521 (1953).

[33] M. Bardon, P. Norton, J. Peoples, A.M. Sachs and J. Lee-Franzini, Phys. Rev. Letters 14, 505 (1965).

[34] W. Heitler, The Quantum Theory of Radiation, Third Ed., p. 268 (Oxford at Clarendon Press 1954).

[35] W. Heitler, ibid, p. 273.

[36] B. Rossi, High Energy Particles, p. 15 (Prentice Hall, New York 1952).

[37] T.D. Lee and C.S. Wu, Ann. Rev. Nucl. Sci. 15, Chapter 4,(1965).

[38] R. Friedberg, Phys. Rev. 129, 2298 (1962).

[39] R. Ehrlich, D. Fryberger, R. Powers, B. Sherwood, V. Telegdi, J. Bonnin, Phys. Rev. Letters 16, 540 (1966).

[40] M. Conversi, L. di Lella, G. Penso, M. Toller, and C. Rubbia, Phys. Rev. Letters 8, 125 (1962).

[41] S. Frankel, W. Frati, J. Halpern, L. Holloway, W. Wales, O. Chamberlain, Phys. Rev. 130, 351 (1963).

[42] T.D. Lee and C.N. Yang, Phys. Rev. 119, 1410 (1960).

[43] W.J. Willis, Proceedings of the International Conference on Weak Interactions (1965), (Argonne, Illinois, to be published); ANL-7130, page 160.

[44] G. Trilling, ibid., page 117.

[45] M.M. Block, H. Burmeister, D.C. Cundy, B. Eiben, C. Franzinetti, J. Keren, R. Møllerud, G. Myatt, M. Nikolic, A. Orkin-LeCourtois, M. Paty, D.H. Perkins, C.A. Ramm, K. Schultze, H. Sletten, K. Soop, R. Stump, W. Venus, and H. Yoshiki, Physics Letters 12, 281 (1964); G. Bernardini, J.K. Bienlein, G. von Dardell, H. Faissner, F. Ferrero, J.M. Gaillard, H.J. Gerber, B. Hahn, V. Kaftanov, F. Krienen, C. Manfredotti, M. Reinharz, and R.A. Salmeron, Physics Letters 13, 86 (1964).

[46] R. Burns, Ph.D. Thesis, Columbia University (1966) (preprint).

[47] D. Bartlett, S. Devons, and A.M. Sachs, Phys. Rev. Letters 8, 120 (1962); S. Frankel, W. Frati, J. Halpern, L. Holloway, W. Wales and O. Chamberlain, Nuovo Cimento 27, 894 (1963).

[48] G. Feinberg, Phys. Rev. 110, 1482 (1958).

FIGURE CAPTIONS

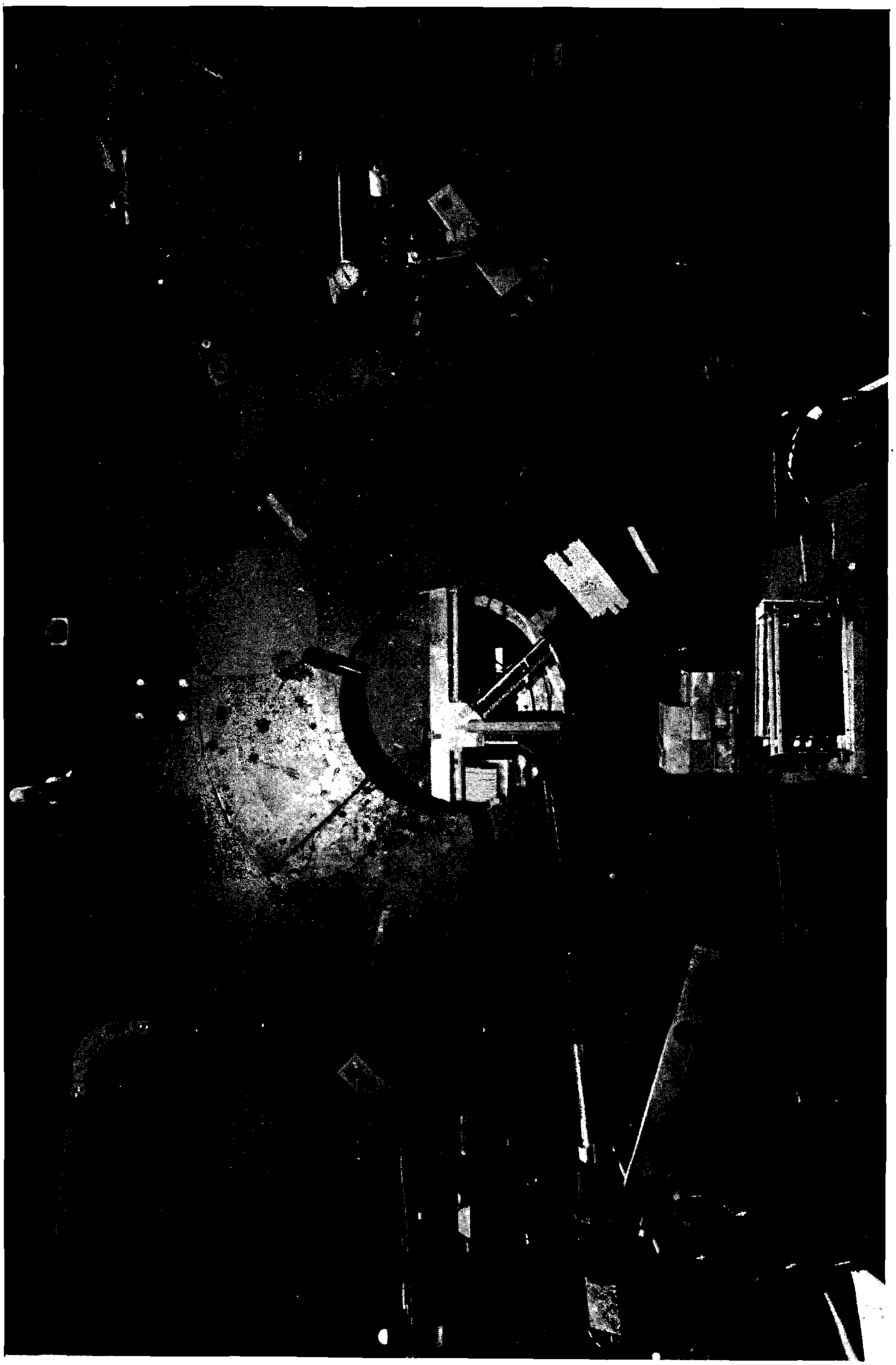

Fig 3

FINAL ARRANGEMENT OF SHIM COILS IN CLOUD CHAMBER MAGNET

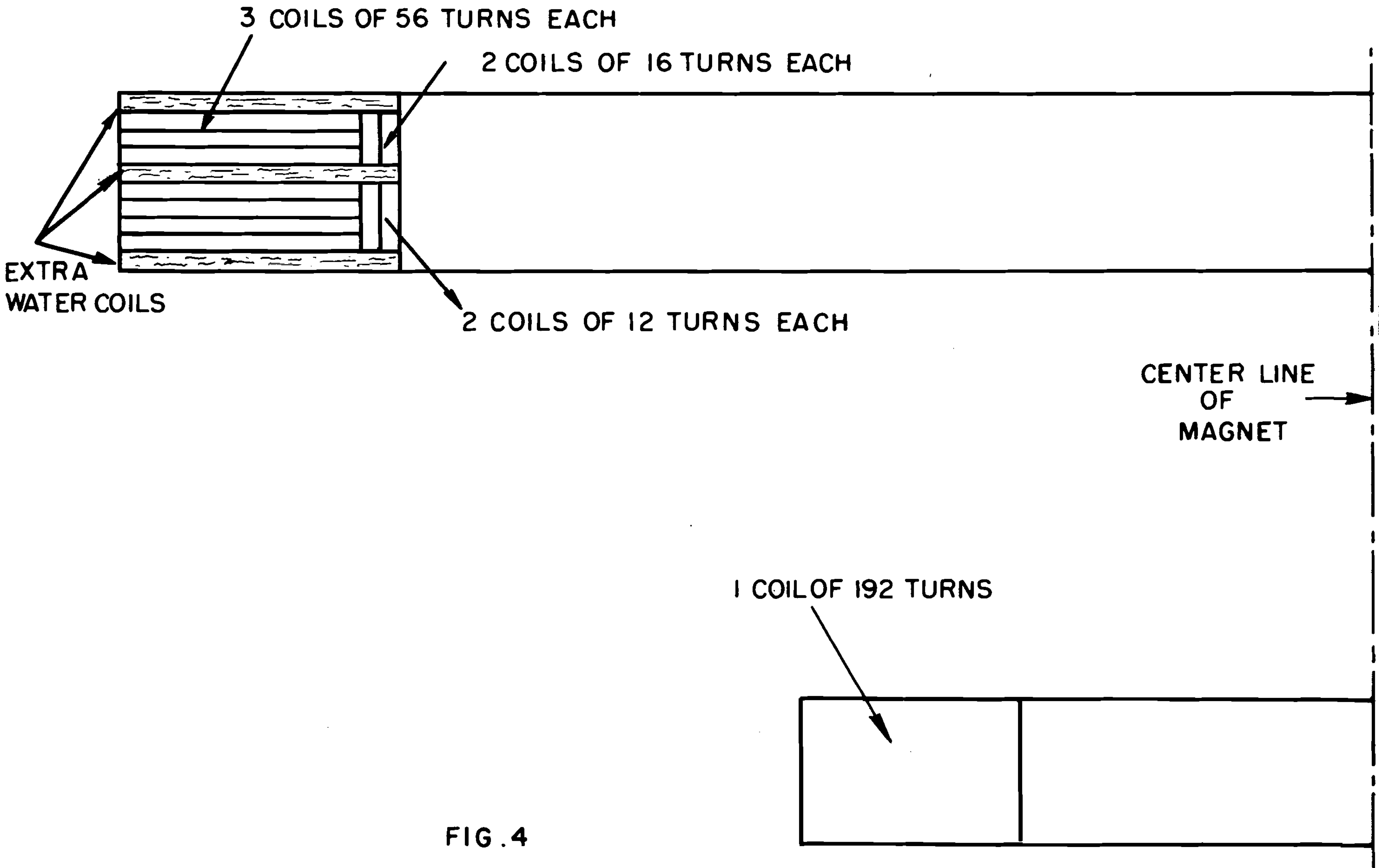

FIG. 4

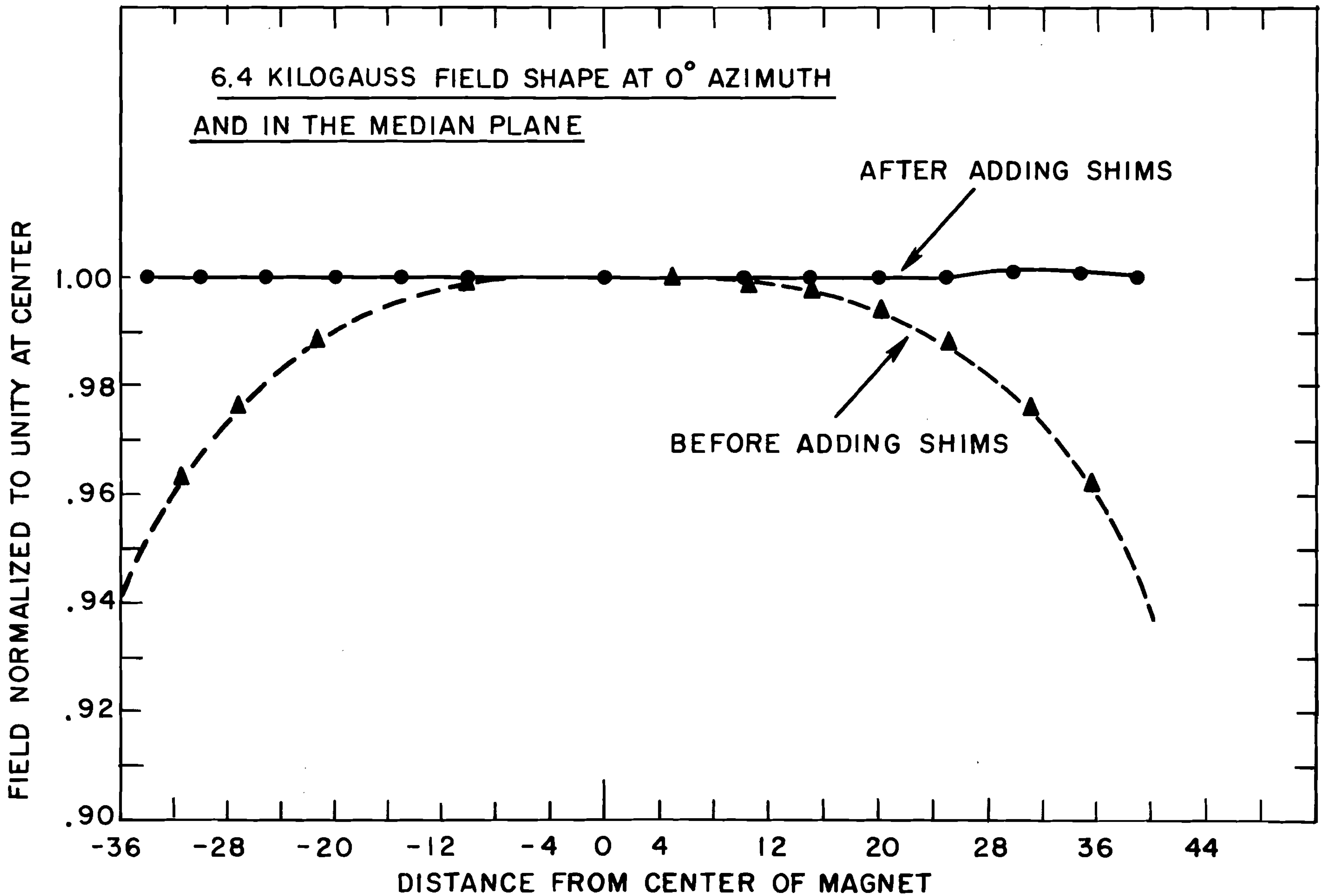
6.4 KILOGAUSS FIELD SHAPE AT 0° AZIMUTH
AND IN THE MEDIAN PLANE
AFTER ADDING SHIMS
BEFORE ADDING SHIMS
FIELD NORMALIZED TO UNITY AT CENTER
1.00
.98
.96
.94
.92
.90
-36
-28
-20
-12
-4
0
4
12
20
28
36
44
DISTANCE FROM CENTER OF MAGNET

FIG. 5

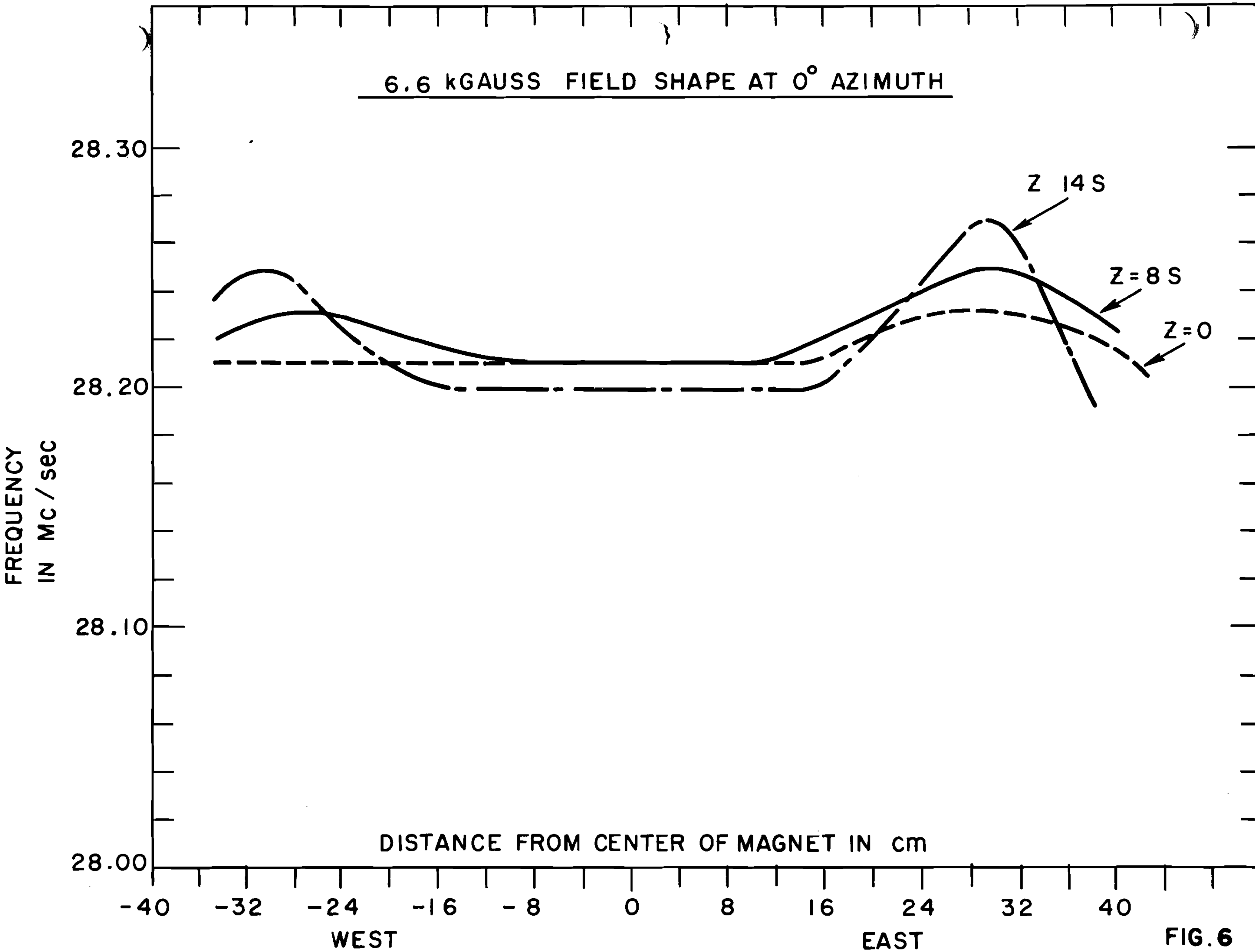
6.6 kGAUSS FIELD SHAPE AT 0° AZIMUTH
Z 14 S
Z = 8 S
Z = 0
28.30
28.20
28.10
28.00
FREQUENCY IN Mc/sec
DISTANCE FROM CENTER OF MAGNET IN cm
-40
-32
-24
-16
-8
0
8
16
24
32
40
WEST
EAST

FIG. 6

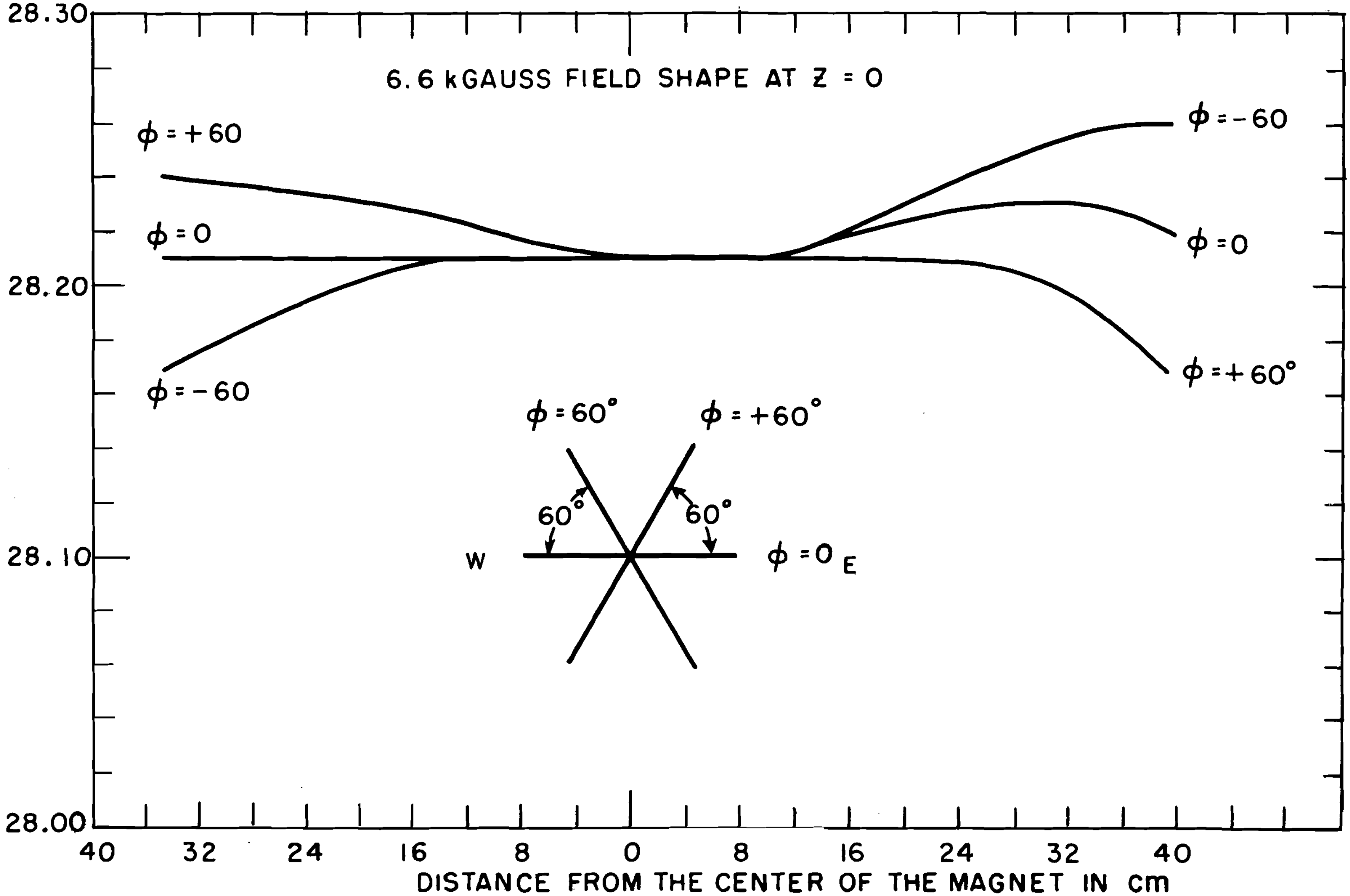
6.6 kGAUSS FIELD SHAPE AT Z = 0
28.30
28.20
28.10
28.00
φ = +60
φ = 0
φ = -60
φ = -60
φ = 0
φ = +60°
φ = 60°
φ = +60°
60°
60°
W
φ = 0 E
40
32
24
16
8
0
8
16
24
32
40
DISTANCE FROM THE CENTER OF THE MAGNET IN cm

FIG. 7

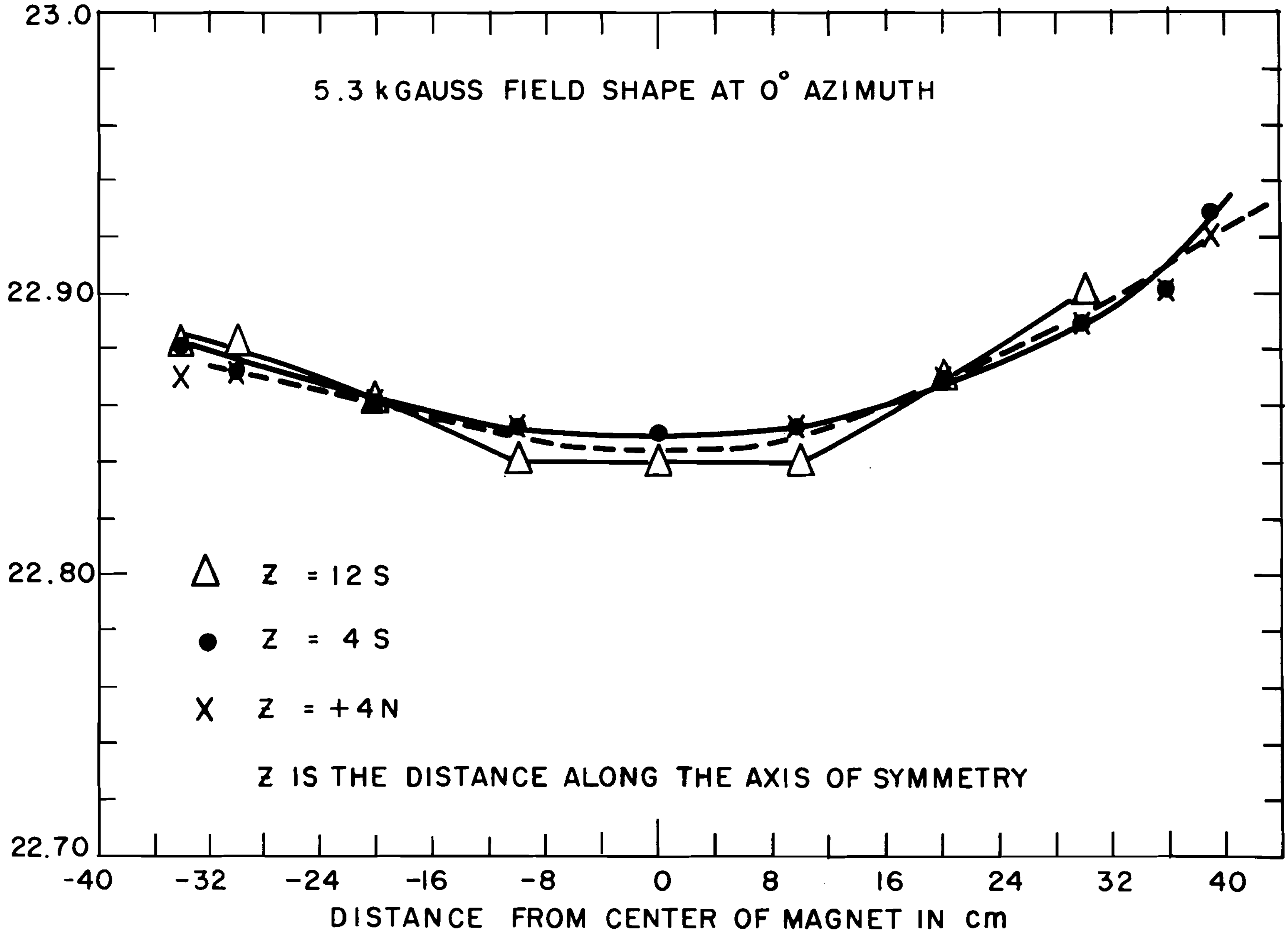
5.3 kGAUSS FIELD SHAPE AT 0° AZIMUTH
23.0
22.90
22.80
22.70
-40
-32
-24
-16
-8
0
8
16
24
32
40
DISTANCE FROM CENTER OF MAGNET IN cm
Δ Z = 12 S
● Z = 4 S
X Z = +4 N
Z IS THE DISTANCE ALONG THE AXIS OF SYMMETRY

FIG. 8

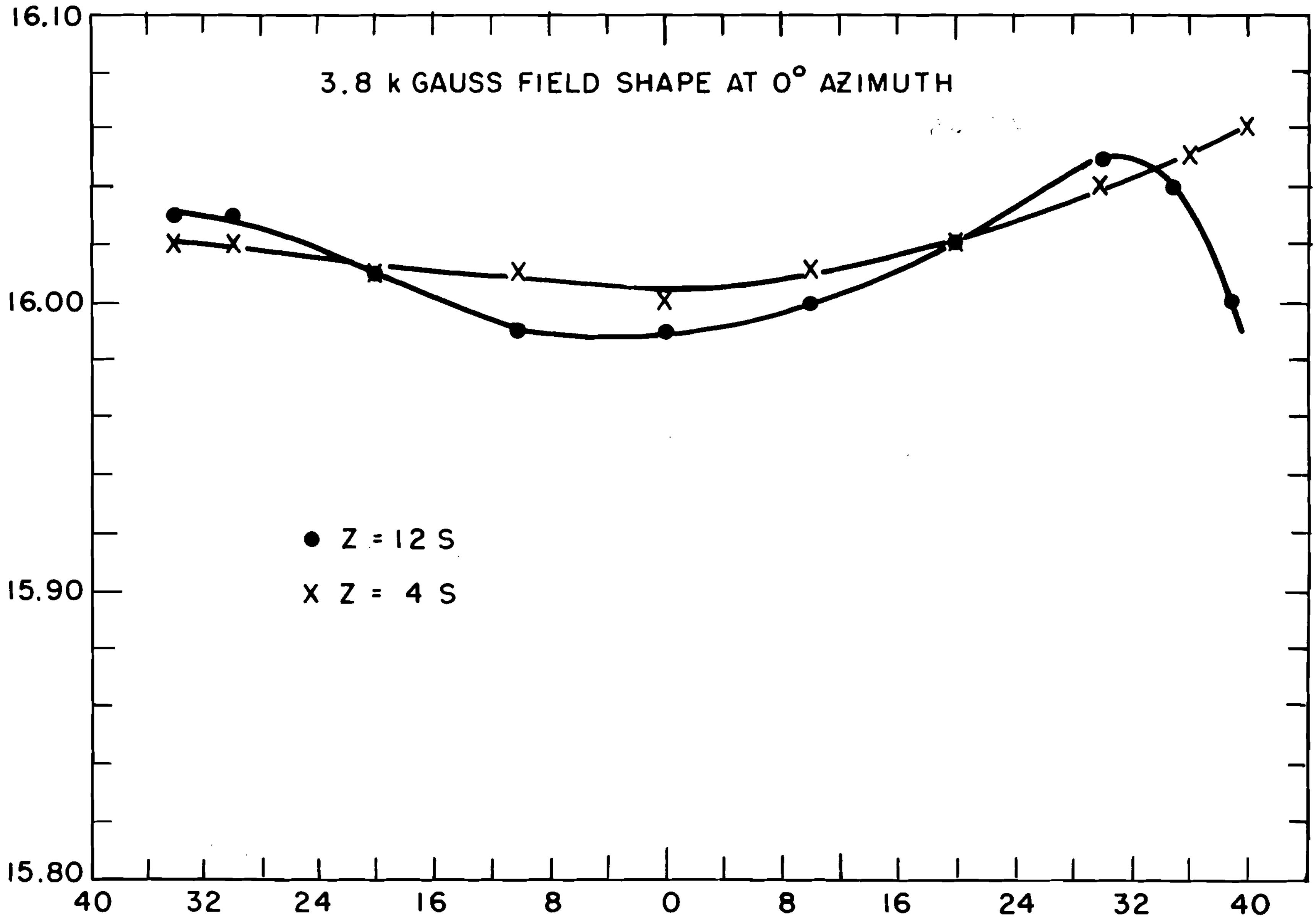
3.8 k GAUSS FIELD SHAPE AT 0° AZIMUTH
● Z = 12 S
X Z = 4 S
16.10
16.00
15.90
15.80
40
32
24
16
8
0
8
16
24
32
40

FIG. 9

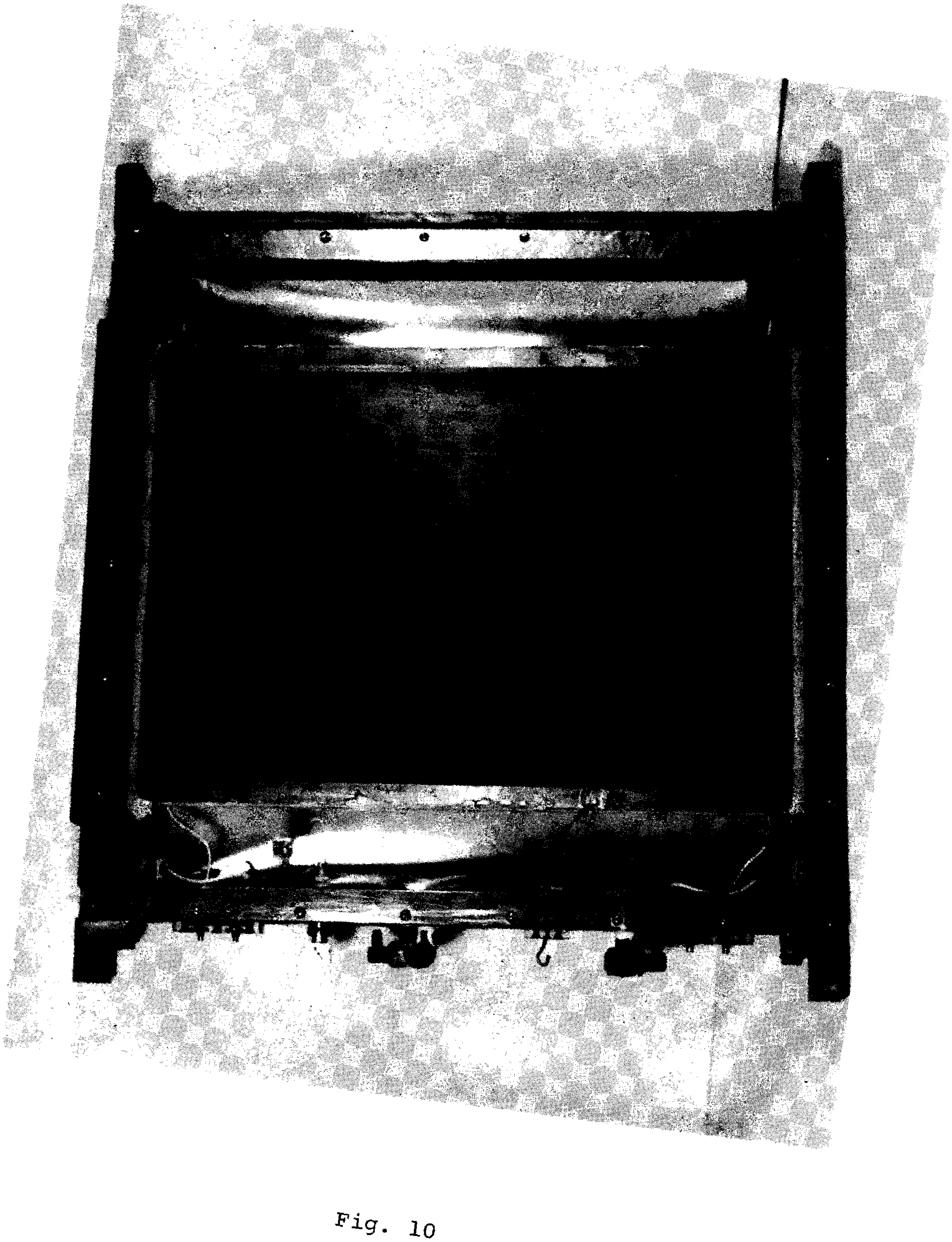

Fig. 10

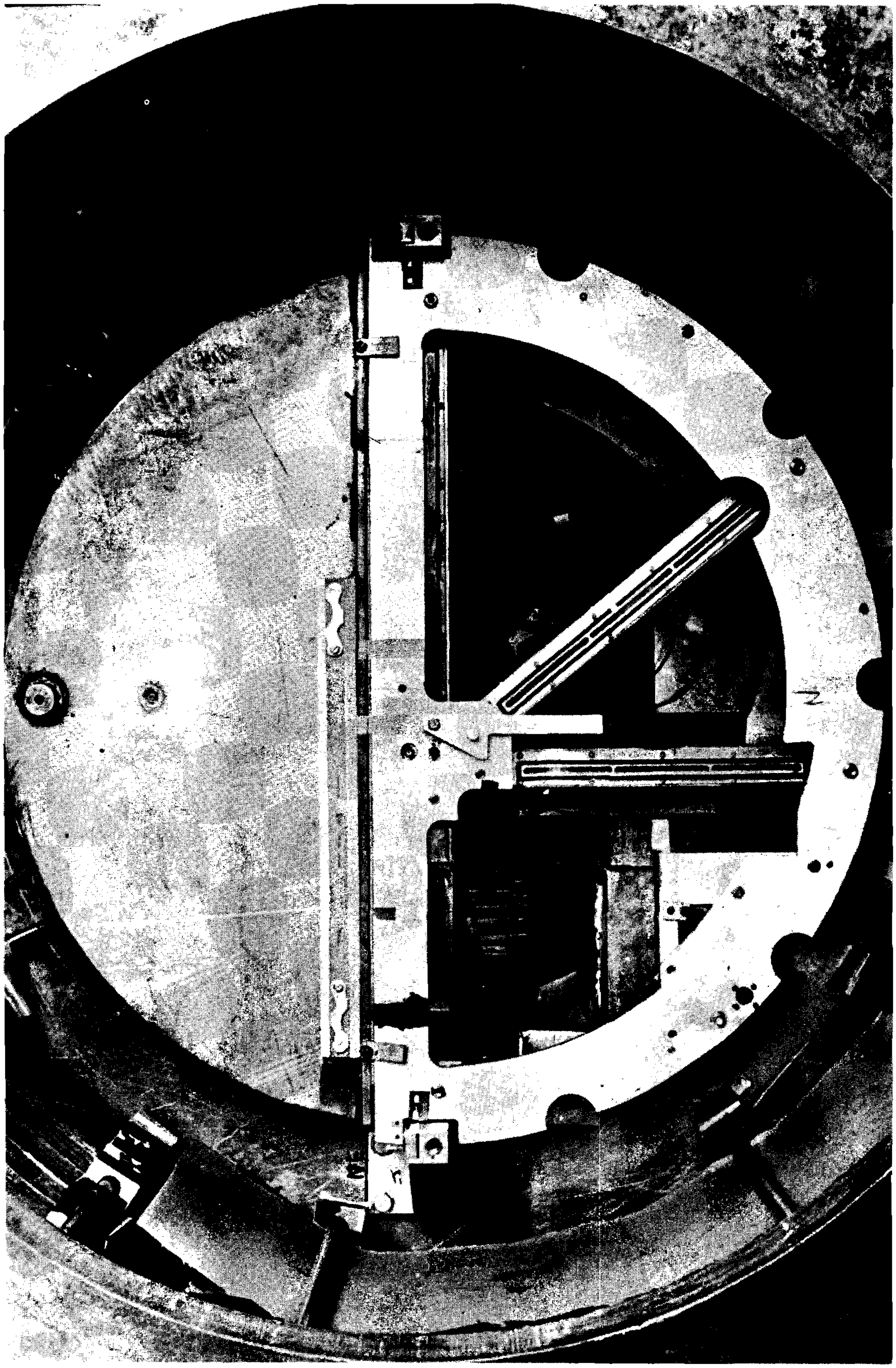

Fig. 11

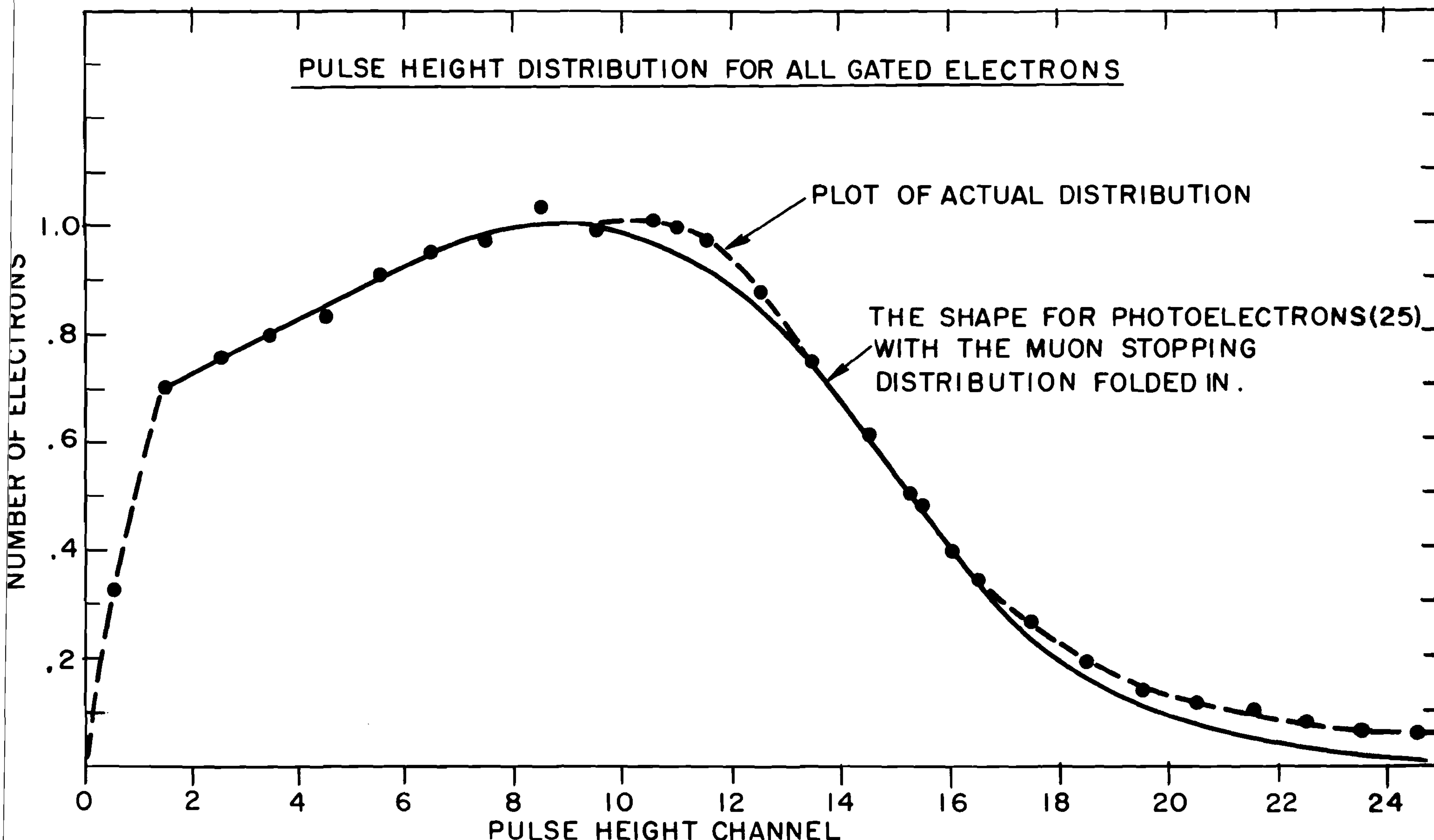
PULSE HEIGHT DISTRIBUTION FOR ALL GATED ELECTRONS
PLOT OF ACTUAL DISTRIBUTION
THE SHAPE FOR PHOTOELECTRONS(25) WITH THE MUON STOPPING DISTRIBUTION FOLDED IN.
NUMBER OF ELECTRONS
1.0
.8
.6
.4
.2
0
2
4
6
8
10
12
14
16
18
20
22
24
PULSE HEIGHT CHANNEL

FIG. 12

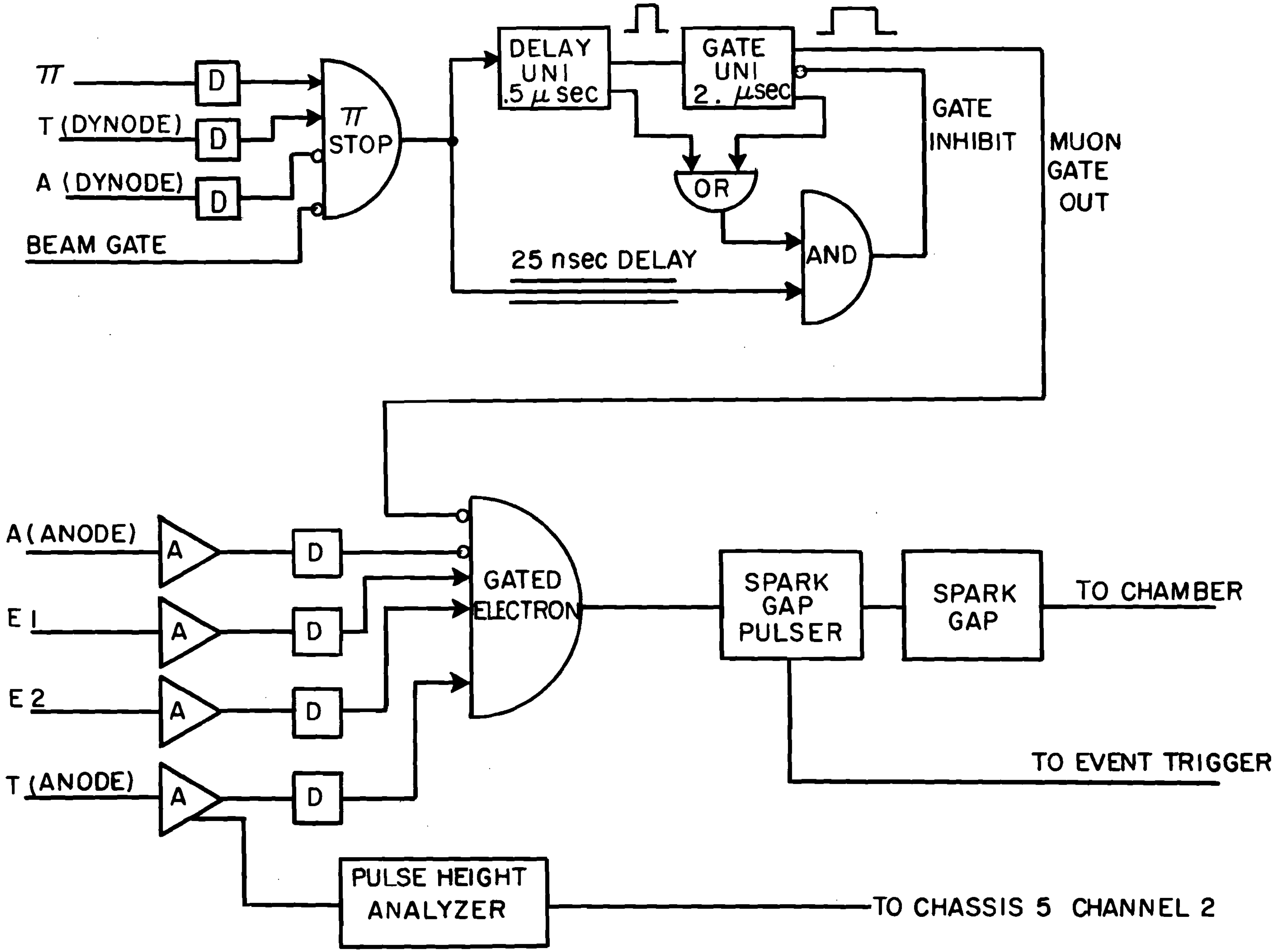

FIG. 13 BLOCK DIAGRAM OF MUON DETECTION ELECTRONICS

BLOCK DIAGRAM OF PULSE HEIGHT ANALYZER

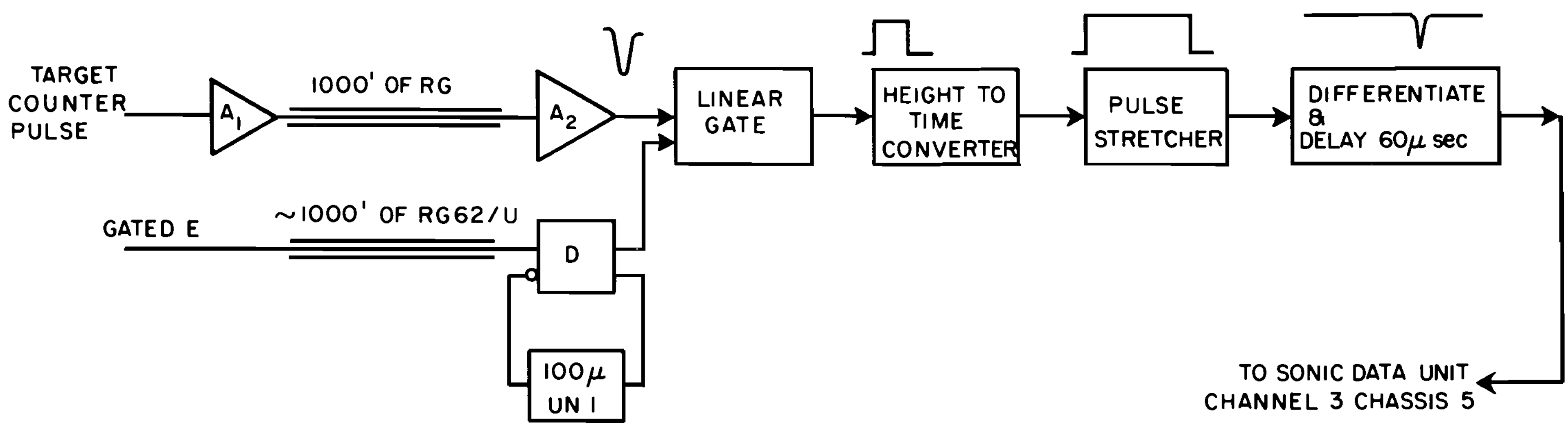

FIG. 14

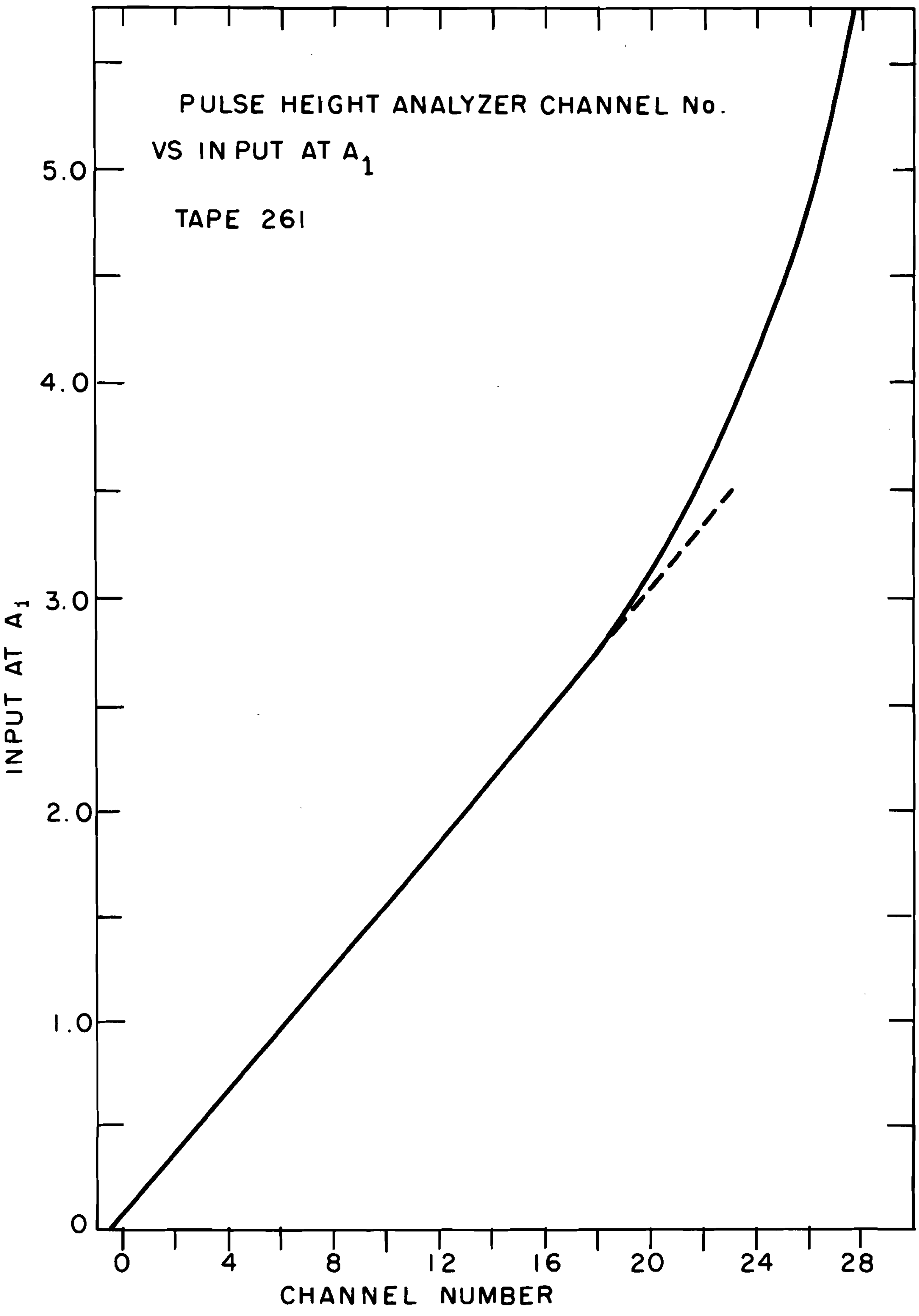
PULSE HEIGHT ANALYZER CHANNEL No.
VS INPUT AT A_1
TAPE 261
INPUT AT A_1
5.0
4.0
3.0
2.0
1.0
0
0
4
8
12
16
20
24
28
CHANNEL NUMBER

FIG. 15

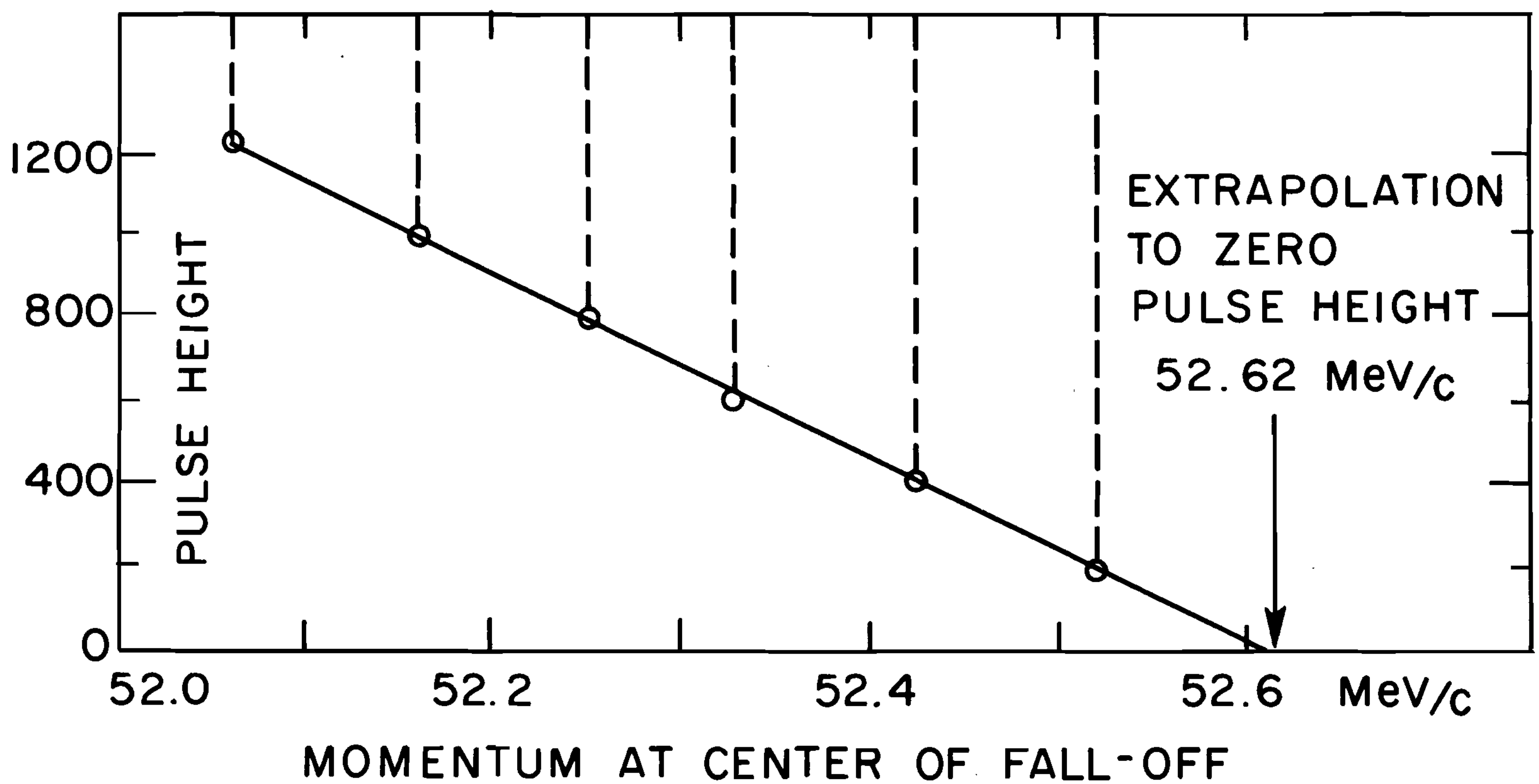

PULSE HEIGHT ANALYZER CHANNEL Vs SPECTRUM END POINT

FIG. 16

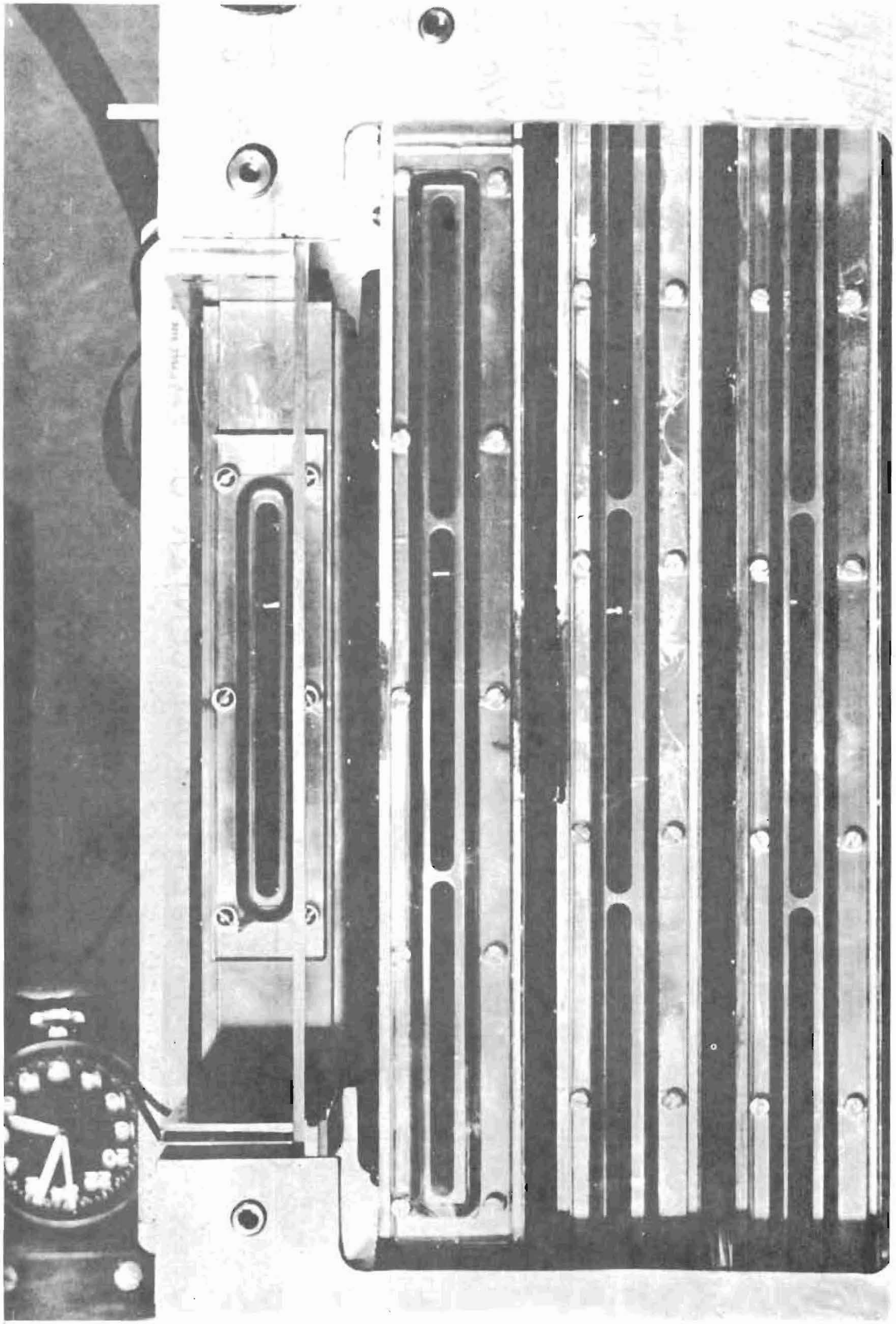

Fig. 18

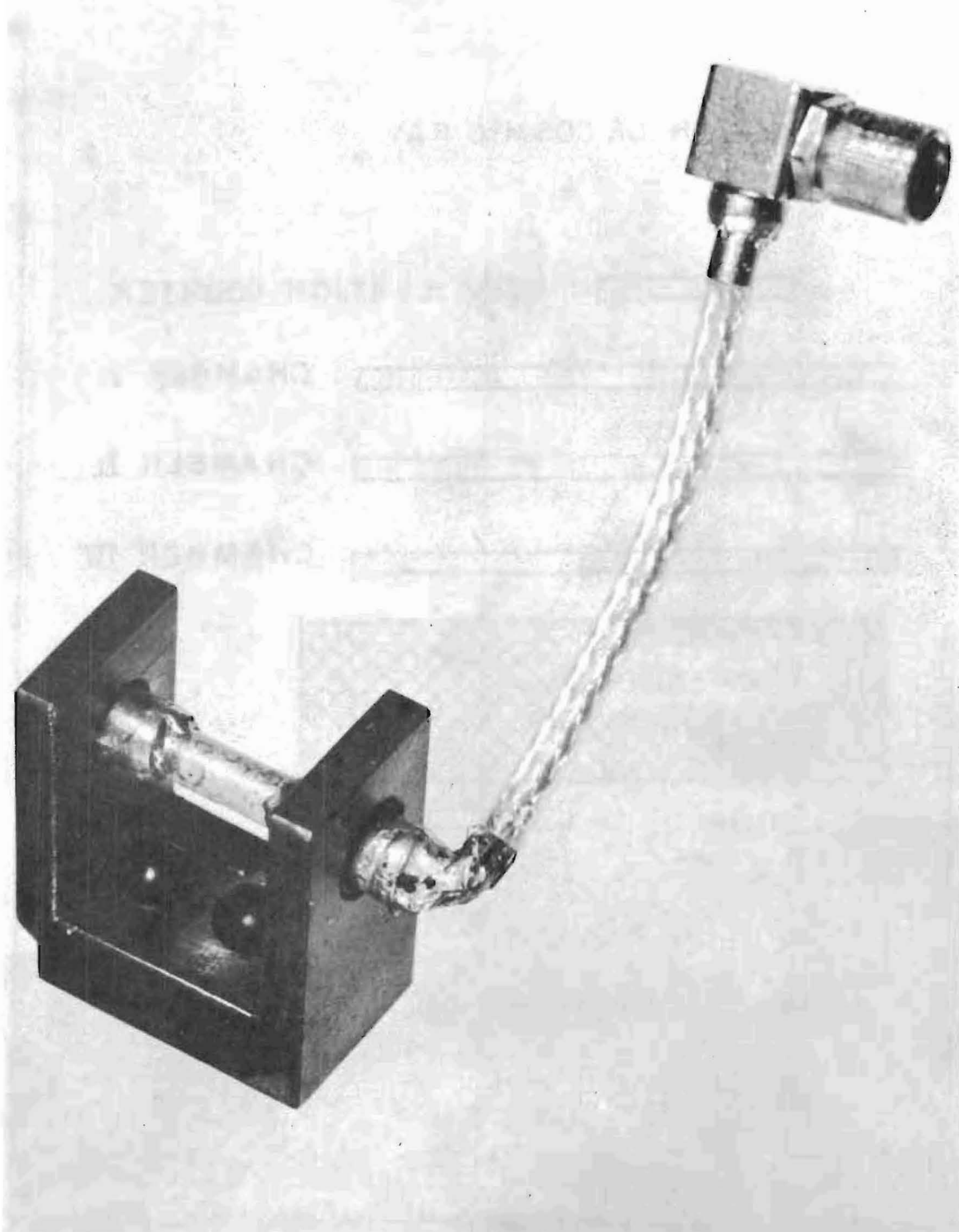

Fig. 19

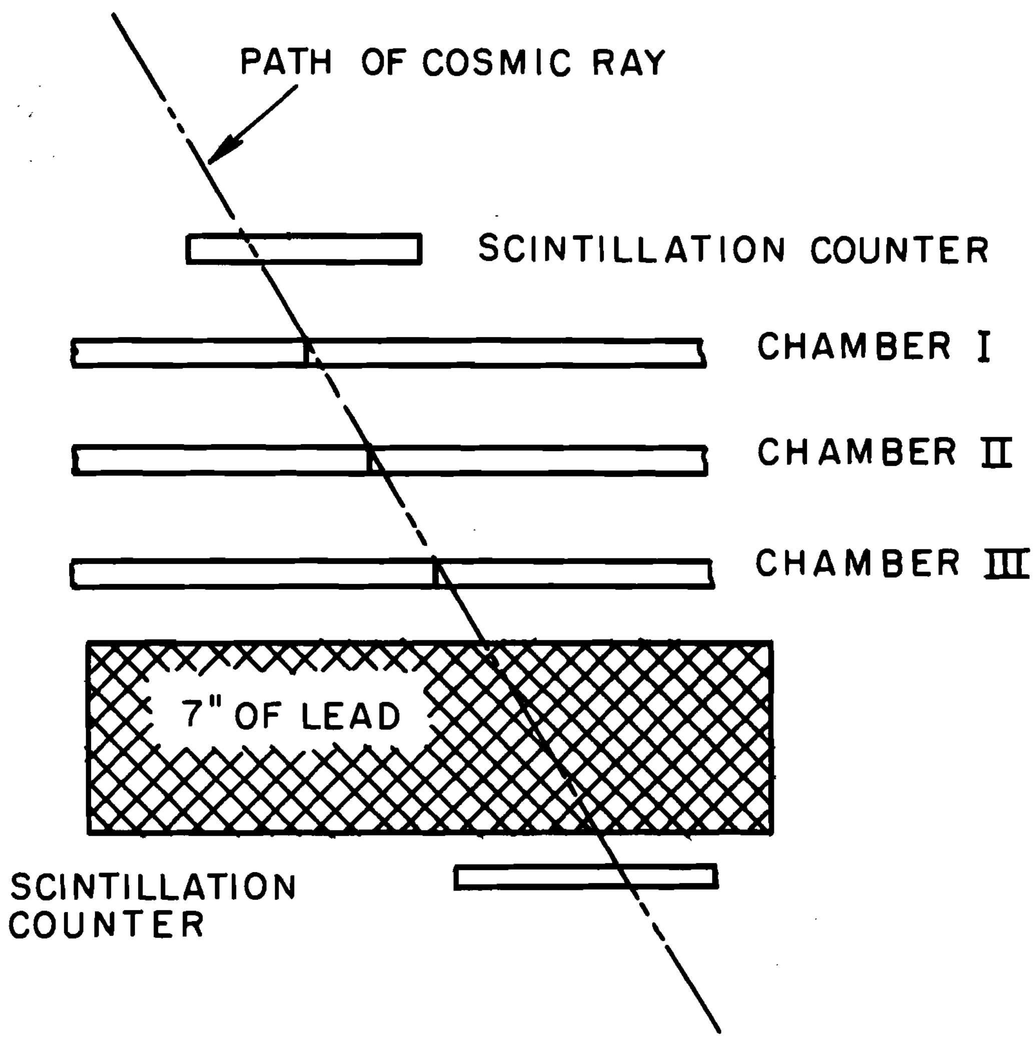

COSMIC RAY TEST SET UP

FIG. 20

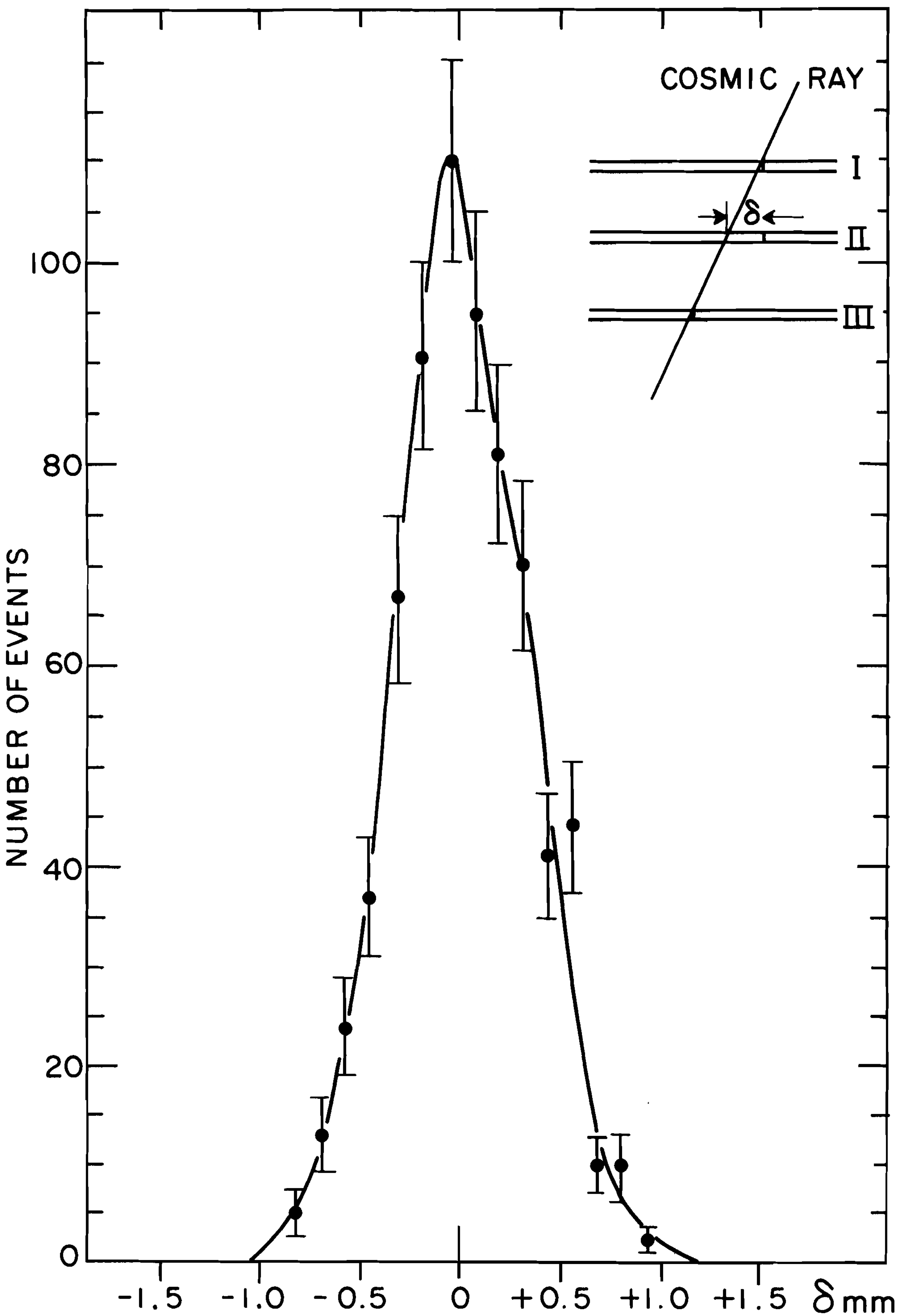
COSMIC RAY
I
δ
II
III
NUMBER OF EVENTS
100
80
60
40
20
0
-1.5
-1.0
-0.5
0
+0.5
+1.0
+1.5
δ mm

BLOCK DIAGRAM OF SONIC SPARK CHAMBER ELECTRONICS

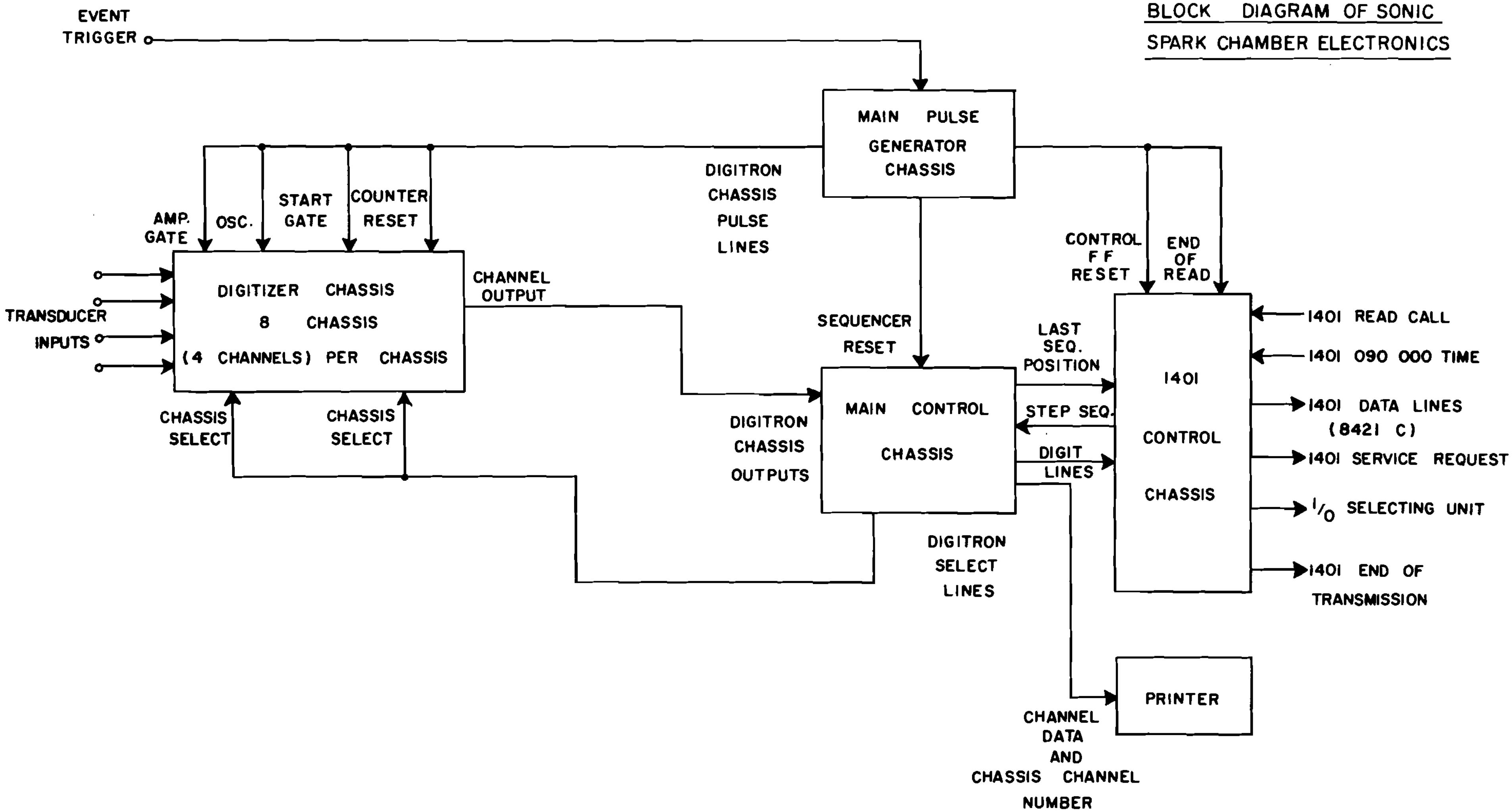

FIG. 22

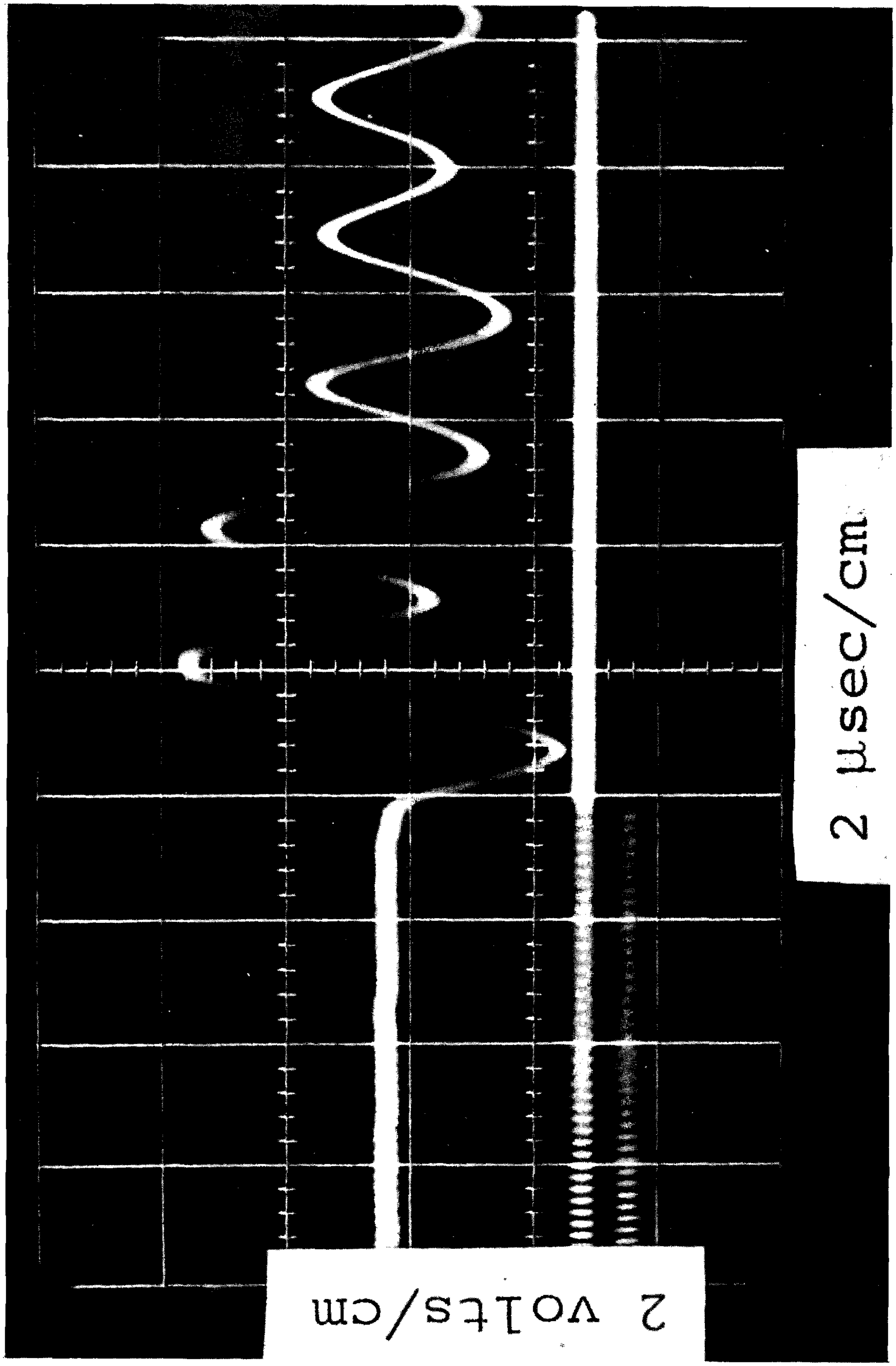

Fig. 23

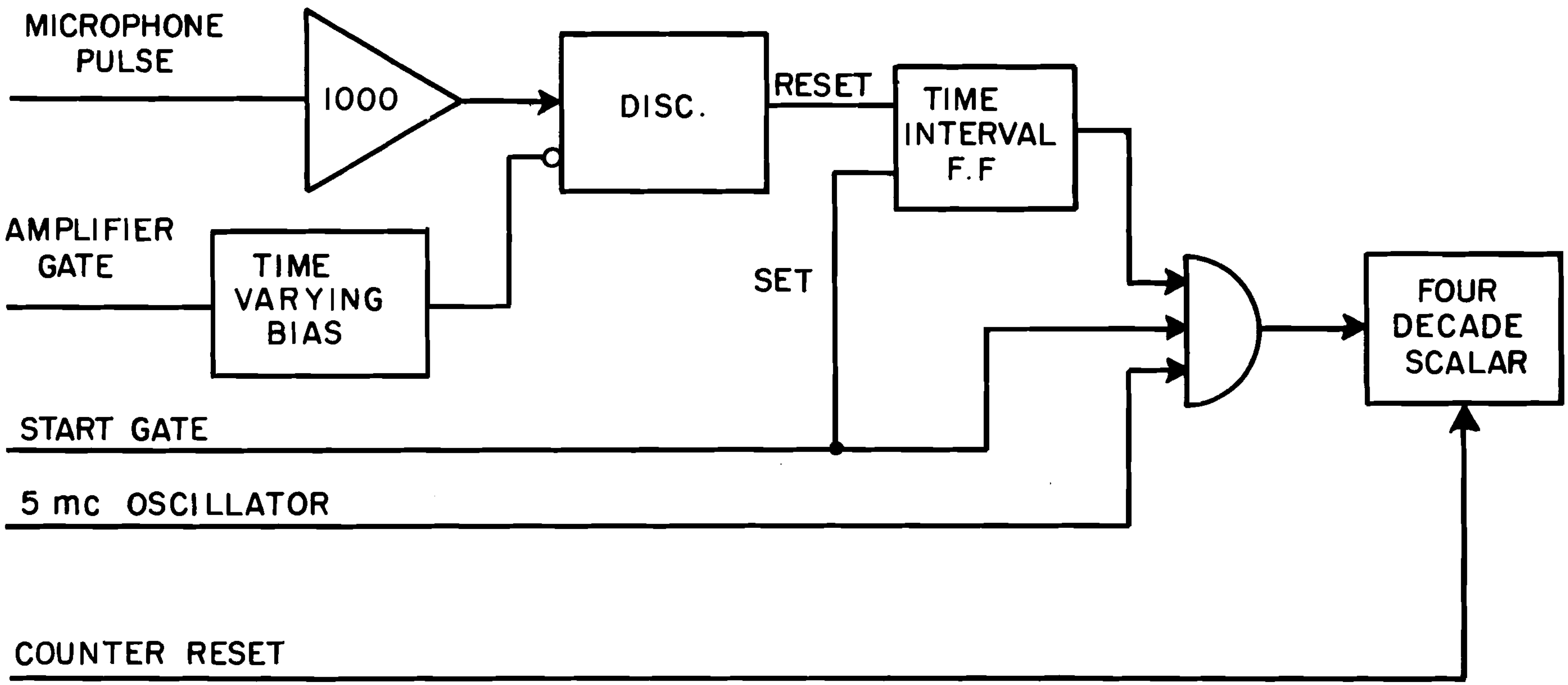

BLOCK DIAGRAM OF THE AMPLIFIER AND TIME INTERVAL GENERATOR

FIG. 24

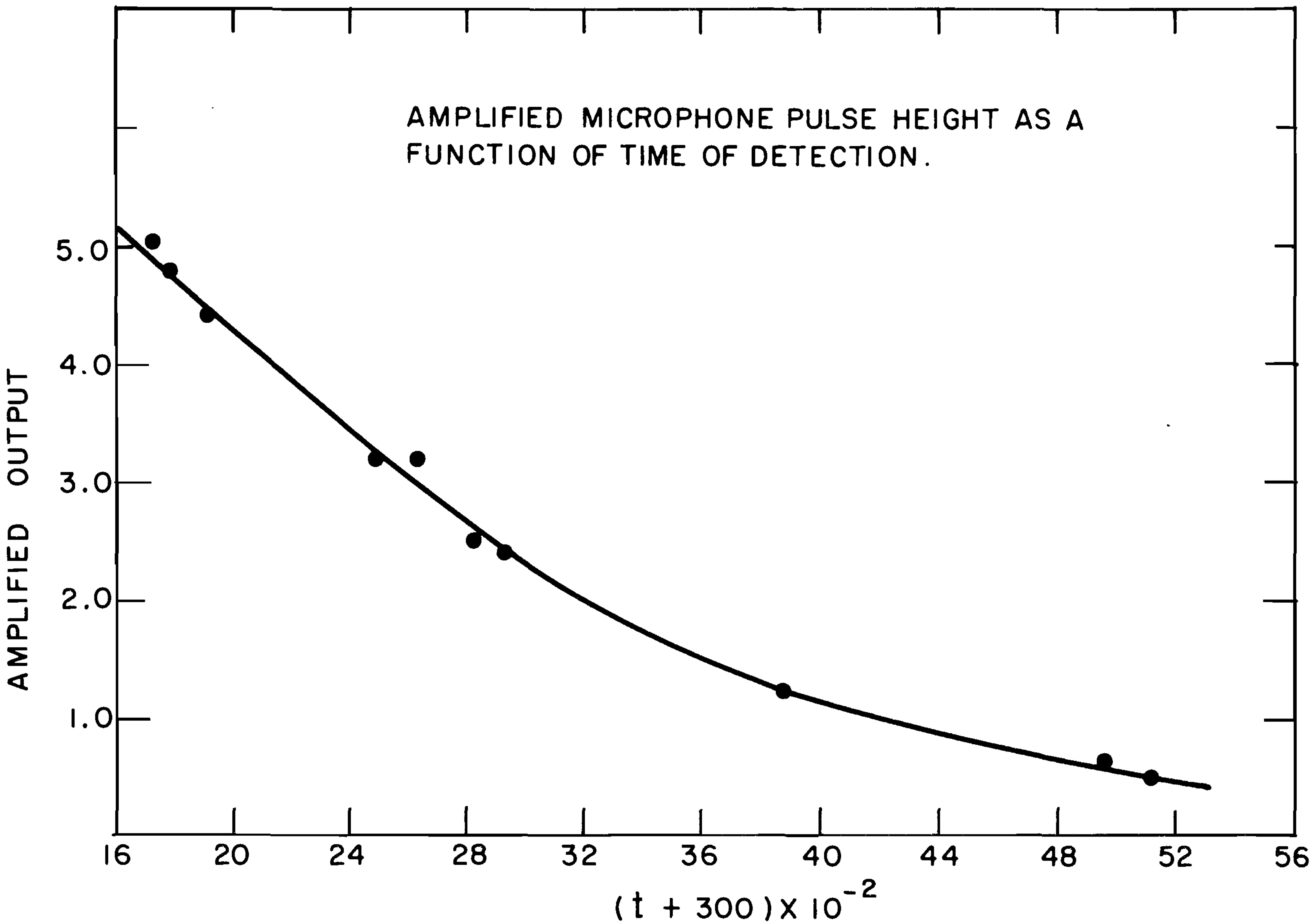
AMPLIFIED MICROPHONE PULSE HEIGHT AS A FUNCTION OF TIME OF DETECTION.
AMPLIFIED OUTPUT
5.0
4.0
3.0
2.0
1.0
16
20
24
28
32
36
40
44
48
52
56
(t + 300) X 10⁻²

FIG. 25

BLOCK DIAGRAM OF 1401 READING SEQUENCE

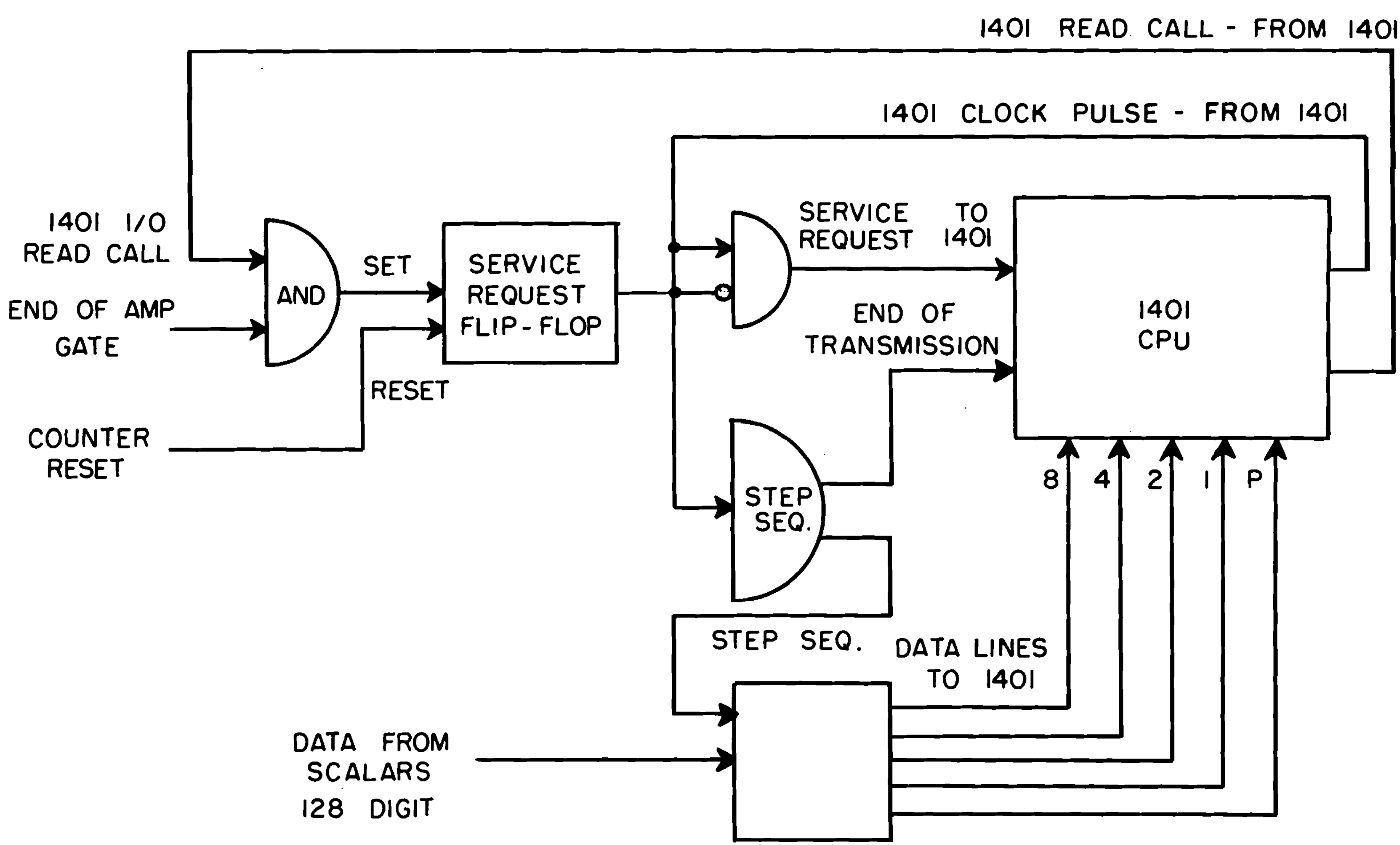

FIG. 26

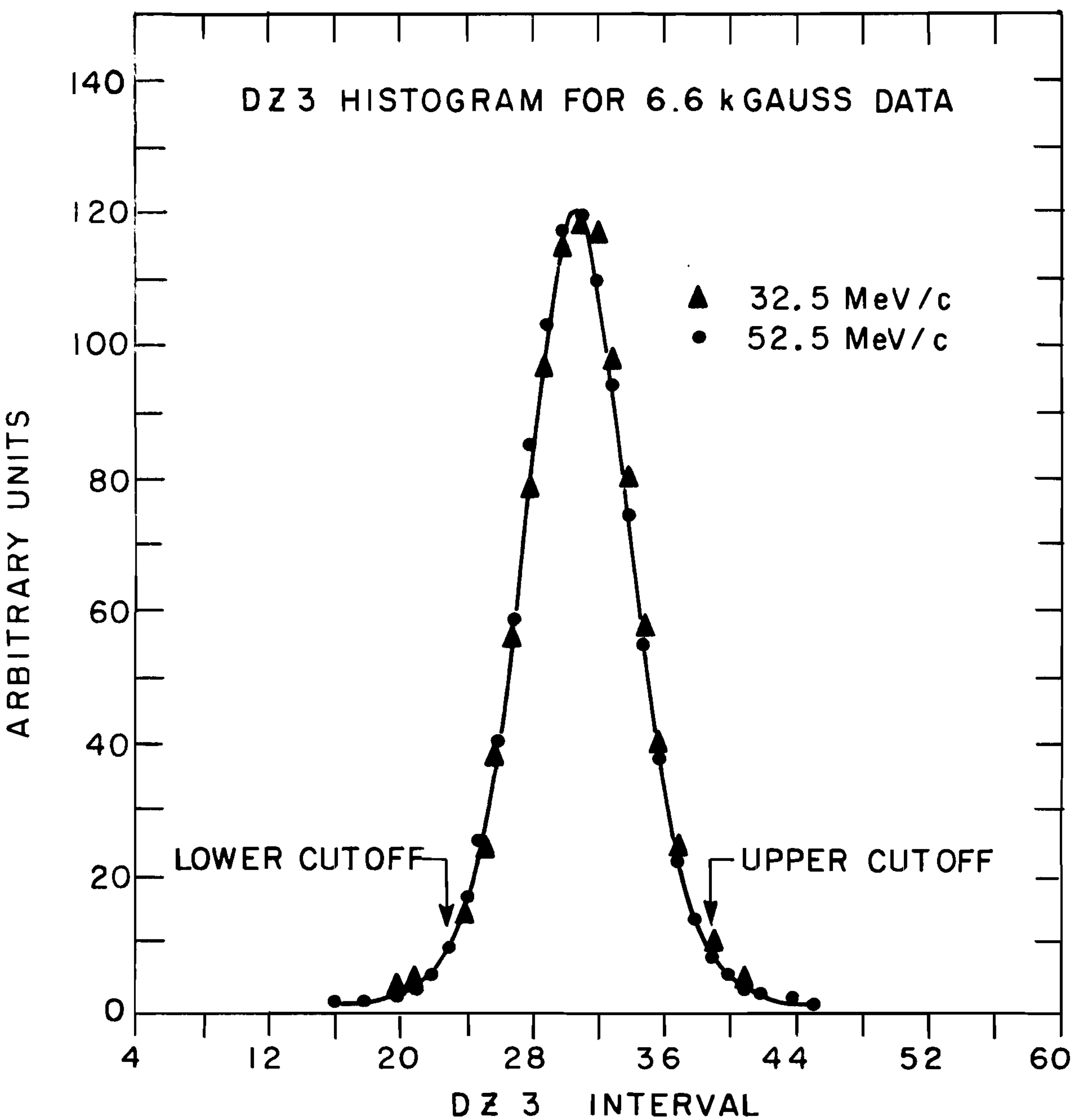
DZ 3 HISTOGRAM FOR 6.6 kGAUSS DATA
32.5 MeV/c
52.5 MeV/c
ARBITRARY UNITS
140
120
100
80
60
40
20
0
LOWER CUTOFF
UPPER CUTOFF
4
12
20
28
36
44
52
60
DZ 3 INTERVAL

FIG. 28

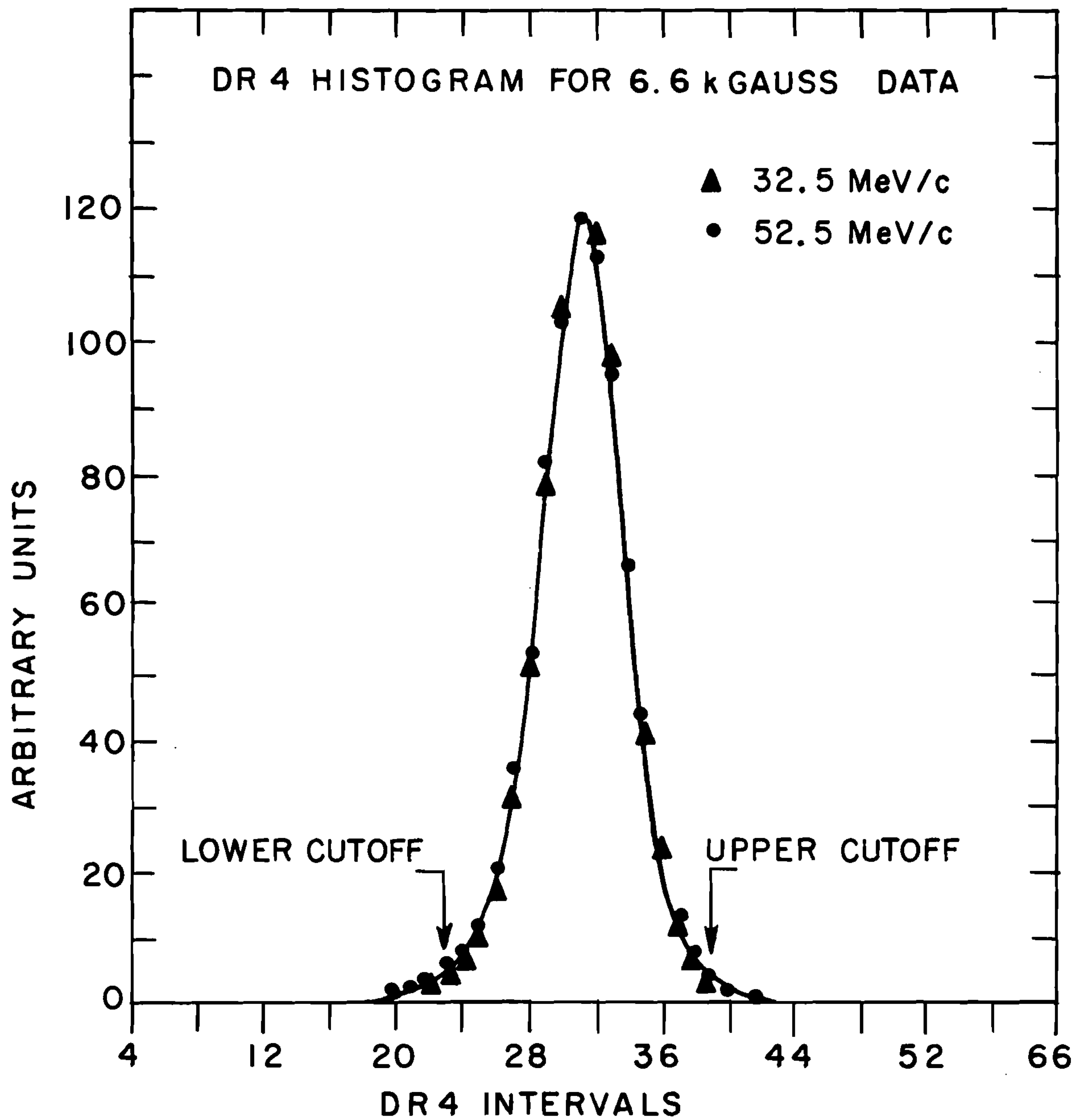
DR 4 HISTOGRAM FOR 6.6 k GAUSS DATA
▲ 32.5 MeV/c
● 52.5 MeV/c
ARBITRARY UNITS
0
20
40
60
80
100
120
LOWER CUTOFF
UPPER CUTOFF
4
12
20
28
36
44
52
66
DR 4 INTERVALS

FIG. 29

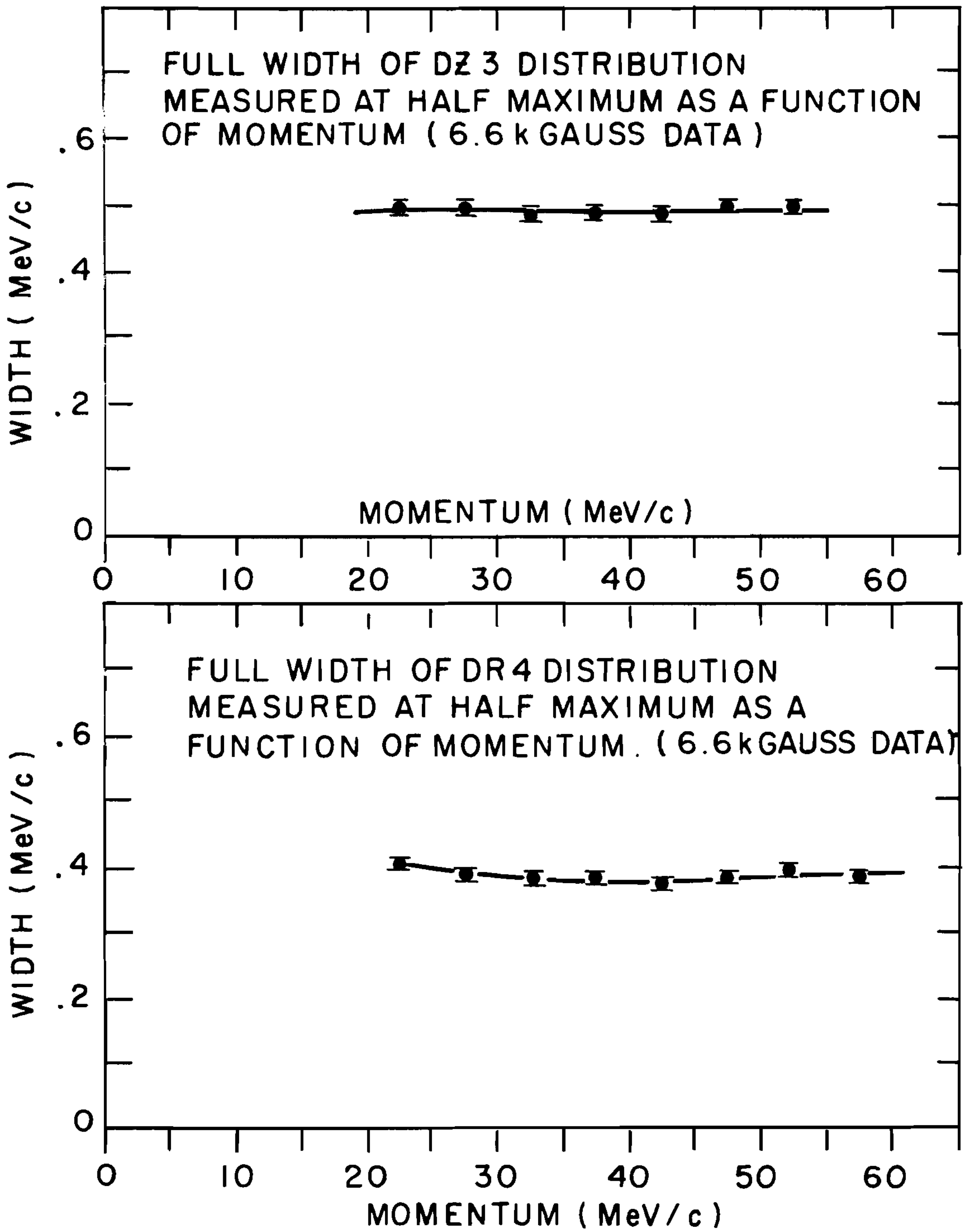
FULL WIDTH OF DZ 3 DISTRIBUTION
MEASURED AT HALF MAXIMUM AS A FUNCTION
OF MOMENTUM (6.6 k GAUSS DATA)
WIDTH (MeV/c)
.6
.4
.2
0
MOMENTUM (MeV/c)
0
10
20
30
40
50
60
FULL WIDTH OF DR4 DISTRIBUTION
MEASURED AT HALF MAXIMUM AS A
FUNCTION OF MOMENTUM. (6.6kGAUSS DATA)
WIDTH (MeV/c)
.6
.4
.2
0
0
10
20
30
40
50
60
MOMENTUM (MeV/c)

FIG. 30

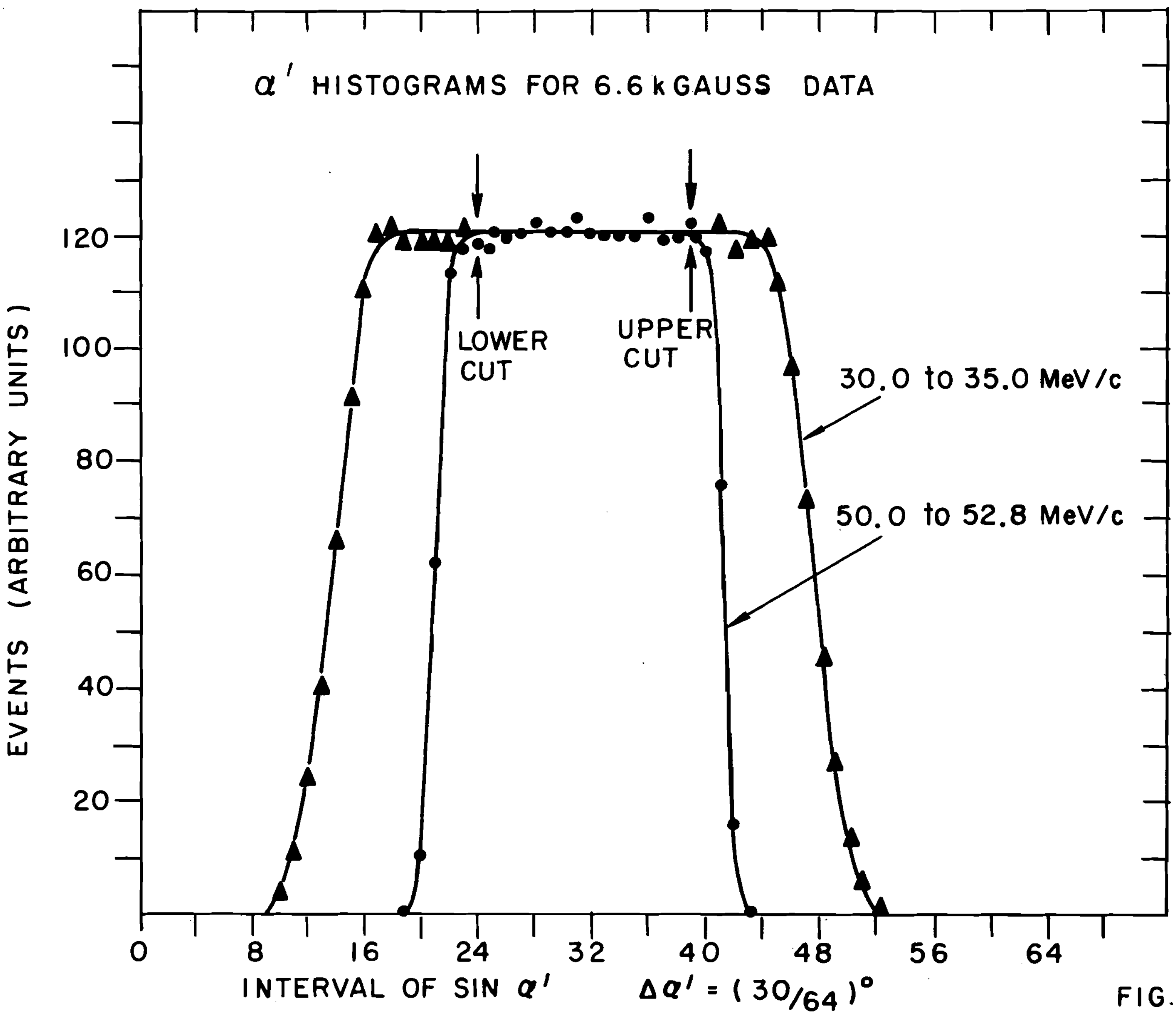
α' HISTOGRAMS FOR 6.6 k GAUSS DATA
LOWER CUT
UPPER CUT
30.0 to 35.0 MeV/c
50.0 to 52.8 MeV/c
EVENTS (ARBITRARY UNITS)
120
100
80
60
40
20
0
8
16
24
32
40
48
56
64
INTERVAL OF SIN α'
Δα' = (30/64)°

FIG. 31

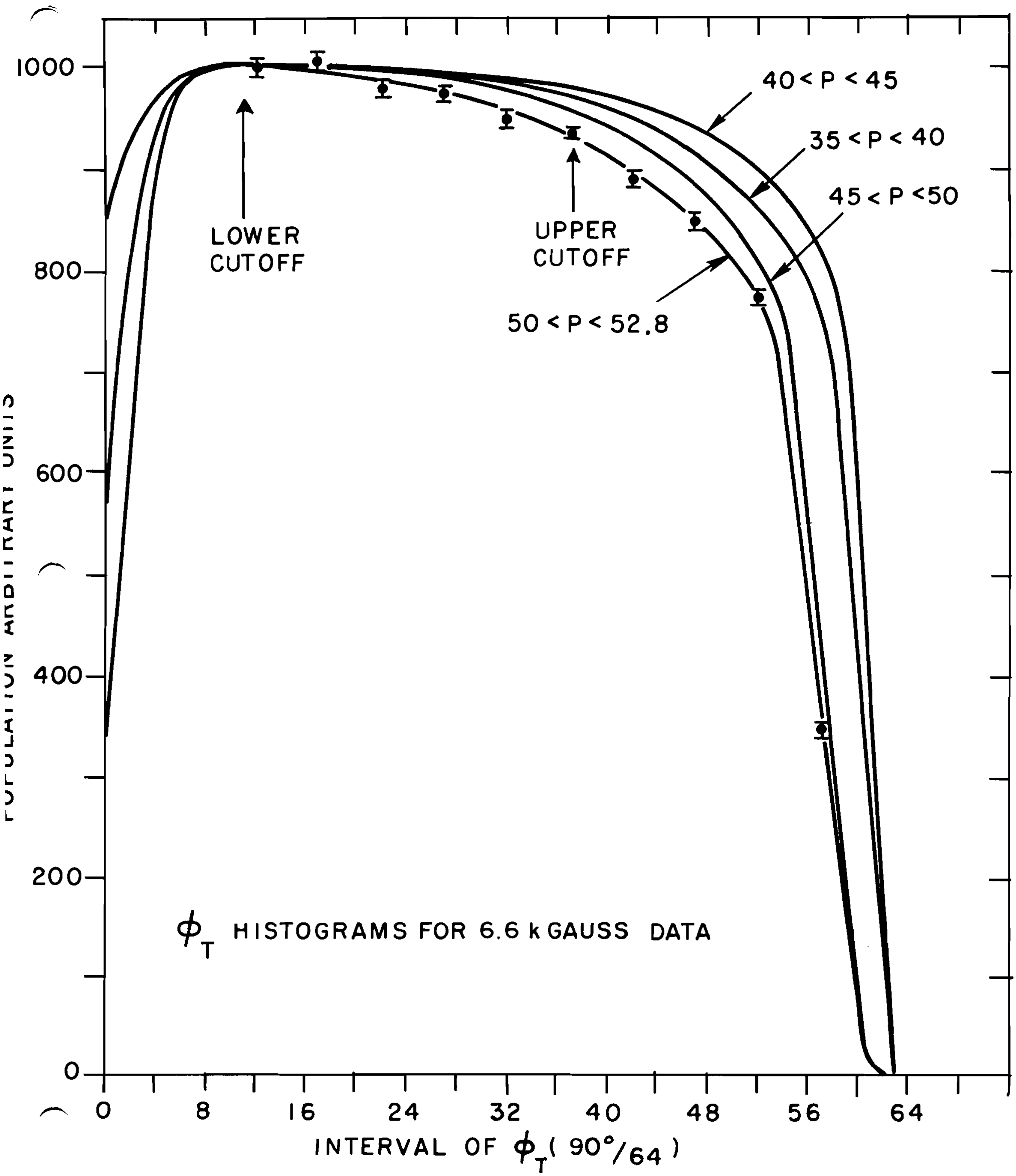
POPULATION ARBITRARY UNITS
1000
800
600
400
200
0
40 < P < 45
35 < P < 40
45 < P < 50
50 < P < 52.8
LOWER CUTOFF
UPPER CUTOFF
φT HISTOGRAMS FOR 6.6 k GAUSS DATA
0
8
16
24
32
40
48
56
64
INTERVAL OF φT (90°/64)

FIG. 32

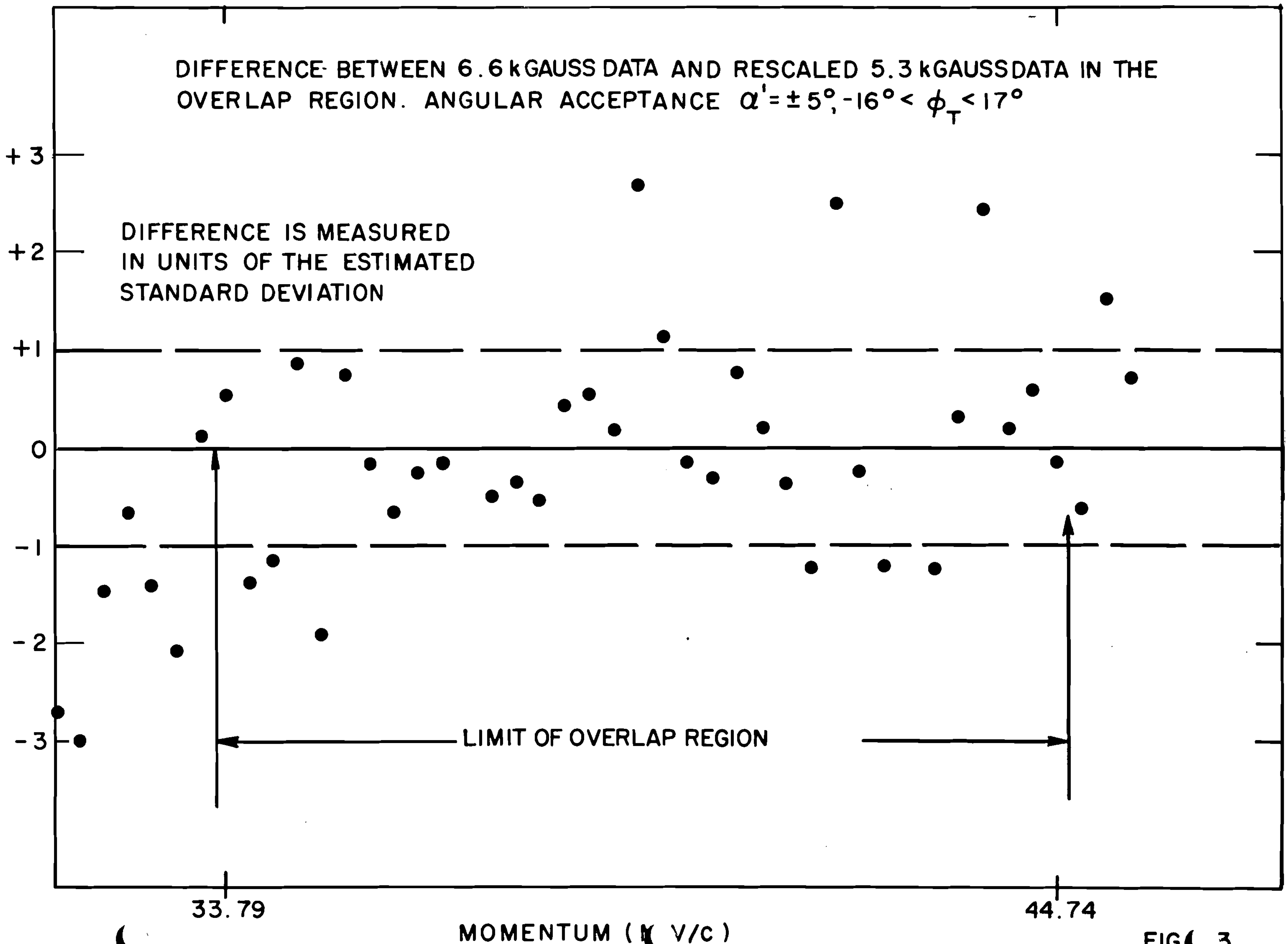
DIFFERENCE BETWEEN 6.6 kGAUSS DATA AND RESCALED 5.3 kGAUSS DATA IN THE OVERLAP REGION. ANGULAR ACCEPTANCE $\alpha' = \pm 5°, -16° < \phi_T < 17°$
DIFFERENCE IS MEASURED IN UNITS OF THE ESTIMATED STANDARD DEVIATION
+3
+2
+1
0
-1
-2
-3
LIMIT OF OVERLAP REGION
33.79
44.74
MOMENTUM (V/C)

FIG 3

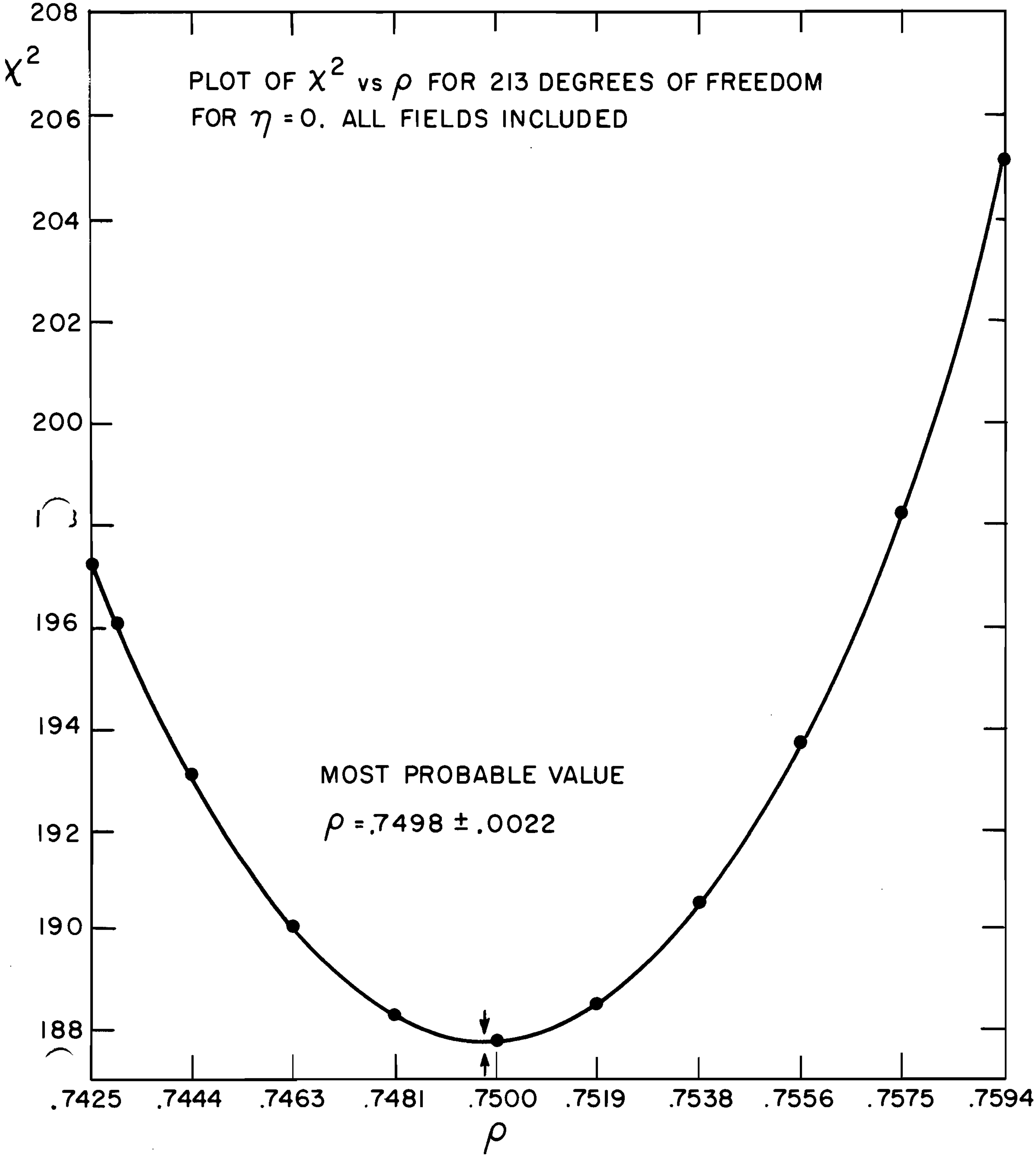

208
206
204
202
200
196
194
192
190
188
χ^2
PLOT OF χ^2 vs ρ FOR 213 DEGREES OF FREEDOM
FOR η = 0. ALL FIELDS INCLUDED
MOST PROBABLE VALUE
ρ = .7498 ± .0022
.7425
.7444
.7463
.7481
.7500
.7519
.7538
.7556
.7575
.7594
ρ

FIG. 34

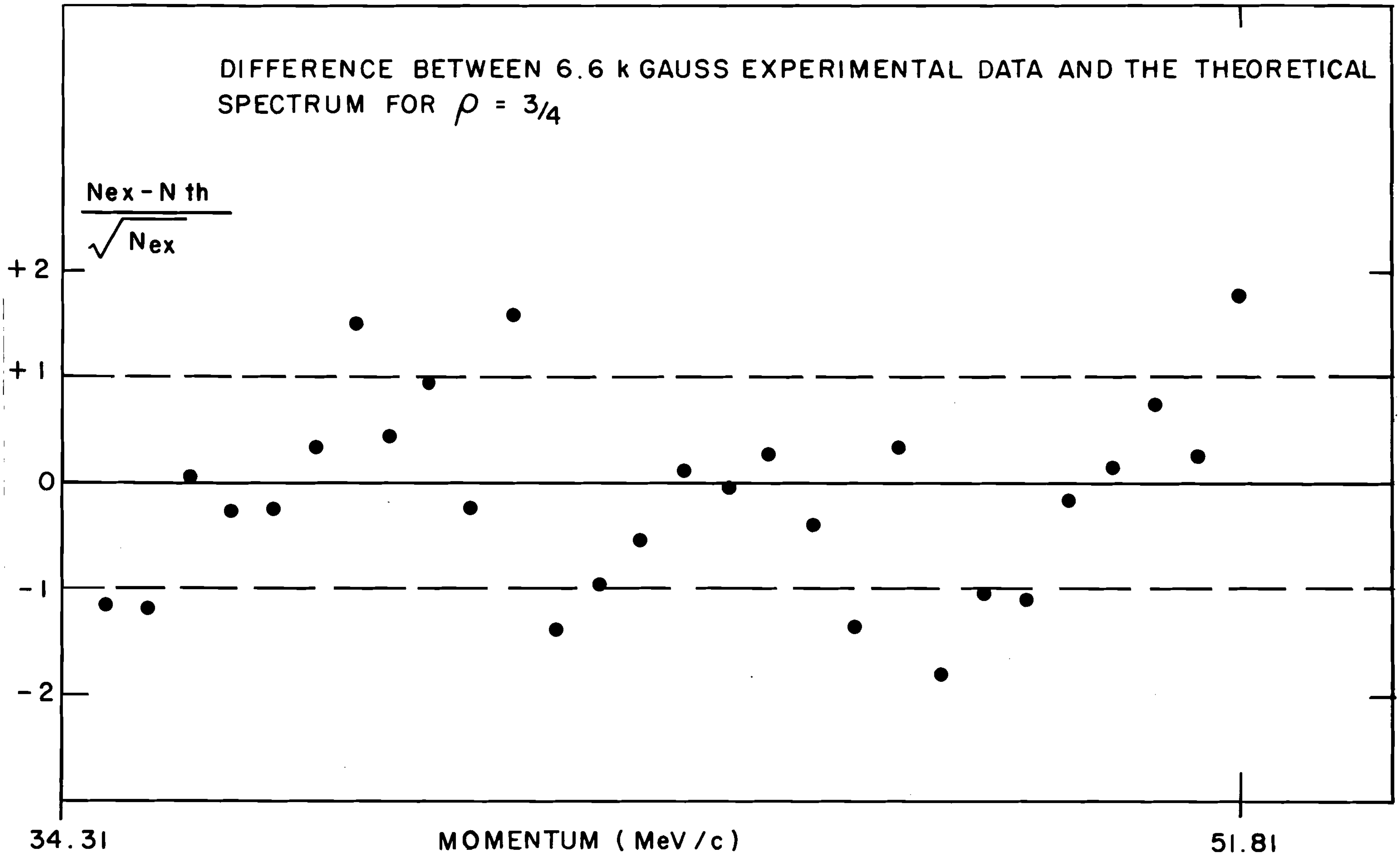
DIFFERENCE BETWEEN 6.6 k GAUSS EXPERIMENTAL DATA AND THE THEORETICAL SPECTRUM FOR ρ = 3/4
Nex - N th / √Nex
+2
+1
0
-1
-2
34.31
MOMENTUM (MeV/c)
51.81

FIG. 35

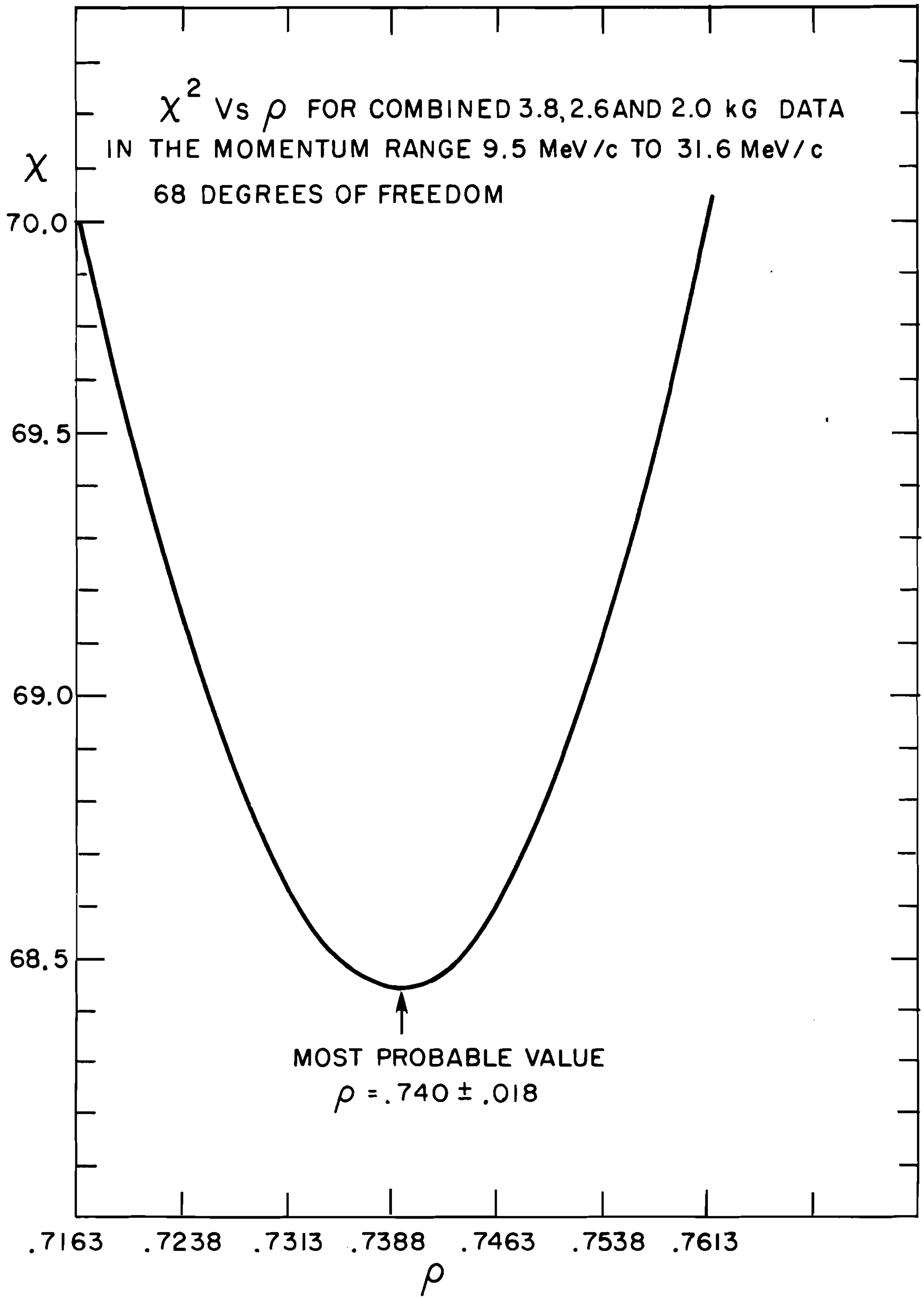

χ^2 Vs ρ FOR COMBINED 3.8, 2.6 AND 2.0 kG DATA
IN THE MOMENTUM RANGE 9.5 MeV/c TO 31.6 MeV/c
68 DEGREES OF FREEDOM
χ
70.0
69.5
69.0
68.5
MOST PROBABLE VALUE
ρ = .740 ± .018
.7163
.7238
.7313
.7388
.7463
.7538
.7613
ρ

FIG. 36

BLOCK DIAGRAM OF DIGITRON DECADE COUNTER

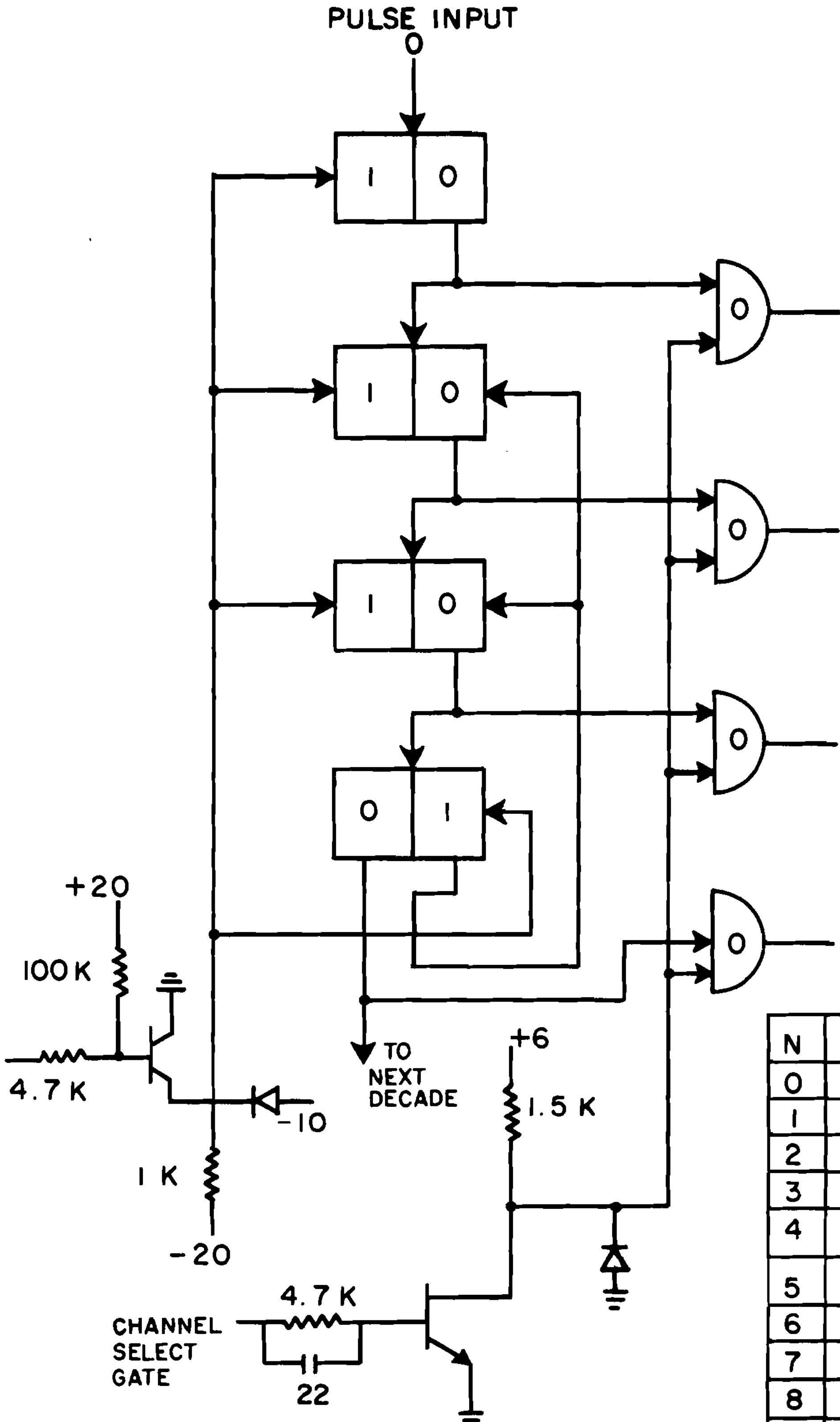

N	D	C	B	A
0	1	0	0	0
1	1	0	0	1
2	1	0	1	0
3	1	0	1	1
4	1	1	0	0
5	1	1	0	1
6	1	1	1	0
7	1	1	1	1
8	0	1	1	0
9	0	1	1	1

FIG.37

MAIN PULSE G ERATOR CHASSIS

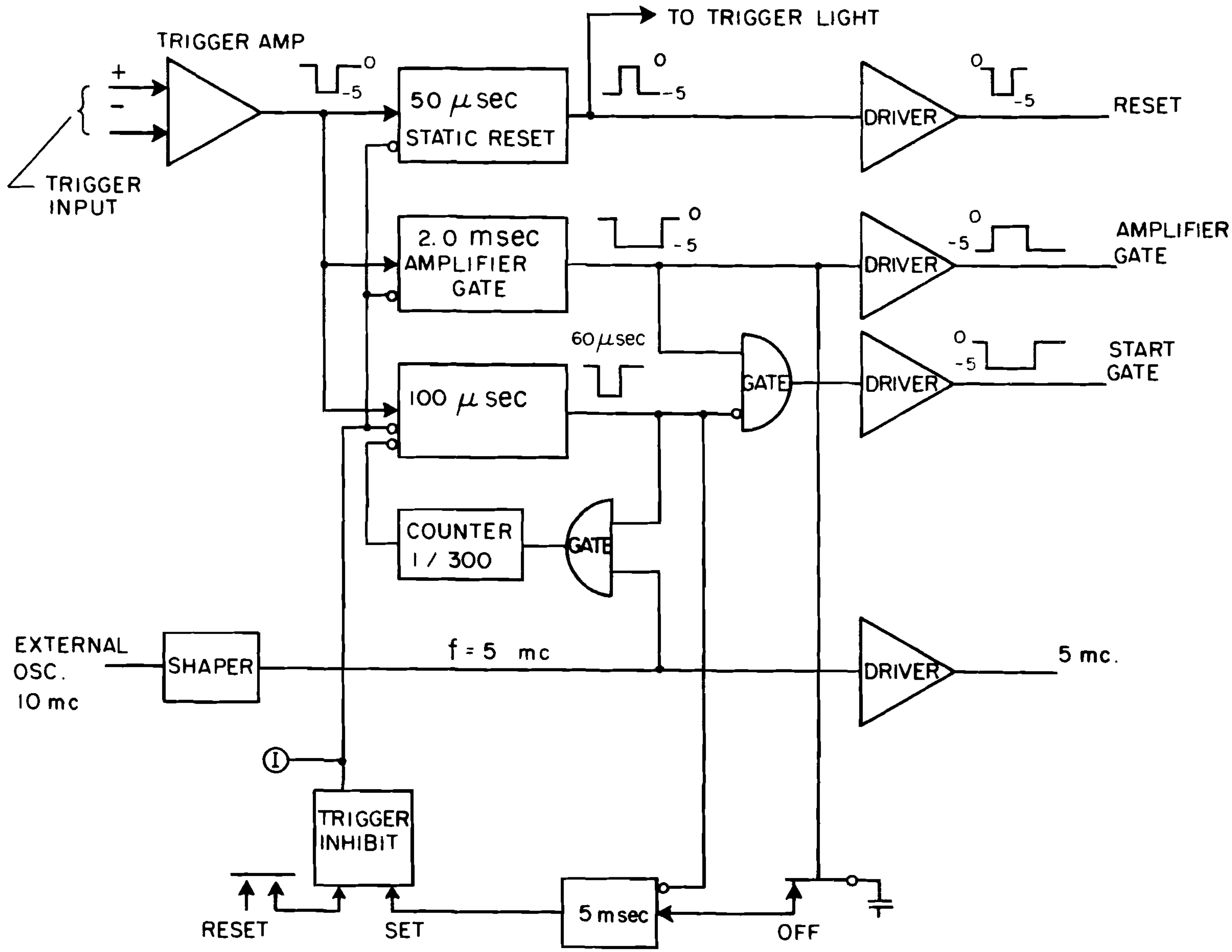

FIG. 38

EXAMPLE OF MIXING OF DIGIT LINES - I LINE SHOWN

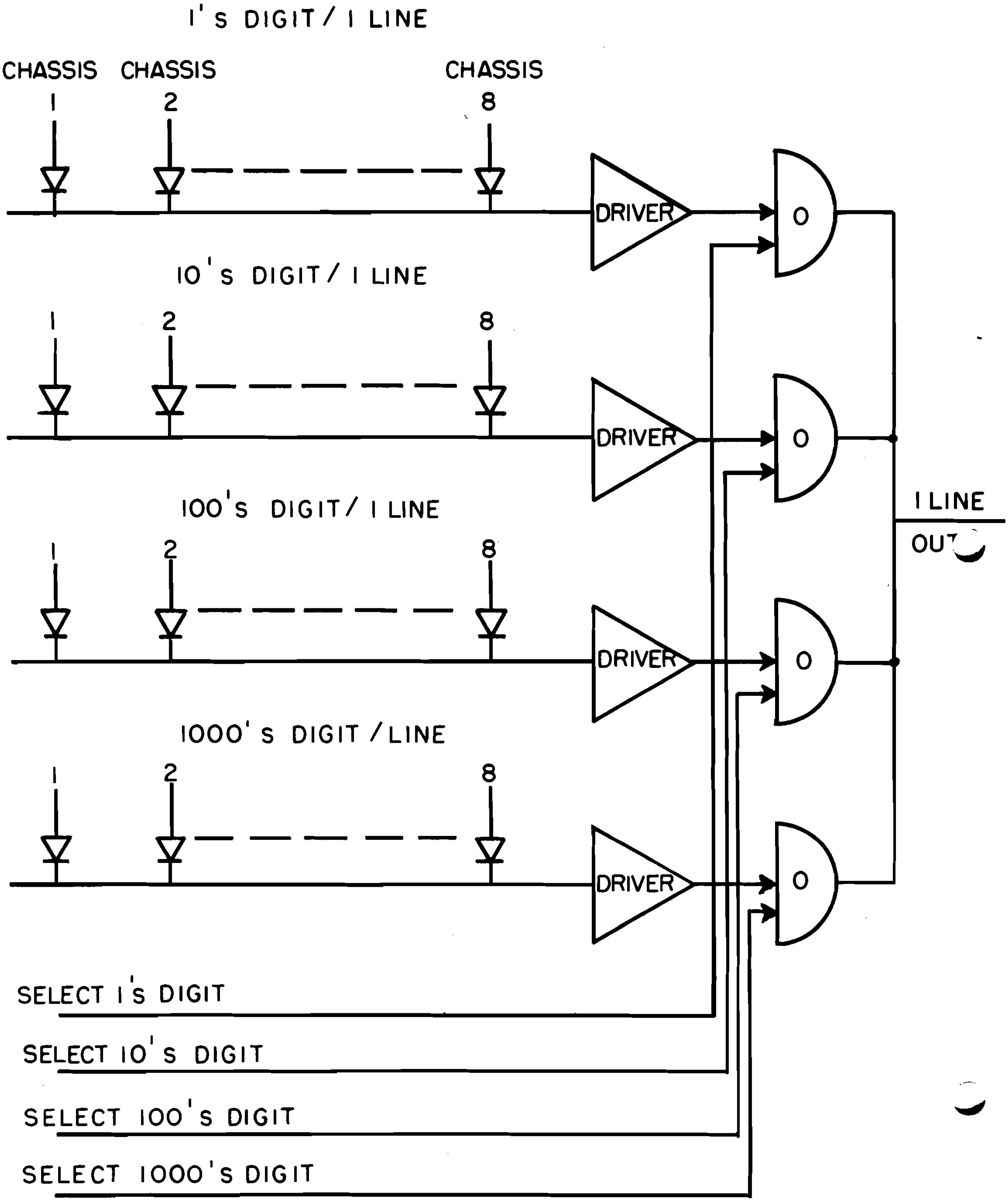

FIG. 39

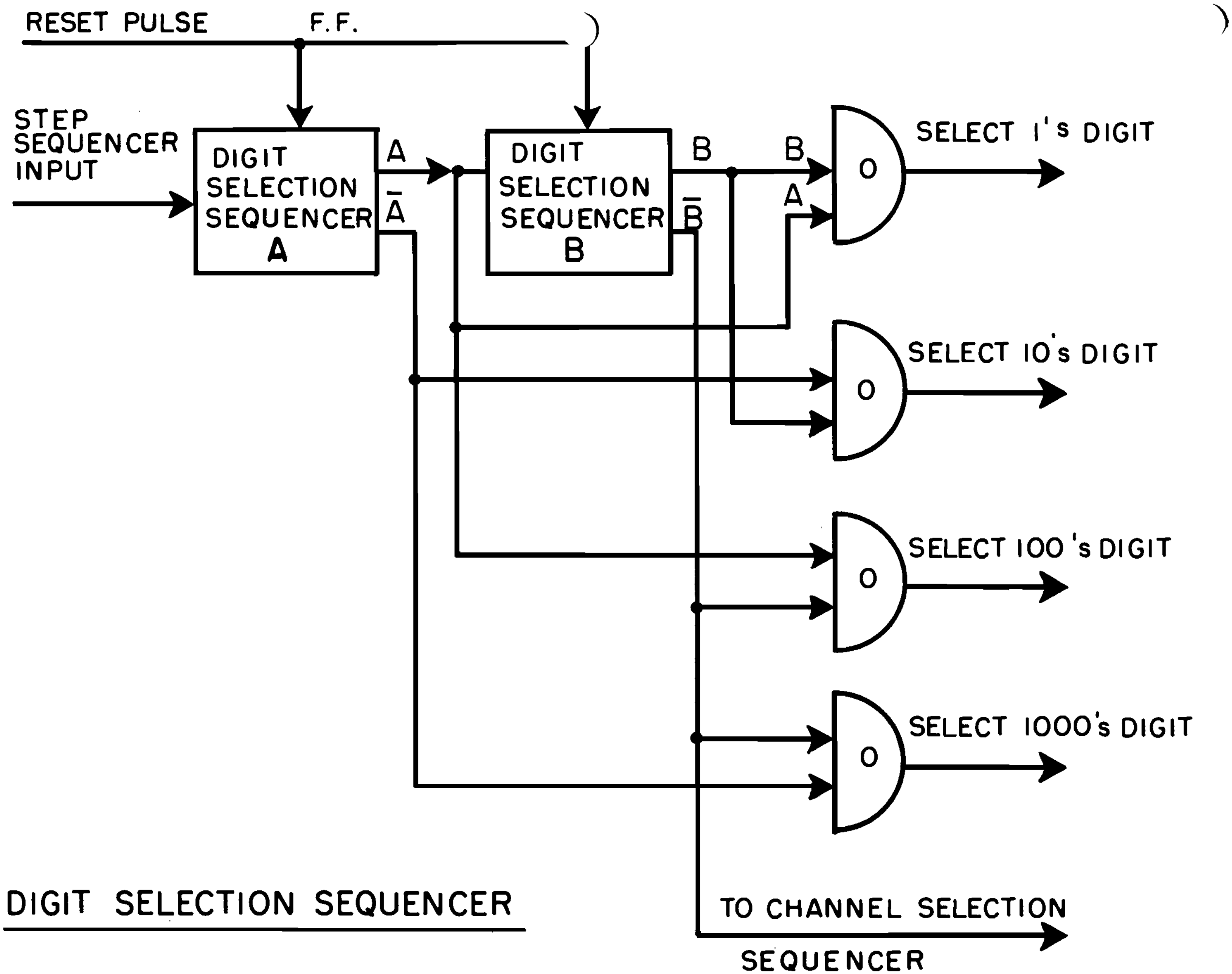

DIGIT SELECTION SEQUENCER

FIG. 40

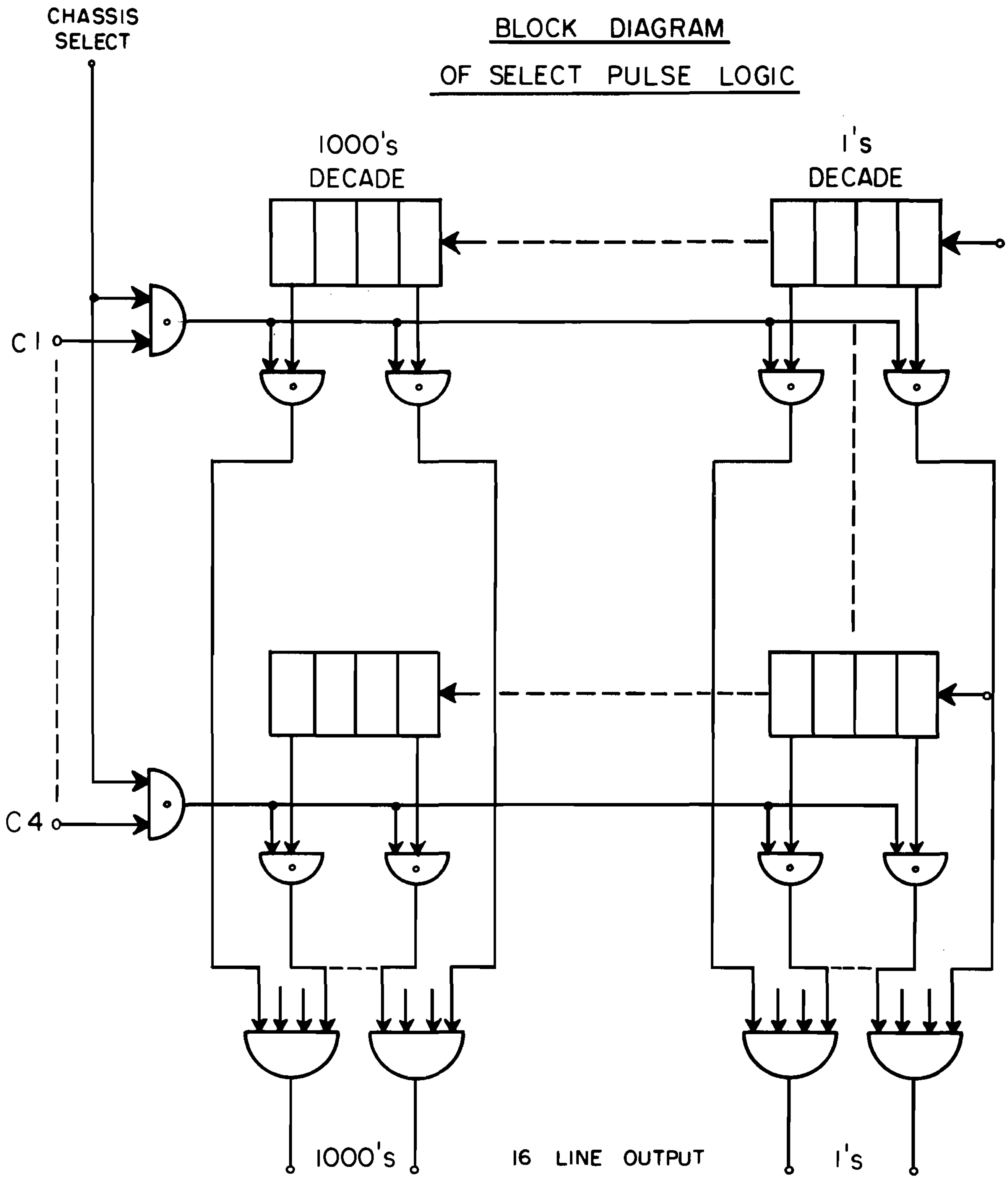
CHASSIS
SELECT
BLOCK DIAGRAM
OF SELECT PULSE LOGIC
1000's
DECADE
1's
DECADE
C1
C4
1000's
16 LINE OUTPUT
1's

FIG. 41

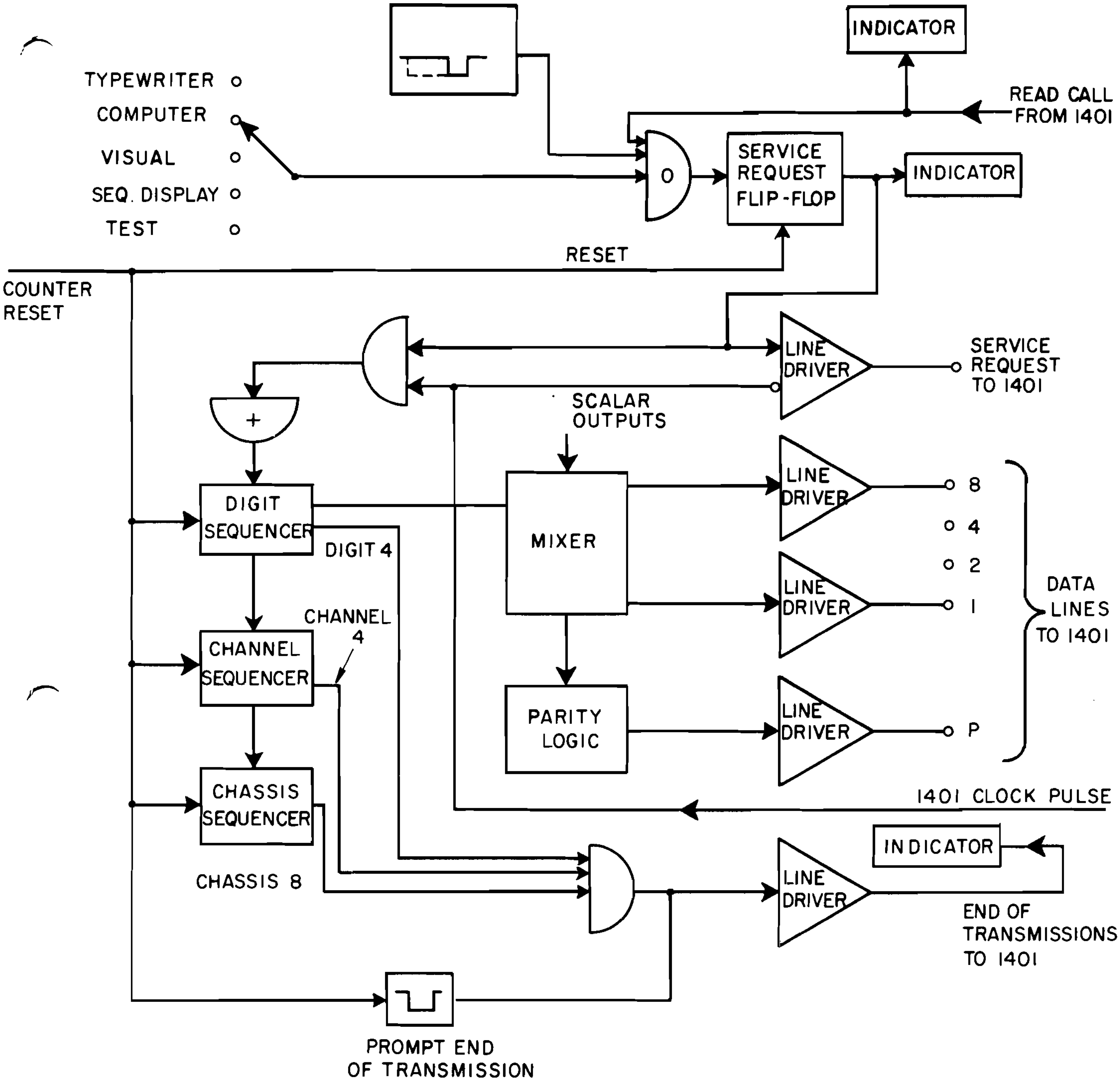

1401 CONTROL CHASSIS

FIG. 42